Communications Research Centre

CHARACTERIZATION AND DESIGN OF IMPATT DIODES AND
ASSOCIATED CIRCUITS

by

A.E. WINTER

DEPARTMENT OF COMMUNICATIONS
MINISTÈRE DES COMMUNICATIONS

CRC REPORT NO. 1257

OTTAWA, DECEMBER 1974

COMMUNICATIONS RESEARCH CENTRE

DEPARTMENT OF COMMUNICATIONS
CANADA

CHARACTERIZATION AND DESIGN OF IMPATT DIODES AND ASSOCIATED CIRCUITS

by

A.E. Winter*

(Communications Systems Directorate)

CRC REPORT NO. 1257

December 1974

OTTAWA

TABLE OF CONTENTS

LIST OF FIGURES

vii

LIST OF IMPORTANT SYMBOLS

A_j — area of cross-section of the chip at the boundary between lump j and j+1, cm^2

$[A],[B],$
$[C],[D]$ — matrices of the state space representation

C_j — capacitance of the reverse biased chip, pF

C_p,C_2 — package capacitances, pF

C_T — transition capacitance between the radial and coaxial lines, pF

e — normalized average error per reading

E_j — electric field at the boundary between lump j and j+1, $V\ cm^{-1}$

F — noise figure, dB

$[G]$ — the Hessian matrix

G — power gain, dB

I_a — total avalanche current, mA

I_o — dc bias current, mA

L_A — avalanche region length, cm

L_D — drift region length, cm

L_p — package inductance, nH

L_R — radial line length, cm

L_T — transition inductance between the radial and coaxial lines, nH

M	noise measure, dB
n	electron density, cm^{-3}
p	hole density, cm^{-3}
R_s	parasitic resistance of the chip, ohms
s	complex radian frequency, $rad\ sec^{-1}$
$U(\underline{\phi})$	objective function for the computer parameter search
v	saturated drift velocity, $cm\ sec^{-1}$
$\underline{x}$	state vector
$\underline{X}(s)$	Laplace Transform of the state vector
Δx	drift region lump length, cm
$Z(r)$	characteristic impedance of the radial line, ohms
$Z_A,\ldots,Z_E$	discontinuity impedances, ohms
Z_{in}	calculated transformed impedance, ohms
$Z_L(\omega)$	load impedance, ohms
Z_{LR}	microstrip connector discontinuity impedance, ohms
$Z_0,\ldots,Z_5$	characteristic impedance of transmission line sections, ohms
α	ionization coefficient for holes and electrons, cm^{-1}
ϵ	dielectric permittivity, $F\ cm^{-1}$
$\underline{\phi}$	parameter vector in the search routine
$\underline{\underline{\Phi}}(t,t_0)$	state transition matrix
θ	taper of the chip, radians
θ_R	relative phase shift, degrees
ρ	charge density, $coulomb\ cm^{-3}$

$\Gamma(\omega)$ reflection coefficient at a frequency of ω rad sec^{-1}

$\underline{\Gamma}_k(\phi)$ reflection coefficient at the kth data point

ω_a avalanche frequency, rad sec^{-1}

ω_N equivalent noise bandwidth, cycles sec^{-1}

CHARACTERIZATION AND DESIGN OF IMPATT DIODES AND ASSOCIATED CIRCUITS

by

A.E. Winter

ABSTRACT

IMPATT diode and microwave circuit interactions at X-band are examined by means of state space techniques. Complexity of circuit formulation is found to limit the usefulness of state space representation as the standard method of device/circuit analysis.

A small-signal lumped model for the IMPATT diode is extended to a nonuniform cross-section chip. This model is used in a characterization method to obtain the parameters of both the chip model and the package equivalent circuit by computer search. At current densities higher than 550 A cm^{-2} the simple lumped model requires improvement.

A design procedure is presented for a microstrip IMPATT diode oscillator and the frequency of operation is predicted to within 3%. The effects of the diode reference plane and the microstrip-to-coaxial-line connector are significant.

The gain and phase shift of a coaxial IMPATT diode amplifier is predicted from the lumped model and experimentally verified. The noise figure of the amplifier, measured as 35 dB, indicates a limitation of the IMPATT diode in many communications systems.

1. INTRODUCTION

1.1 THE PROBLEM

Rapid development of microwave techniques based on solid state devices has exposed the need for an overall approach to the design process. While there have been many papers on the detailed behavior of particular devices and, on the other hand, many descriptions of their applications there has been a significant lack of published information on the interaction of device and circuit.

This report presents an integrated approach to the application of a small-signal lumped model for the IMPATT diode to the design of active microwave circuits.

1.2 HISTORICAL BACKGROUND

In 1954, Shockley [1] first demonstrated that a negative resistance device could be implemented by the use of transit-time effects. In the transistor-like pnp structure Shockley proposed, the negative resistance is produced from a phase lag of the externally induced current with respect to the voltage, caused by the diffusion time of the carriers across the base region. Four years later, Read [2] predicted microwave oscillations from an $n^+pi\ p^+$ diode in which the phase lag between the current through the diode and the voltage across it is produced by the generation of carriers by impact ionization and by transit-time effects. Figure 1.1 shows the diode structure, the field distribution, the applied a.c. voltage, the charge distribution and the resulting external current.

However, semiconductor technology had to be improved before the device was fabricated in 1965 by Lee and others [3]. Also in 1965, Johnston et al. [4] reported microwave oscillations at 10 GHz from a pn junction which was reverse-biased into avalanche breakdown. This result indicated that a Read structure is not necessary to obtain a microwave negative resistance diode. Misawa [5] obtained computer solutions for the small-signal impedance of negative resistance avalanche diodes with a wide range of doping profiles and found them to be qualitatively similar. Thus, all of these junction devices, including the Read diode, have come to be known as Impact Ionization Avalanche Transit Time or IMPATT diodes.

The operation of an IMPATT diode is governed by three equations: the continuity equations for holes and electrons and Poisson's equation.

The one dimensional continuity equations include terms due to the carrier generation by impact ionization:

$$\frac{\partial p}{\partial t} = -\frac{1}{q} \cdot \frac{\partial J_p}{\partial x} + \alpha_p\ p\ v_p + \alpha_n\ n\ v_n \tag{1.1}$$

and

$$\frac{\partial n}{\partial t} = \frac{1}{q} \cdot \frac{\partial J_n}{\partial x} + \alpha_p\ p\ v_p + \alpha_n\ n\ v_n \tag{1.2}$$

READ DIODE

| N⁺ | P | I | P⁺ |
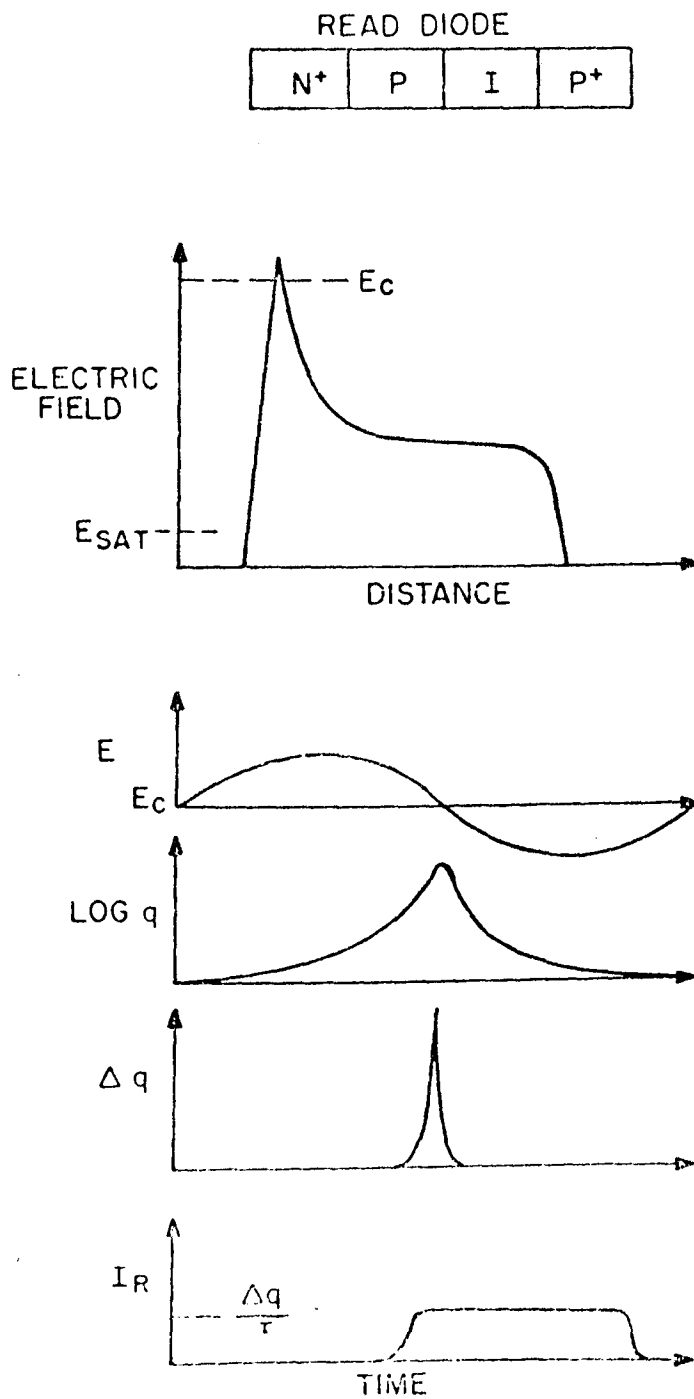
Figure 1-1. The Read Diode Structure, Field Distribution (E(x)),
Applied Electric Field (E), Charge Distribution (q) and
External Current (I$_R$).

Poisson's equation can be written

$$\frac{\partial E}{\partial x} = \frac{q}{\varepsilon} (N_D - N_A + p-n) \qquad (1.3)$$

where

p   is the hole density (cm^{-3})

n   is the electron density (cm^{-3})

q   is the electronic charge (C)

J_p is the hole current density (A cm^{-2})

J_n is the electron current density (A cm^{-2})

v_p is the hole velocity (cm sec^{-1})

v_n is the electron velocity (cm sec^{-1})

α_p is the ionization rate for holes (cm^{-1})

α_n is the ionization rate for electrons (cm^{-1})

N_D is the donor density (cm^{-3})

N_A is the acceptor density (cm^{-3})

and ε is the dielectric constant (F cm^{-1}).

These equations neglect the effect of carrier generation and recombination through defects.

Read used several assumptions to obtain a closed form solution for the small-signal admittance of the diode. The diode was assumed divided into a narrow avalanche region in which the conduction current was constant with distance through the region, and a drift region in which the carriers were assumed to travel with equal saturated velocities. Also, the ionization rates for holes and electrons were assumed equal. Gilden and Hines [6] obtained a simple equivalent circuit for the diode by assuming a small transit time of the drift region. Fisher [7] generalized the small-signal analysis by removing the restrictions of equal saturated drift velocities for holes and electrons and equal ionization rates. Also, in this analysis, the narrow avalanche region could be placed at any point in the depletion region. Gummel and Scharfetter [8] produced a small-signal analysis in which the avalanche region was a significant fraction of the total space charge region of the diode.

Several large-signal analyses have been undertaken which provide insight into the nonlinear properties of the IMPATT diode. Evans and Haddad [9] produced qualitative results by the use of Read's assumptions and the additional assumption of a small transit time in the drift region. Kuvas and Lee [10] considered unequal saturated velocities and unequal ionization coefficients for holes and electrons, while Schroeder et al. [11] considered unsaturated velocities of the carriers and predicted output power saturation. In 1969, large scale simulations on a digital computer were carried out by Scharfetter and Gummel [12]. They considered the variation of mobility as a function of electric field and doping density, the generation and recombination of the carriers due to impact ionization and defects, and both cases separately for holes and electroncs. Although these simulations probably give the most accurate and detailed theoretical solutions to the large-signal operating conditions, the large computational time necessary generally precludes detailed studies of the operating characteristics under a wide range of parameter variations. Since 1969, the IMPATT diode analyses have generally attempted to reduce the computational time for solution [13] [14], without causing a significant reduction in accuracy.

In 1967 an "anomalous mode" was reported by Prager et al. [15], who experimentally found a high efficiency (60%) mode of operation under pulsed conditions. Scharfetter, Bartelink, Gummel and Johnston [16] simulated this mode which they termed the "TRAPATT" mode for Trapped Plasma Avalanche Triggered Transit. They postulated a travelling "avalanche shock front" which leaves behind it a region of high carrier concentration and low field. This plasma is initially trapped but recovers to the initial state and the process is repeated. A typical TRAPATT diode structure and the voltage and current waveforms are shown in Figure 1.2 [17].

The traditional contender with the avalanche diode in microwave applications is the Gunn diode [18], (a "transferred electron device"), which achieves negative resistance by the use of the negative differential mobility of electrons in Gallium Arsenide and related compounds. The Gunn diode can operate in one of several modes:

a) the transit time mode;

b) the quenched mode;

c) the limited space charge accumulation mode;

or d) the hybrid mode.

Although structurally simpler than the avalanche diode, the Gunn diode requires very pure material and n⁺GaAs contacts (Figure 1.3). The diode also is limited in CW output by heat dissipation problems.

A new class of microwave diodes was indicated by Coleman and Sze [19] in 1971 and were called BARITT diodes, for Barrier Injected Transit Time. Carriers travel across the drift region, similar to that of the IMPATT diode, but the carriers are produced by minority carrier injection of the forward biased junction (or by a metal semiconductor junction) rather than by the avalanche process. A typical BARITT diode structure and the associated electric field are shown in Figure 1.4.

a)

b)
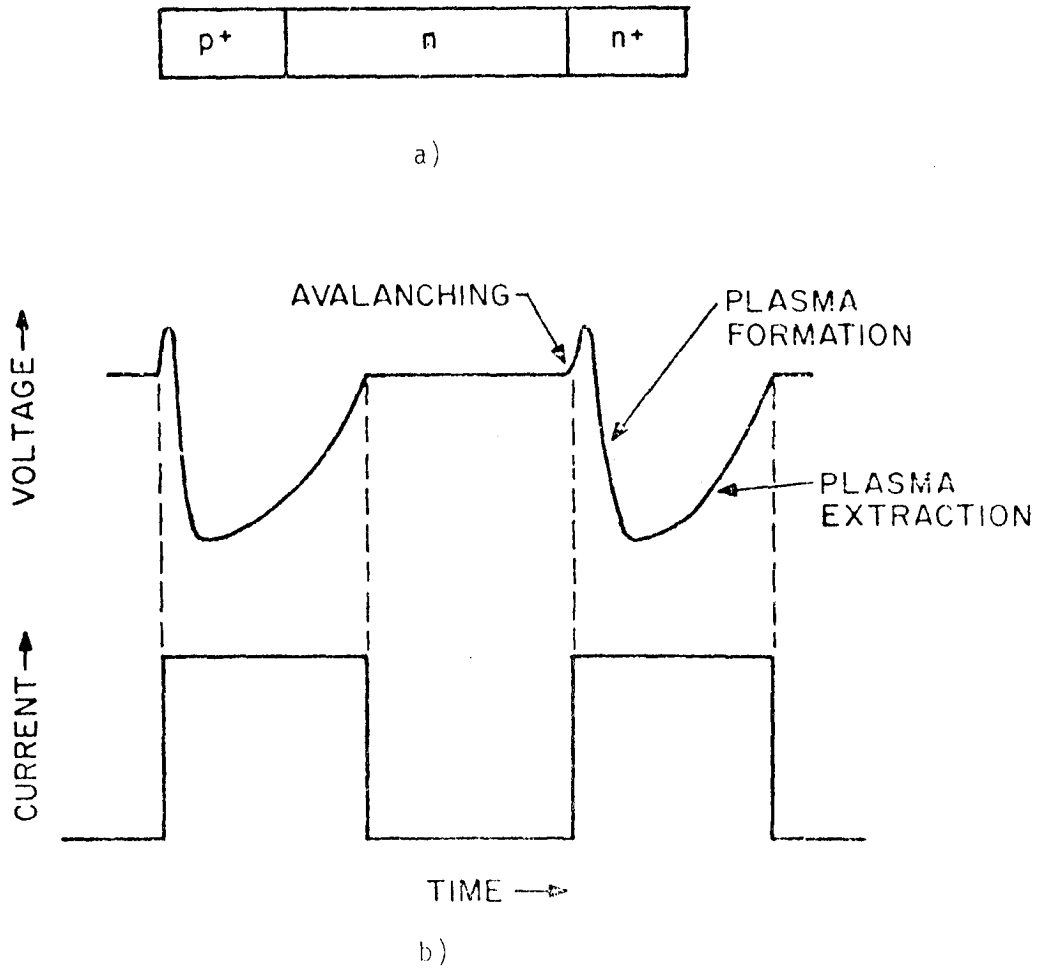
a) The structure,

b) Voltage and current waveforms.

Figure 1.2. The TRAPATT Diode.
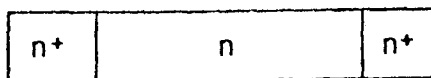
Figure 1.3.   GaAs Gunn Diode with n⁺ Contacts.
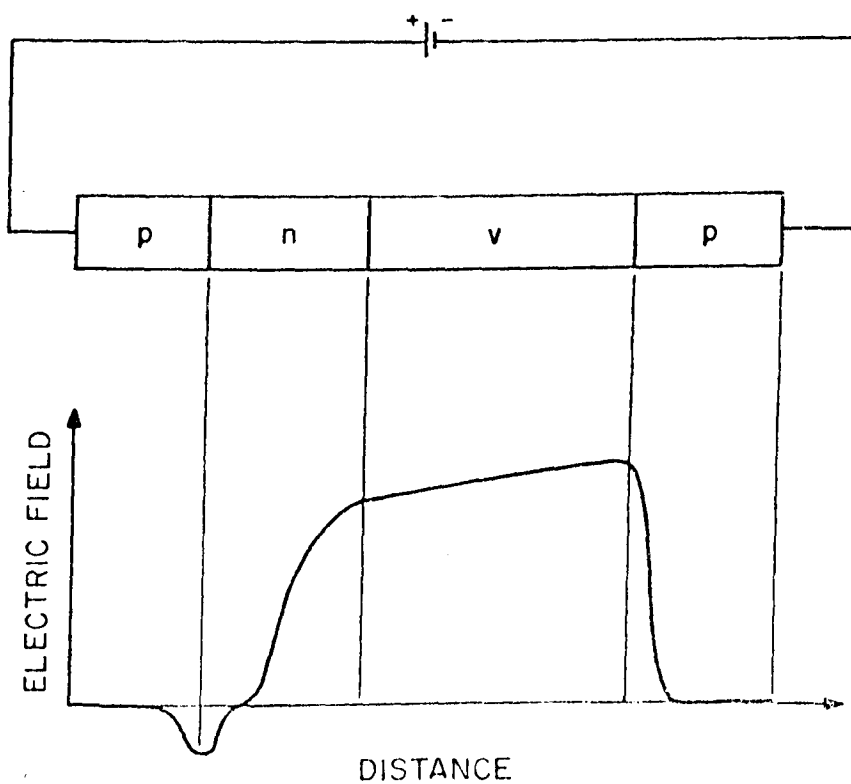
Figure 1.4.   A BARITT Diode and the Associated Electric Field.

Table 1.1 summarizes the advantages, disadvantages and typical applications of the IMPATT, TRAPATT, Gunn and BARITT diodes [17]. The comparisons are made for frequencies above L-band, as transistors are preferred for most suitable applications at L-band and lower frequencies.

1.3 METHODS OF ANALYSIS

The prediction of the operating characteristics of IMPATT diodes in microwave circuits requires the use of a model for the diode. The observable terminal characteristics are governed by mathematical expressions which involve the "parameters" of the model. The values of the physical parameters for a particular diode are often difficult to obtain accurately in which case the design of IMPATT diode circuits and systems does not require highly complex diode models. Thus, standard and simple methods for the determination of diode parameters, including the package parameters, are needed, which are also consistent with the predicted performance of the associated circuitry. The IMPATT diode models that have been used up to the present range from the Gilden and Hines [6] simple lumped element model to the extensive computer simulations of Scharfetter and Gummel [12] and others [14]. As the IMPATT diode has several related microwave devices, such as the BARITT diode, common computer-oriented methods of analysis resulting from broadband circuit models are required. The methods should be able to include the diode package and the effects of the real dimensions of the chip on the performance of the device.

1.4 OUTLINE OF REPORT

This report presents an overall view of the small-signal analysis and design of IMPATT diode oscillator and amplifier circuits. The lumped model of the diode was chosen as the resulting state space formulation can include the external circuit, the real geometry of the device, and perhaps be extended to other devices. Also, large-signal effects can be studied by numerical iteration of the nonlinear equations. The approach taken in the thesis is to compare the design and measurements with the predictions of the diode model wherever possible.

A short description of state space analysis is given in Chapter 2. The lumped model of the IMPATT diode as described by Conn [20] is given in Chapter 3 and the model is extended to a diode chip of varying cross-sectional areas. The chip equations are described in state space form. In Chapter 4, a discussion of the equivalent circuit of the diode package is presented. Experimental results for the parameters of the diode package and chip are also presented. A microstrip oscillator is designed and analyzed in Chapter 5 with particular reference to the microstrip connector, reference plane and discontinuities. Experimental oscillator results are given. A coaxial amplifier is discussed in Chapter 6. It is shown that the external circuit analysis is a dominant feature of the amplifier design. The noise figure of the amplifier is also measured experimentally and compared to existing noise theories. The conclusions and extensions of the report are presented in Chapter 7.

TABLE 1.1

Comparison of diode types

DIODE TYPE	ADVANTAGES	DISADVANTAGES	TYPICAL APPLICATIONS
IMPATT	1. Can be fabricated from Si, Ge, or GaAs 2. High frequency outputs (300GHz)	1. High output noise 2. High d.c. bias power is required	Oscillators and amplifiers as transmitters for millimetre wave communications systems
TRAPATT	1. High pulsed peak power output 2. High efficiency of d.c. to RF conversion	1. Complicated associated circuitry is required 2. High output noise 3. High d.c. bias power is required	Transmitters for pulsed arrays
Gunn	1. Structurally simple 2. High pulsed power output from LSA mode	1. Difficult to dissipate heat and therefore low CW power output 2. Very pure and uniform material is required	Transmitters for battery-operated radars
BARITT	1. Low output noise 2. Potentially low fabrication cost	1. Low output power	Local oscillators in communications receivers

2. STATE SPACE ANALYSIS

2.1 INTRODUCTION

Since the late 1950's, control theory has relied on state space formulation to handle multiple inputs and outputs in systems, particularly in the areas of stability and optimization theory [1,2]. State space methods were introduced into network analysis in 1957 by Bashkow [3] and later described by Kuh and Rohrer [4]. Since 1964, when Snyder [5] introduced "stochastic state space equations", a large class of problems in communication systems have been formulated in the state space representation, such as phase lock loop [6] and digital filter analysis [7].

The application of state space methods to microwave devices and networks was indicated in a comment by Murray-Lasso [8] but further implementation did not appear in the literature until Conn [9] analyzed a lumped model of a Read diode. This work was extended to PIN diodes [10] and Gunn diodes [11]. Little experimental work was undertaken to determine the required complexity of diode models for the design of microwave subsystems. The lumped modelling concept has been applied also to large-signal [12] and TRAPATT conditions [13].

This chapter summarizes the state space formulation, to which lumped modelling is particularly suited, together with its limitations. The formulation is compared to other methods on the basis of:

1) Programming and computational speed;

2) Ease of problem formulation;

3) The general applicability of the method.

2.2 DEFINITION OF STATE SPACE

The state of a system can be regarded as the minimum amount of information necessary at any time to characterize completely any possible future behavior of the system. If the state is specified at a time $t = t_o$, the behavior of the system can be predicted uniquely for any time $t > t_o$, provided that every element of the input set is known for $t > t_o$.

Assume that n "state variables" are required to characterize a given system. Then this set of state variables can be considered components of a vector $\underline{x}$, called the "state vector", and the n-dimensional space in which x_1, x_2, ..., x_n are coordinates, is defined as "state space". The systems considered are assumed to be described by sets of arbitrary order differential equations, each of which can be reduced to a set of first order differential equations. With the aid of vector and matrix notation these "state equations" can be written in systematic form [14].

2.3 THE STATE EQUATIONS

2.3.1 The Systematic Form

The state equations can be written in general

$$\dot{\underline{x}}(t) = [A(t)] \underline{x}(t) + [B(t)] \underline{u}(t) \qquad (2.1)$$

$$\underline{y}(t) = [C(t)] \underline{x}(t) + [D(t)] \underline{u}(t) \qquad (2.2)$$

where

    $x(t)$ is a state vector of dimension n

    $\dot{\underline{x}}(t)$ is the time derivative of $\underline{x}(t)$

    $[A(t)]$ is an n x n square matrix

    $\underline{u}(t)$ is the control vector of input variables and has a dimension of m

    $[B(t)]$ is an n x m matrix

    $\underline{y}(t)$ is the output vector of dimension b

    $[C(t)]$ is a b x n matrix

    $[D(t)]$ is a b x m matrix.

2.3.2 Solution of the Systematic Form

Now,

$$\dot{\underline{x}}(t) = [A(t)] \underline{x}(t) + [B(t)] \underline{u}(t) \qquad (2.3)$$

and the initial conditions $\underline{x}(t_o)$ are known. A fundamental nxn matrix $\Phi(t,t_o)$ is defined such that

$$\frac{d}{dt} [\Phi(t,t_o)] = A(t)\Phi(t,t_o) \qquad (2.4)$$

where

$$\Phi(t_o,t_o) = [I] \qquad (2.5)$$

and $[I]$ is the identity matrix.

12

The solution of eqn. (2.4) is given by [15]

$$\underline{x}(t) = \Phi(t,t_o) \, \underline{x}(t_o) + \int_{t_o}^{t} \Phi(t,\tau) \, [B(\tau)] \underline{u}(\tau) \, d\tau \qquad (2.6)$$

It can be seen from eqn. (2.6) that the solution of the vector equation is made up of a homogeneous solution $(\Phi(t,t_o)\underline{x}(t_o))$ and a particular solution.

In the case of a linear, time-invariant system the solution can be simplified.

The systematic form becomes

$$\dot{\underline{x}}(t) = [A]\underline{x}(t) + [B]\underline{u}(t) \qquad (2.7)$$

and

$$\dot{\underline{x}}(t) - [A]\underline{x}(t) = [B]\underline{u}(t). \qquad (2.8)$$

Multiplying both sides of eqn. (2.8) by $\exp(-[A]t)$ and integrating the resulting equation, we obtain

$$e^{-[A]t}(\underline{x}(t)) = \underline{x}(o) + \int_{0}^{t} e^{-[A]\tau} \, [B]\underline{u}(\tau) \, d\tau \qquad (2.9)$$

Thus $\underline{x}(t)$ is given by

$$\underline{x}(t) = e^{[A]t} \, \underline{x}(o) + \int_{0}^{t} e^{[A](t-\tau)} [B]\underline{u}(\tau) \, d\tau \qquad (2.10)$$

In eqn. (2.10), $\exp([A]t)$ is defined as the "state transition matrix" because it maps the state $\underline{x}(o)$ at time zero into the state $\underline{x}(t)$ at time t for the free motion of the system.

Note that $\exp([A]t)$ is defined as

$$e^{[A]t} = [I] + [A]t + \frac{[A]^2 t^2}{2!} + \ldots + \frac{[A]^k t^k}{k!} + \ldots \qquad (2.11)$$

where [I] is the identity matrix of order n.

2.3.3 The Laplace Transform Frequency Domain Solution

Consider the system

$$\dot{\underline{x}}(t) = [A]\underline{x}(t) + [B]u(t) \qquad\qquad (2.12)$$

$$\underline{y}(t) = [C]\underline{x}(t) + [D]u(t) \qquad\qquad (2.13)$$

Taking the Laplace Transform of each side of eqn. (2.12) and assuming zero initial conditions, we get

$$s\underline{X}(s) = [A]\underline{X}(s) + [B]\underline{U}(s) \qquad\qquad (2.14)$$

where $\quad s = \sigma + j\omega \qquad\qquad (2.15)$

σ is the decay constant,

ω is the frequency of operation,

$\underline{X}(s)$ is the Laplace Transform of $\underline{x}(t)$,

and $\quad \underline{U}(s)$ is the Laplace Transform of $\underline{u}(t)$.

Thus

$$\underline{X}(s) = (s[I] - [A])^{-1} [B]\underline{U}(s) \qquad\qquad (2.16)$$

Note that the poles of the system are the eigenvalues of the matrix [A].

From the output eqn. (2.13)

$$\underline{Y}(s) = [[C] (s[I] - [A])^{-1} [B] + [D]]\underline{U}(s) \qquad\qquad (2.17)$$

which gives the *transfer function* matrix between $\underline{Y}(s)$ and $\underline{U}(s)$.

For any given complex frequency s the solution for $\underline{X}(s)$ and $\underline{Y}(s)$ can be obtained from standard matrix inversion and multiplication computer programs.

2.4 LUMPED MODELLING

2.4.1 An Example

Figure 2.1 shows a typical distribution of charge density, Q(x) through a length W of semiconductor, in one dimension, at some instant of time. One approximation to this distribution is also shown, where

$$Q_L = \frac{Q_{n-1} + Q_n}{2} \qquad (2.18)$$

for each lump.

In general, the equations for each lump are simpler in form than for the complete system, but there is a correspondingly greater number of equations. It is also obvious that the greater the number of lumps the closer the approximate distribution approaches the original distribution. The balance between the increased number of equations and the approximation error is fundamental to lumped modelling.
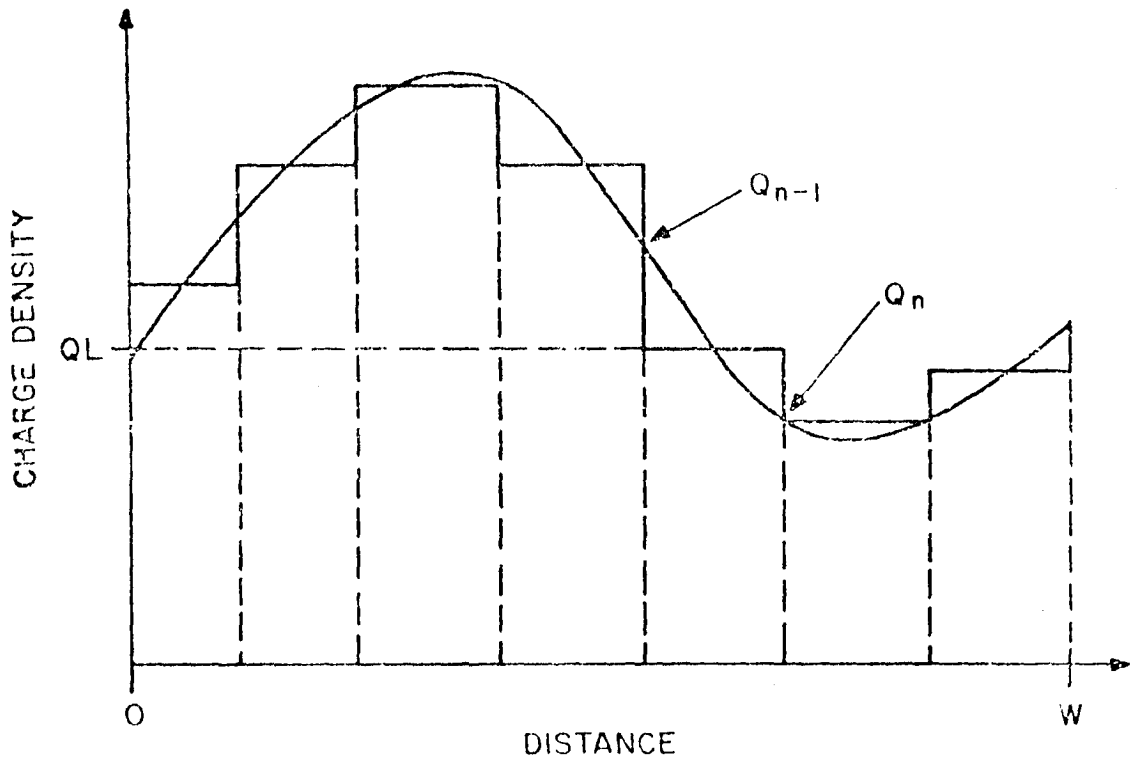
Figure 2.1. A Typical Charge Density Distribution (Q(x)) in a Semiconductor and a Lumped Model Approximation.

In the case given above, the charge density is related to the electric field in each lump by a first order differential equation, Gauss' Law, which can be written

$$\varepsilon \frac{\partial E(x)}{\partial x} = Q(x) \qquad (2.19)$$

where

      ε is the dielectric constant of the semiconductor,

and $E(x)$ is the electric field.

Thus $E(x)$ is a continuous function which can be approximated in lumped form as

$$\varepsilon \left[E(x)\big|_n - E(x)\big|_{n-1} \right] = \Delta x Q_L \qquad (2.20)$$

where Δx is the lump width.

In this example, an arbitrary charge distribution $Q(x)$ is simply represented by lumps of constant charge density. In the whole semiconductor, the electrical behavior is represented by a set of first order differential equations, conveniently written and solved in state space form.

2.4.2 Advantages of State Space Formulation

1. The representation of first-order differential equations in state space form leads to standardization of methods for solution on a digital computer. These methods involve common programs which manipulate matrices. Increasing the complexity of the model or circuit does not involve more complex methods for solution.

2. The technique does not require the use of equivalent circuit elements in the frequency domain which are frequency dependent.

3. The eigenvalues of the characteristic matrix give the natural frequencies of the system and provide information on particular modes of the system which might be excited.

4. Lumped modelling can be applied to devices of arbitrarily varying cross-section in the direction of propagation, similar in concept to the case of non-uniform transmission lines.

5. Formulation of the system as a set of first order differential equations can lead to a simple simulation on an analog computer.

2.4.3 Limitations of State Space Formulation

1. A sharp current pulse or domain travelling through the bulk
    semiconductor requires many lumps in order to reproduce the shape
    of the pulse or domain. In Figure 2.2, the pulse of charge is
    lost if the lump width exceeds that of the pulse.

    This effect has been observed in the simulation of a Gunn diode
    [16]. An alternative but complex scheme is to vary the lump
    widths inversely with the rate of change of charge density in
    the device.

2. Large-signal simulation of IMPATT diodes has been carried out
    numerically by use of the Runge-Kutta method on the set of first
    order differential equations resulting from the state space
    formulation. Instabilities in the iteration method have been
    observed for high current densities and low operating frequencies
    [17]. Therefore the method of solution must be carefully chosen.

3. For a simple model of an IMPATT diode or microwave device, the
    analytic expression for impedance can prove to be a simpler
    computational task, requiring less computer time, than the
    corresponding solution of the model which is formulated in state
    space. This has been found in the case of the Gilden and Hines
    model of the IMPATT diode.

4. Transmission lines can be represented in state space notation by
    equivalent circuit elements. However, over a wide range of
    frequencies, significant error can result from the use of simple
    lumped equivalent circuits.

5. For the simple analog computer circuits obtained from IMPATT
    lumped models, the very large dynamic range of avalanche current
    is found to limit the accuracy of analog models [18].

3. THE DIODE MODEL

3.1 INTRODUCTION

Since Read [1] proposed a microwave avalanche diode in 1958 there have
been numerous observations of IMPATT behavior in various diode structures.
Most IMPATT diodes are fabricated to exhibit a localized avalanche region
and in this case the Read model approximately predicts their terminal
characteristics. Gilden and Hines [2] simplified Read's assumptions and
produced a small-signal analysis. Conn [3] formulated a lumped model of the
Read diode and compared the chip impedance to the results of Gilden and Hines.

The lumped model is presented in this chapter and extended to a diode
of varying cross-sectional area [4]. State space formulation of the lumped
model provides a method of analysis that can be extended easily to include
the external circuit [5]. A three element equivalent circuit for the package
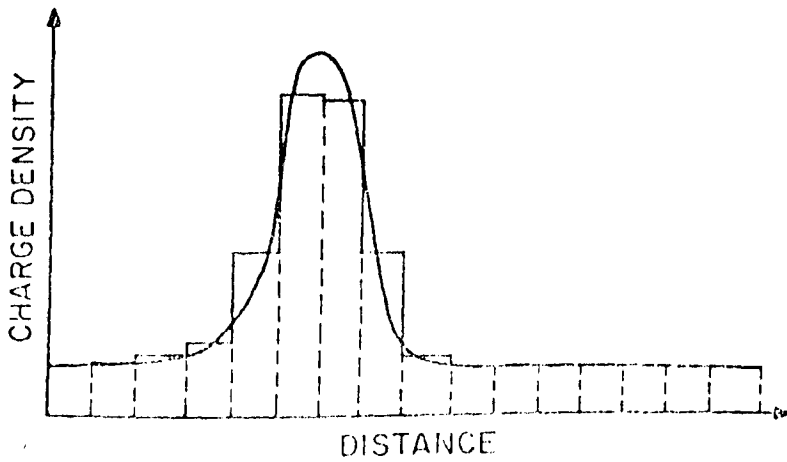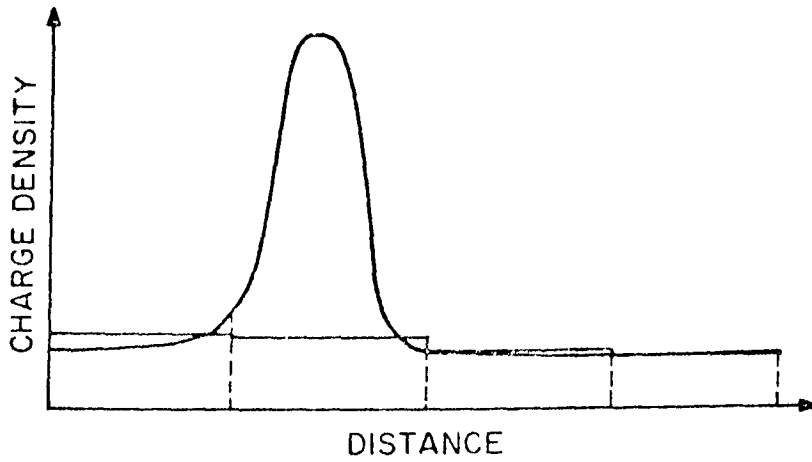
Figure 2.2. Effect of Lump Width on the Approximate
Profile of the Charge Density.

is considered and included in the state-space equations for the diode package complex.

3.2 THE CHIP

3.2.1 The Small Signal Lumped Model

The chip is shown in Figure 3.1 to be a flip-chip mesa structure, and the doping regions are indicated in Figure 3.2. The resulting electric field profile (Figure 3.3) is approximated by the lumped model electric field profile shown.
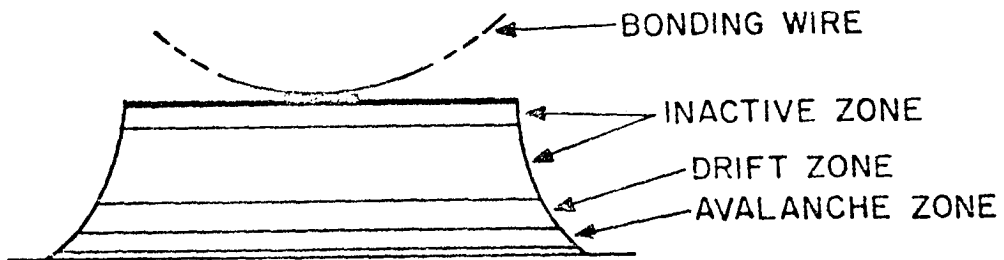
Figure 3.1. Flip-Chip Mesa Structure of the IMPATT Chip.
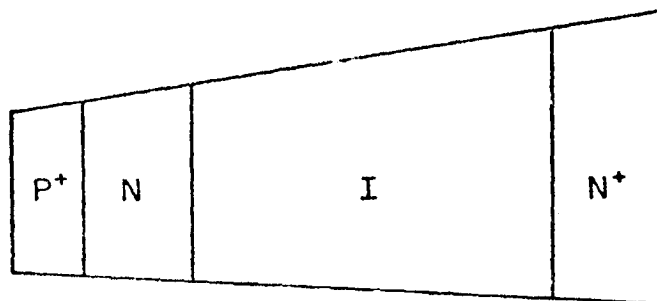
Figure 3.2. Doping Regions of the Chip.
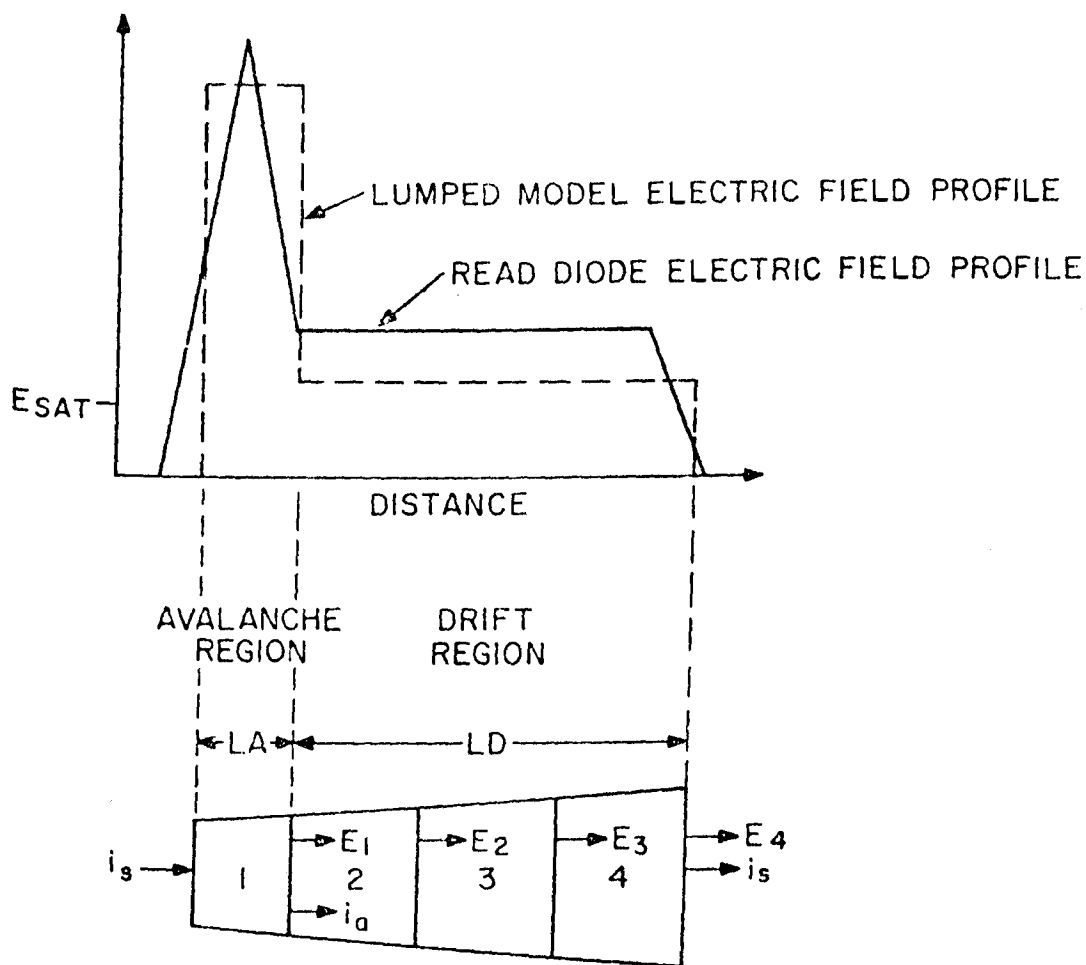
Figure 3.3. *Electric Field Profile and Lumped Model of a Tapered Chip.*
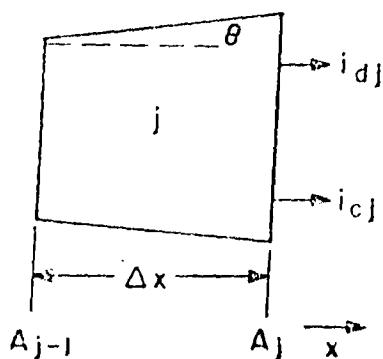
Figure 3.4. *One Drift Lump.*

Assumptions in the small-signal model are:

1) Avalanche is confined to the narrow region of maximum electric
    field.

2) The carriers appear at the edge of the avalanche region without
    delay.

3) The conduction current consists of electrons only.

4) Space charge effects in the avalanche zone are neglected.

5) There is saturation in the drift velocity of the carriers in transit
    across the drift zone.

6) Outside the depletion region the bulk semiconductor acts as a
    parasitic resistance.

It has been found [3] that the four-lump model (Figure 3.3) adequately
compares with the analytic analysis of the chip. E_1, E_2, E_3 and E_4 are the
small-signal electric fields in the chip, i_s is the total ac current through
the chip and i_a is the avalanche current.

The physical parameters of the chip model are

v = saturated drift velocity

L_D = drift region length

Δx = length of each drift region lump

L_A = avalanche region length

$A_1,\ldots,A_4$ = areas of cross-section of the diode

α' = $d\alpha/dE$ where α is the ionization coefficient for electrons.

Read has shown,

$$\frac{dI_a}{dt} = \frac{2I_a}{\tau_a} \left[\int_o^{L_A} \alpha.dx - 1 \right] \tag{3.1}$$

where τ_a is the transit time in the avalanche zone and I_a is the total
avalanche current.

Gilden and Hines simplified this equation for small signals to

$$\frac{di_a}{dt} = 2\overline{\alpha}^{\tau} \, v \, I_o E_1 \tag{3.2}$$

where

$$I_a = I_o + i_a \tag{3.3}$$

and I_o is the dc bias current

$\overline{\alpha}$ is the average value of α in the avalanche zone.

3.2.2 Analysis of a Lumped Model for a Tapered Chip

From Gauss' Law, for any volume v enclosed by a surface S

$$\oint_S D.ds = \int_v \rho \, dv \tag{3.4}$$

where D is the electric flux density, and ρ is the charge density in the volume v, or,

$$\frac{\partial E}{\partial x} + \frac{\partial E}{\partial y} + \frac{\partial E}{\partial z} = \frac{\rho}{\varepsilon} \tag{3.5}$$

where ε is the dielectric constant.

Note that the assumption of one-dimensional current flow is an approximation to the actual case of time-varying magnetic fields, electric fields and terminal current [3]. Consideration of one-dimensional current flow in a tapered chip (for $\theta \ll 1$ radian) does not introduce further assumptions.

Thus

$$\frac{E_j - E_{j-1}}{\Delta x} = \frac{2q_j}{\varepsilon.\Delta x. \, (A_{j-1} + A_j)} \tag{3.6}$$

where

$$q_j = \frac{A_j + A_{j-1}}{2} \cdot \varepsilon \cdot (E_j - E_{j-1}), \quad j = 2,3,4 \tag{3.7}$$

The conduction currents are given by

$$i_{cj} = \frac{v}{2\Delta x} (q_j + q_{j+1}), \quad j = 2,3 \tag{3.8}$$

$$i_{c4} = \frac{v}{\Delta x} (q_4) \tag{3.9}$$

From current continuity

$$i_s = i_a + \varepsilon A_1 \dot{E}_1 \tag{3.10}$$

and

$$i_s = \frac{V_2 - V_D}{R_s}$$

where R_s is the parasitic resistance associated with the chip, and V_2 is the voltage across the chip and R_s. The diode voltage, V_D, is given by

$$V_D = \left[\left(L_A + \frac{\Delta x}{2} \right) E_1 + \Delta x E_2 + \Delta x E_3 + \frac{\Delta x}{2} E_4 \right] \tag{3.11}$$

and

$$\dot{E}_1 = -\left[\frac{\left(L_A + \frac{\Delta x}{2} \right)}{\varepsilon . R_s . A_1} \right] E_1 - \left[\frac{\Delta x}{\varepsilon . R_s . A_1} \right] E_2 - \left[\frac{\Delta x}{\varepsilon . R_s . A_1} \right] E_3$$

$$- \left[\frac{\Delta x}{2\varepsilon . R_s . A_1} \right] E_4 - \frac{i_a}{\varepsilon . A_1} + \frac{V_2}{\varepsilon . R_s . A_1} \tag{3.12}$$

From current continuity, and applying eqns. (3.6) to (3.11)

$$\dot{E}_2 = \left[\left(\frac{v}{2\Delta x} \right) \left(\frac{A_{15}}{A_2} \right) - \frac{\left(L_A + \frac{\Delta x}{2} \right)}{\varepsilon R_s A_2} \right] E_1 - \left[\frac{\Delta x}{\varepsilon R_s A_2} + \frac{v}{2\Delta x} \frac{A_1 - A_3}{2A_2} \right] E_2$$

$$- \left[\left(\frac{v}{2\Delta x} \right) \left(\frac{A_{25}}{A_2} \right) + \left(\frac{\Delta x}{\varepsilon R_s A_2} \right) \right] E_3 - \left(\frac{\Delta x}{2\varepsilon R_s A_2} \right) E_4 + \frac{V_2}{\varepsilon R_s A_2} \qquad (3.13)$$

where

$$A_{j5} = \frac{A_j + A_{j+1}}{2} .$$

Similarly E_3 and E_4 can be obtained.

3.3 THE PACKAGE

A typical IMPATT diode package is shown in Figure 3.5, and is suited for mounting in coaxial line, reduced height waveguide, or microstrip. At the frequencies of operation (H- and X-bands) the electrical lengths of the package are small. Thus lumped elements can be used for the model of the package.
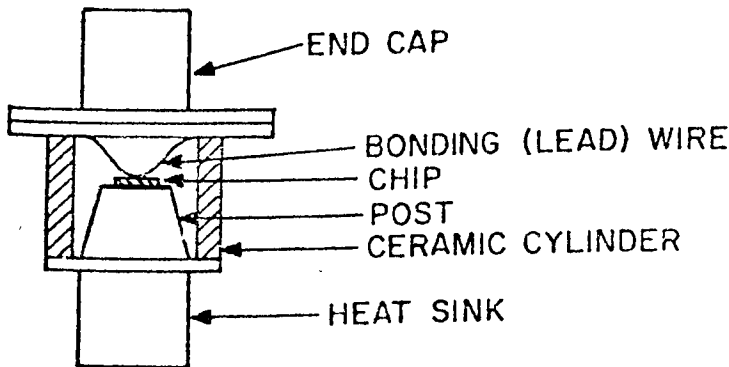
Figure 3.5. The Packaged Diode.

An equivalent circuit is discussed by Getsinger [6], who assumes a simple pi-network (Figure 3.6). More complex circuits have been used [7], [8] but at frequencies in X-band and lower, the majority of these circuits can be shown to reduce to a pi-network. For example, Figure 3.7a shows the equivalent circuit which includes the post inductance (L_B) and the capacitance between the lead wires and the post (C_c). The pi-equivalent circuit of Figure 3.7d is obtained by the exchange of elements in the same branch and the assumption that:

$$2\omega^2 \; L_B C_B \;<< \; 1 \tag{3.14}$$

In this case, the three element equivalent circuit represents the package behavior, but the elements do not necessarily correspond to defined configurations in the package.

THE MOUNT   THE PACKAGE   THE CHIP
AND EXTERNAL
CIRCUIT
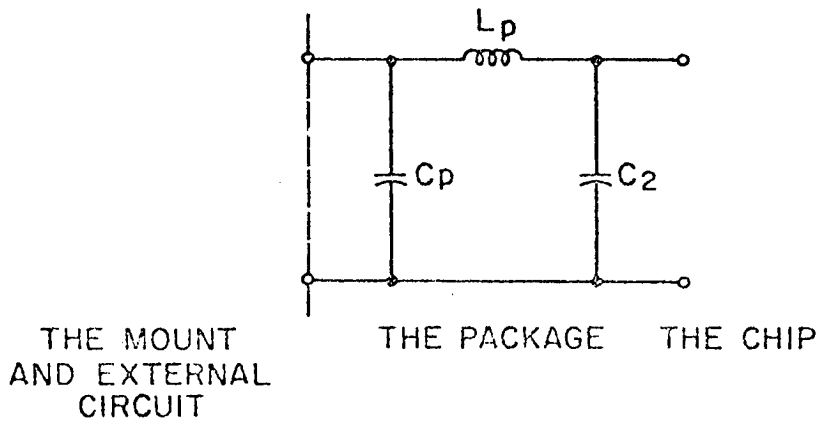
Figure 3.6. The Package Equivalent Circuit.

From Figure 3.7d,

R_s includes both the losses in the semiconductor chip and the losses in the package

and u(t) is an input current generator. The state equations for the package are

$$C_p \; \dot{v}_{C1} = - \; i_L + u(t)$$

$$\dot{v}_{C1} = - \frac{i_L}{C_p} + \frac{u(t)}{C_p} \tag{3.15}$$
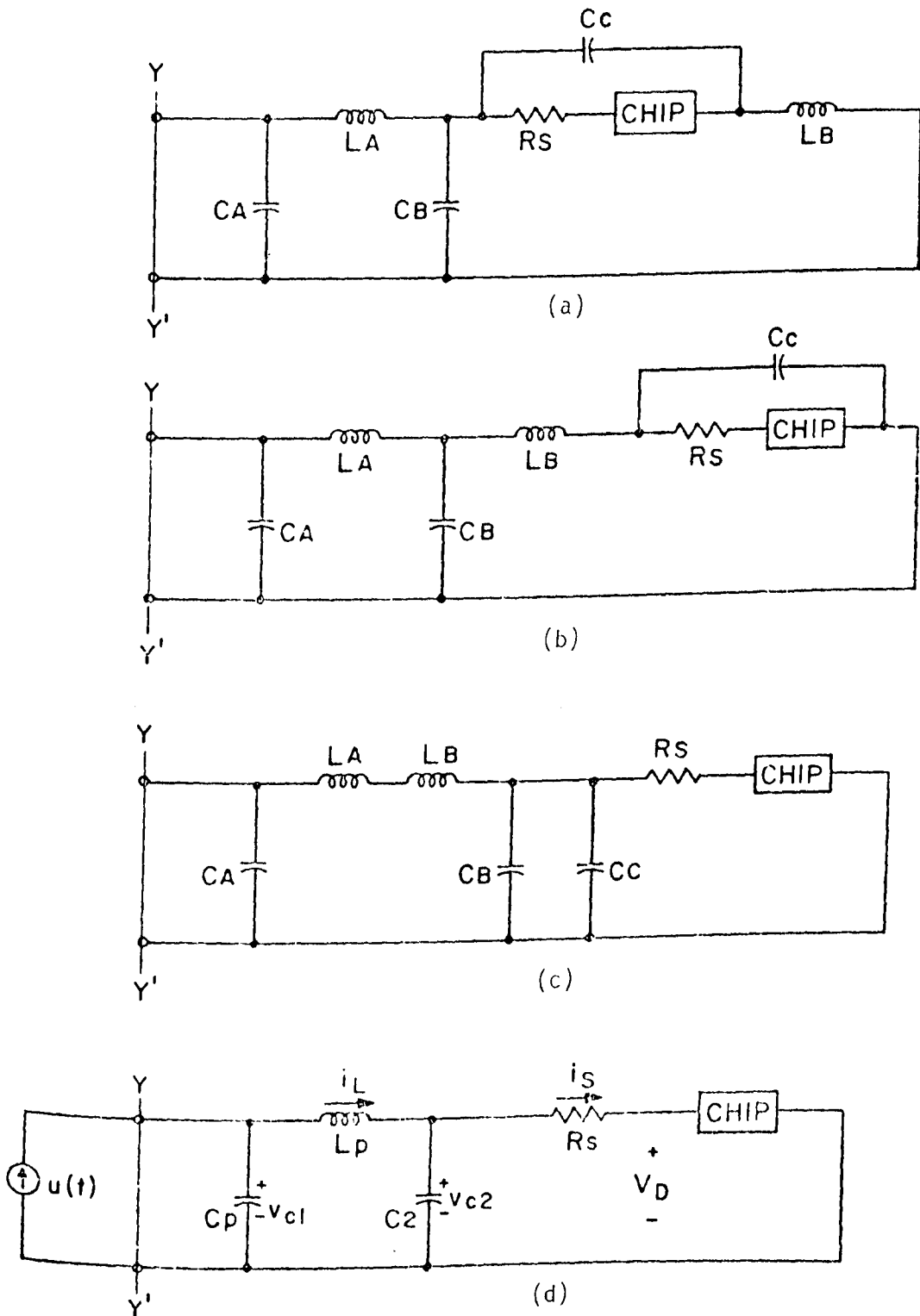
Figure 3.7. The Reduction of a Complex Package Equivalent Circuit Where, $C_p = C_A$, $L_p = L_A + L_B$, $C_2 = C_B + C_c$.

$$C_2 \, \dot{v}_{C2} = i_L + \frac{V_D - v_{C2}}{R_s}$$

$$\dot{v}_{C2} = \frac{i_L}{C_2} - \frac{v_{C2}}{R_s C_2} + \frac{V_D}{R_s C_2} \qquad (3.16)$$

$$L_p \dot{i}_L = v_{C1} - v_{C2}$$

$$i_L = \frac{v_{C1}}{L_p} - \frac{v_{C2}}{L_p} \qquad (3.17)$$

3.4 THE STATE EQUATION

The differential equations for the chip and package are combined, resulting in the state equation

$$\dot{\underline{x}} = [A] \, \underline{x} + \underline{B} \, u(t) \qquad (3.18)$$

where

$$\underline{x} = \begin{bmatrix} E_1 \\ E_2 \\ E_3 \\ E_4 \\ i_a \\ v_{C1} \\ i_L \\ v_{C2} \end{bmatrix} \qquad \underline{B} = \begin{bmatrix} 0 \\ 0 \\ 0 \\ 0 \\ 0 \\ 1/C_p \\ 0 \\ 0 \end{bmatrix}$$

and $[A]$ is shown in Figure 3.8.

$-\dfrac{L_A + \Delta x/2}{\epsilon R_s A_1}$	$-\dfrac{\Delta x}{\epsilon R_s A_1}$	$-\dfrac{\Delta x}{\epsilon R_s A_1}$	$+\dfrac{\Delta x}{2\epsilon R_s A_1}$	$-\dfrac{1}{\epsilon A_1}$	0	0	$\dfrac{11}{\epsilon R_s A_1}$
$\left(\dfrac{v}{2\Delta x}\right)\left(\dfrac{A_{15}}{A_2}\right) - \dfrac{L_A + \Delta x/2}{\epsilon R_s A_2}$	$-\dfrac{\Delta x}{\epsilon R_s A_2} - \dfrac{v}{2\Delta x}\left(\dfrac{A_1 - A_3}{2A_2}\right)$	$-\left(\dfrac{v}{2\Delta x}\right)\left(\dfrac{A_{25}}{A_2}\right) - \dfrac{\Delta x}{\epsilon R_s A_2}$	$-\dfrac{\Delta x}{2\epsilon R_s A_2}$	0	0	0	$\dfrac{1}{\epsilon R_s A_2}$
$-\left(\dfrac{L_A + \Delta x/2}{\epsilon R_s A_3}\right)$	$\dfrac{v}{2\Delta x}\left(\dfrac{A_{25}}{A_3}\right) - \dfrac{\Delta x}{\epsilon A_3 R_s}$	$-\dfrac{\Delta x}{\epsilon R_s A_3} - \dfrac{v}{2\Delta x}\left(\dfrac{A_2 - A_4}{2A_3}\right)$	$-\dfrac{\Delta x}{2\epsilon R_s A_3} - \dfrac{v}{2\Delta x}\left(\dfrac{A_{35}}{A_3}\right)$	0	0	0	$\dfrac{-1}{\epsilon R_s A_3}$
$-\dfrac{L_A + \Delta x/2}{\epsilon R_s A_4}$	$-\dfrac{\Delta x}{\epsilon R_s A_4}$	$\dfrac{v}{\Delta x}\left(\dfrac{A_{35}}{A_4}\right) - \dfrac{\Delta x}{\epsilon R_s A_4}$	$-\dfrac{v}{\Delta x}\left(\dfrac{A_{35}}{A_4}\right) - \dfrac{\Delta x}{\epsilon R_s A_4}$	0	0	0	$\dfrac{1}{\epsilon R_s A_4}$
$2v\alpha' I_a$	0	0	0	0	0	0	0
0	0	0	0	0	0	$-\dfrac{1}{C_1}$	
0	0	0	0	0	$\dfrac{1}{L_p}$	0	$-\dfrac{1}{L_p}$
$\dfrac{L_A + \Delta x/2}{R_s C_2}$	$\dfrac{\Delta x}{R_s C_2}$	$\dfrac{\Delta x}{R_s C_2}$	$\dfrac{\Delta x}{2R_s C_2}$	0	0	$\dfrac{1}{C_2}$	$\dfrac{1}{R_s C_2}$

Figure 3.8. Matrix [A] of Equation 3.18

The Laplace Transform of (3.18) with zero initial conditions gives

$$X(s) = [(s[I] - [A])]^{-1} \cdot \underline{B} \cdot U(s) \qquad (3.19)$$

where $[I]$ is the unity matrix (Chapter 2). The impedance of the diode at the input reference plane is given by

$$Z_D(s) = \frac{X_6(s)}{U(s)}$$

where

$$X_6(s) = L[X_6(t)] \qquad (3.20)$$

and L is the Laplace operator.

4. CHARACTERIZATION OF THE DIODE AND PACKAGE

4.1 INTRODUCTION

Standard matrix computer programs can be used for solution when the equations for the lumped model of the chip and the package model are written in state space form. This approach is used in this chapter and a characterization method for IMPATT diodes is presented here. The method allows simple determination of the package parameters and the chip parameters of an IMPATT diode, from standard network analyzer reflection coefficient measurements. This separation of the package and chip is essential to optimize the performance of the diode over X-band.

The method in this chapter indicates that the analyzer measurement plane can be placed at the equivalent reference plane of the diode, so that the mount parameters need not be explicitly measured, and avoids the complications associated with internally short- or open-circuited packages as references. Direct search methods of parameter variation are discussed relative to the experimental accuracy required, and applied, first to the package parameters and secondly to the chip parameters. This separation reduced the number of parameters for each search routine. The variation of chip parameters with bias voltage and current showed some limitations to the lumped model assumptions.

4.2 THE REFERENCE PLANE FOR THE DIODE PACKAGE

4.2.1 Previous Work on the Diode Reference Plane

It is important to obtain an equivalent circuit for the diode package that is independent of the diode mount. The choice of a suitable reference plane for the package is complicated by the possible presence of several transmission line modes.

Getsinger [1] discussed the reference plane at the surface bb (Figure 4.1) assuming a radial transmission line mode at that surface. However, in practice, the emanating wave is a mixture of radial line and coaxial line modes that interact along the reference surface and through the plane YY^1. Therefore, the separation of package and mount equivalent circuits is difficult.

In addition, several other factors complicate the analysis:

a) losses in the mount can be significant [2];

b) a package consisting only of end caps does not provide an exact open-circuit [3];

c) the impedances of lead wires are not consistent, even in the same fabrication batch of diodes [4].

Owens [5] examined the mount equivalent circuit developed by Getsinger and presented experimentally deduced values of the mount parameters for an S_4 Package in a 7 mm coaxial line (Figure 4.2).
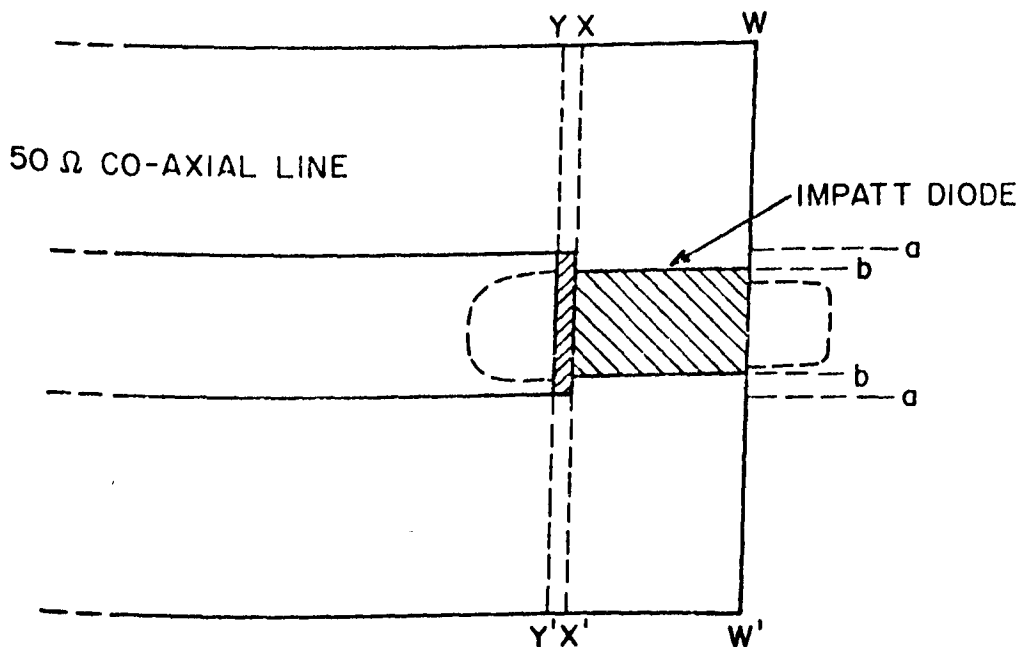
Figure 4.1. The Diode Mounted in a 50Ω Coaxial Line.

Y 0.086   0.224   a   0.109   b
      nH   nH   nH

0.010 pF   0.043 pF   0.027 pF

Y'   a   b
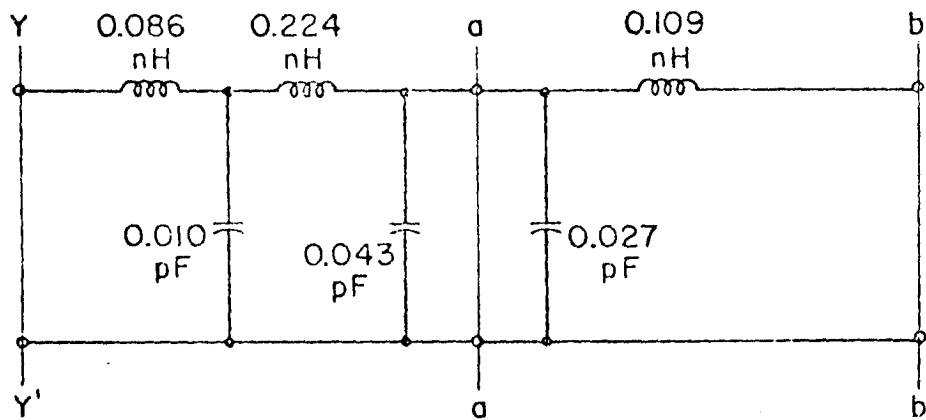
Figure 4.2.   The Mount Equivalent Circuit (Owens).

4.2.2 The Equivalent Reference Plane Approach

In this work a copper dummy diode with the external dimensions of the packaged diode was used as a short-circuit reference in the diode mount. This reference avoided the use of an open circuit, did not include lead wires but did account for the losses in the mount.

The transmission line equivalent circuit in lumped elements of the copper dummy diode is shown in Figure 4.3, from the plane YY^1 to a short circuit as the plane WW^1. The lumped elements were calculated from the coaxial impedances per unit length and included the discontinuity at the plane XX^1. The mount equivalent circuit was compared to that of Owens for a $(10 + j10)\Omega$ termination, and the resulting impedance transformations to the plane YY^1 are plotted versus frequency in Figure 4.4. There was approximately four percent difference in the transformed impedances of the equivalent circuits at 12 GHz. An examination of Figures 4.2 and 4.3 shows this difference was due to the differing distribution of capacitance, assuming no discrepancies in physical dimensions between the mounts.

Y   X   W
      0.086 nH   0.320 nH

0.016 pF 0.016 pF 0.008 pF 0.022 pF 0.022 pF

Y'   X'   W'
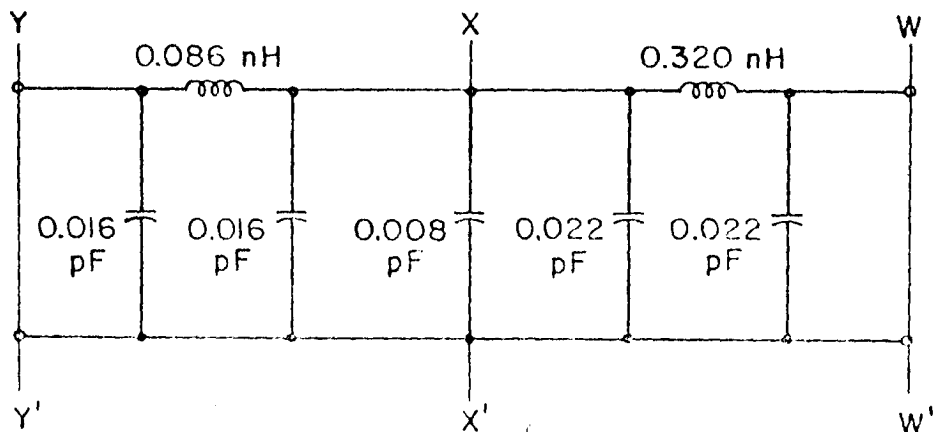
Figure 4.3.   The Mount Equivalent Circuit for the Copper Dummy Diode.
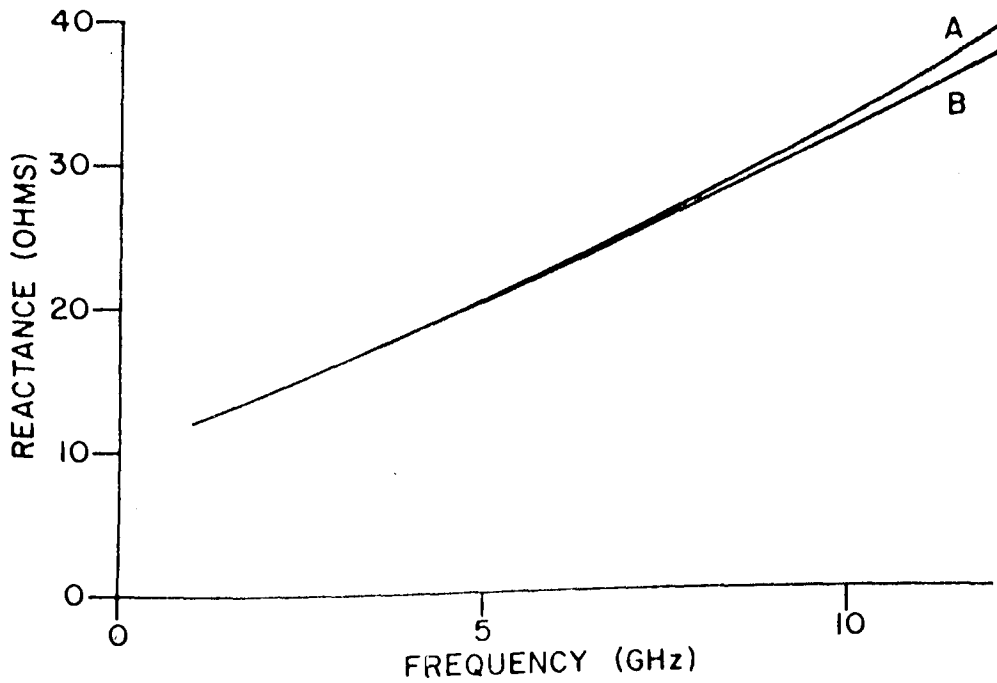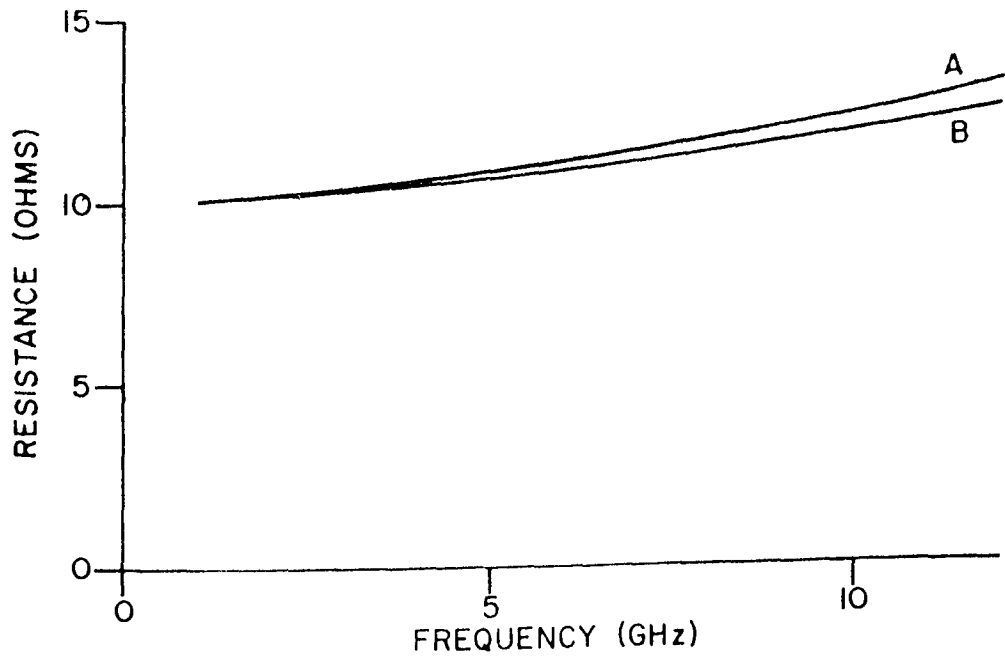
Figure 4.4. Comparison of Transformed Impedance at the Plane YY'
for a Termination of (10+j10) Ohms of the Equivalent Circuits of
Figures 4.2 and 4.3. A, Copper Dummy Diode; B, Owens' Model.

4.3 DATA ACQUISITION AND REDUCTION

The establishment of the diode reference plane allowed a direct measurement of the diode package reflection coefficient. Under several conditions of diode bias voltage and current, the reflection coefficient was measured by the use of the network analyzer. An appropriate model was chosen for the chip, depending on the bias conditions, and a parameter search routine adjusted the package and chip equivalent circuit values until a match was obtained between the measured and predicted reflection coefficients over the frequency range of interest.

4.4 PARAMETER SEARCH METHODS

4.4.1 The Objective Functions

We wish to minimize the combined objective function

$$U(\underline{\phi}) = \beta_1 \, U_M(\underline{\phi}) + \beta_2 \, U_A(\underline{\phi}) \tag{4.1}$$

where

$$U_M(\underline{\phi}) = \sum_{k=1}^{n} (|\Gamma_k^C(\underline{\phi})| - |\Gamma_k^D(\underline{\phi})|)^2 \tag{4.2}$$

$$U_A(\underline{\phi}) = \sum_{k=1}^{n} (\lfloor \Gamma_k^C(\underline{\phi}) - \lfloor \Gamma_k^D(\underline{\phi}))^2 \tag{4.3}$$

$\Gamma_k^C(\underline{\phi})$ is the calculated reflection coefficient from the appropriate model.

$\Gamma_k^D(\underline{\phi})$ is the measured reflection coefficient at the kth frequency.

β_1 and β_2 are scaling constants to equalize the effects of the angle objective functions, and

$$\underline{\phi} = \begin{bmatrix} \phi_1 \\ \cdot \\ \cdot \\ \cdot \\ \phi_N \end{bmatrix} \tag{4.4}$$

where $\phi_1,\ldots,\phi_N$ are the appropriate parameters for the package and chip.

One measure of the average error per reading (e) is given by

$$e = \left[\frac{1}{n} \sum_{k=1}^{n} \frac{|\Gamma_k^C(\phi) - \Gamma_k^D(\phi)|}{|\Gamma_k^C(\phi)|} \right] \tag{4.5}$$

where

$$\Gamma(\phi) = |\Gamma(\phi)| \underline{|\Gamma(\phi)}$$

and n is the number of data points in the operating frequency range.

Note that the objective function defined by eqn. (4.1) allowed the direct substitution of the magnitude and angle of the reflection coefficient as measured by the network analyzer.

4.4.2 The Desired Minimum

Many methods are available in the literature to minimize a function of several variables [for example [6], [7]]. Most of these methods assume that there is one desired minimum which can be reached from any initial point in the feasible region. The existence of several minima in this region can lead to non-unique solutions by minimization methods, depending on the initial point of each search. The only method currently available to check that the minimum reached by the search method is a global minimum is exhaustive enumeration, which may be implemented as either a systematic mesh search or a random search [8].

The package and chip minimizations indicated in Section 4.3 in general appeared to give unique minima, independent of the initial conditions tried. However, if it were possible to enumerate the function $U(\phi)$ at every point in the feasible region, the global minimum would appear directly. Even if the mesh width is appreciable (Figure 4.5) the method is prohibitive in length.

Sharp undesired minima have been reported, for example, from fitting a series of exponential functions (Figure 4.6) [9], but have not been observed in the package or chip minimization. The high sensitivity exhibited (i.e., the drastic change in the reflection coefficient for a small change in one of the parameters) is unacceptable to fit experimental data which can be in error up to 4%.

To further ensure that the feasible region is unimodal, an approximate knowledge of any of the parameters produced a constraint which reduced the size of the feasible region. Certainly the order of magnitude of the package parameters can be deduced from physical dimensions [10] and several chip
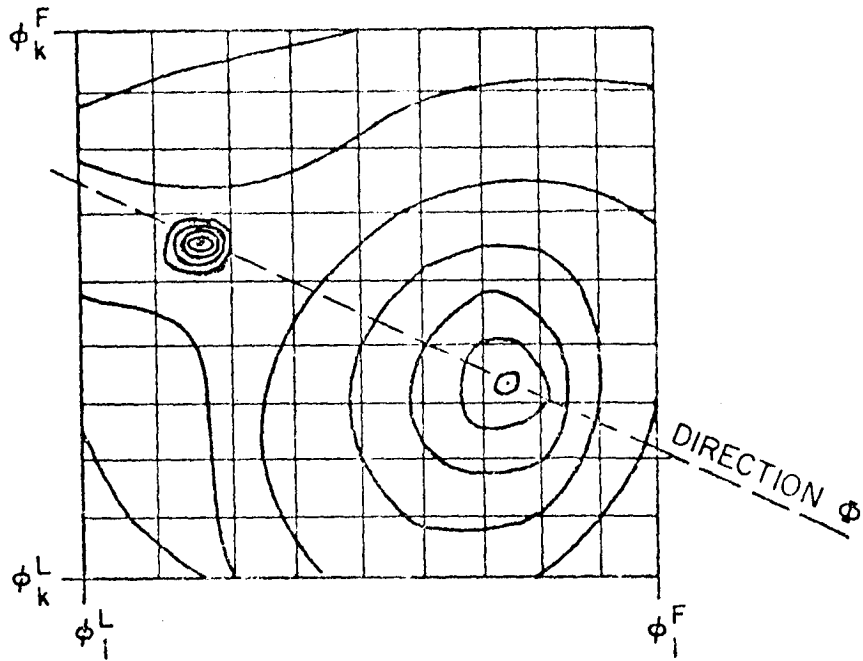
Figure 4.5. A Two-Dimensional Mesh Search Over the Feasible Region.

The Superscript L Indicates a Lower Constraint on i,k.

The Superscript F Indicates an Upper Constraint on i,k.
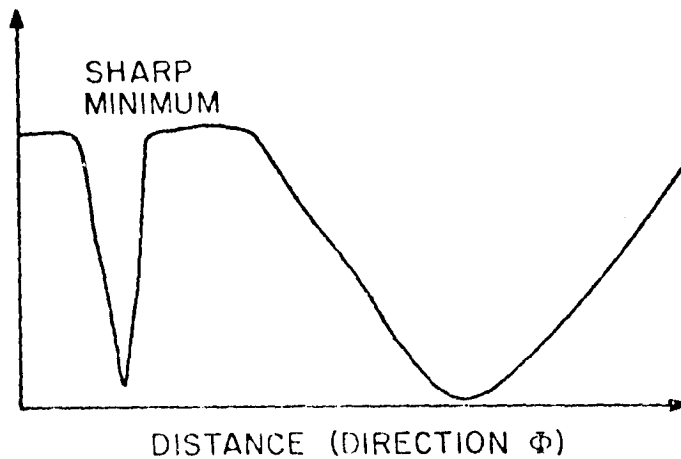
Figure 4.6. A Sharp Minimum Inside a Mesh Unit Square.

parameters can be estimated from available manufacturers' specifications, such as the substrate material or doping profile.

4.4.3 Minimization Methods

Taylor's Theorem for one dimension can be written

$$f(z) = f(a) + \frac{z-a}{1!} f(a) + \frac{(z-a)^2}{2!} \cdot f''(a) + \ldots + \frac{(z-a)^p}{p!} \cdot f^p(a) \qquad (4.6)$$

and in n dimensions can be approximated by

$$U(x_1 + \delta_1, \ldots, x_n + \delta_n)$$

$$\simeq U(x_1, x_2, \ldots, x_n) + \sum_{i=1}^{n} \delta_i g_i + \frac{1}{2} \sum_{i=1}^{n} \sum_{j=1}^{n} \delta_i G_{ij} \delta_j \qquad (4.7)$$

where

$$g_i = \frac{\partial U(x_1, x_2, \ldots, x_n)}{\partial x_i} \qquad (4.8)$$

$$G_{ij} = \frac{\partial^2 U(x_1, x_2, \ldots, x_n)}{\partial x_i \, \partial x_j} \qquad (4.9)$$

Then, at a minimum, the first derivatives are zero, and the Hessian matrix [G] is positive definite. For a quadratic objective function the approximation of eqn. (4.7) is exact, and the conjugate directions (a and b) can be defined as

$$\sum_{i=1}^{n} \sum_{j=1}^{n} a_i G_{ij} b_j = 0 \qquad (4.10)$$

or,

$$\underline{a}^T [G] \underline{b} = 0$$

Minimization methods can be classed as follows:

1) *One-at-a-time search methods* do not consider the gradient of the objective function and instead search along the parameter axes. The sectioning method, for example, searches parallel to each axis, such that

$$\nabla U(\phi_i) = 0, \qquad \text{for each } i,$$

until no further improvement is found. However this method fails if the objective function contours include a descending ridge in a direction other than one of the axes. A related method is the neighboring grid method which also saves computer time. Instead of searching the whole range of each parameter, a step size $\Delta \phi_i$ is introduced. The values of the objective function $U(\underline{\phi})$ are computed at

$$U(\phi_1, \phi_2, \ldots, \phi_i \pm \Delta \phi_i, \ldots, \phi_n) \qquad \text{for } i = 1, 2, \ldots, n.$$

The minimum value becomes the succeeding starting value, and the process is repeated until the minimum is found.

The computation time of one-at-a-time methods is highly sensitive to the orientation of the objective function contours. This effect can be partly overcome by scaling and rotating the axes of the parameters. The objective function contours are extended to approximate hyperspheres by scaling and a remaining ridge or valley is oriented along one parameter axis.

2) *Gradient methods,* such as the classical steepest descent method [11], calculate the first derivatives of the objective function (eqn. (4.8)) and arrange the direction of search accordingly. These methods are "first order".

3) *Second-order methods,* such as the Newton-Raphson method [12], calculate or approximate the first and second derivatives of the objective function (eqns. (4.8) and (4.9)). Powell's method [13] is second order, but does not require the explicit evaluation of any derivatives. The method uses conjugate directions of search relative to a quadratic objective function (eqn. (4.10)). Bandler [6] summarizes the algorithm and gives an example. Waren et al. [14] compare the method favorably with other second order methods. However, for each iteration many objective function evaluations are necessary, so that increase in computation time balances the increase in accuracy.

The inherent accuracy limits of the experimental data dictates that high accuracy of the parameter values is unrealistic. In any case, Powell's method is appropriate as an occasional check on the parameter values obtained by the simpler methods and is an illustration

of a suitable method for a more complex study of the package or
chip.

4.5 CHARACTERIZATION PROCEDURE

The method of obtaining the parameters of the complete model was
divided into two sections. First, the package parameters were determined
and secondly, with these parameters held invariant, the chip parameters were
determined. This separation allowed the use of two minimizations, each with
half the number of parameters of the complete model, and led to improved
accuracy.

To obtain the package parameters, the diode was held in reverse bias,
but not in avalanche. Under these conditions, the depletion region formed
in the diode chip was modelled as a voltage dependent capacitor in series
with the bulk resistance of the chip ($C_j(V_b)$ and $R_s(V_b)$). Over a range of
reverse bias the package parameters were assumed constant and were determined
accurately, as only two parameters were needed to characterize the chip.
Under forward bias the chip can be modelled as a resistance, which would
indicate that the package parameters could be determined from measurements
in forward bias. However, the measurements were not as consistent as in
reverse bias and were used as a check that the correct minimum was reached
by the parameter search program. Under avalance conditions the chip was
represented by the lumped model developed in Section 3.2.1.

A Hewlett-Packard network analyzer was used to measure the reflection
coefficient, with provision for digital readout, under forward or reverse
bias with the diode mounted in the test jig (Figure 4.7). Over the frequency
range of interest (7 - 11 GHz) diode oscillation was prevented by the 50 ohm
characteristic impedance of the test jig. The diode holder provided a heat
sink for the diode and the grip mechanism ensured similar mount conditions
for different diodes. The copper dummy diode (Section 4.2.2) was used as a
short circuit reference for the network analyzer. The rotation of the
reflection coefficient as measured by the network analyzer was checked by
means of a variable length air line and a coaxial precision short circuit.
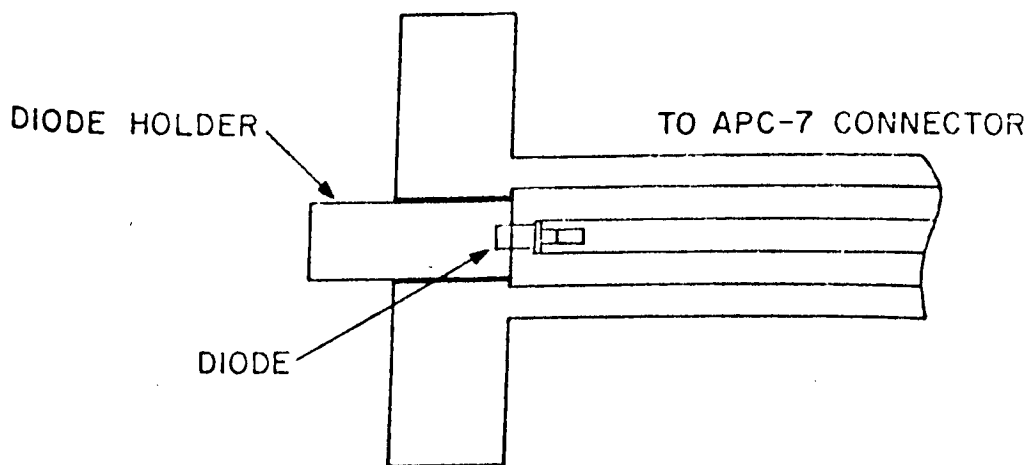
Figure 4.7. The Diode Test Jig and Heat Sink.

4.6 RESULTS

Several IMPATT diodes have been characterized. The package and chip parameters as found by the search routines are presented for three diodes, as follows.

Northern Electric diode 2/4-S4 case, N_4

Northern Electric diode 2/24-S4 case, N_{24}

Varian VAO-12C-N20/90B-2-13 N20 case, V

Table 4.1 shows the package parameters (Figure 3.6) obtained from the neighboring grid parameter search. R_s is the diode loss measured at the breakdown voltage for onset of avalanche. The chip parameters $R_s(V_b)$ and $C_j(V_b)$ obtained from the same set of measurements are shown in Figure 4.8 and 4.9. Table 4.2 indicates a measure of the average error per reading(e).

TABLE 4.1

Package Parameters

Where $R_s = R_s|$ at the Breakdown Voltage

DIODE	C_p(pF)	L_p(nH)	C_2(pF)	R_s (ohms)
N_4	0.16	0.53	0.04	4.0
N_{24}	0.15	0.41	0.07	2.5
V	0.18	0.38	0.06	2.1

TABLE 4.2

Parameter Fitting Error (e) for the Objective Function $U(\underline{\phi})$

$$\text{where } \underline{\phi} = \begin{bmatrix} C_p \\ L_p \\ C_2 \\ R_s \\ C_j \end{bmatrix}$$

	OBJECTIVE FUNCTION (percent)
N_4	5
N_{24}	4
V	4

Figures 4.8 to 4.12 show the variation of the chip parameters versus the d.c. bias voltage and current. Table 4.3 lists the values of the chip parameters that are assumed to be independent of bias current, and the parameter fitting error is tabulated for the neighboring grid search method in Table 4.4.

TABLE 4.3

Chip Parameters α' and θ

DIODE	α'	θ
N_4	0.24	$-15°$
N_{24}	0.25	$-20°$
V	0.28	$-22°$

Table 4.4

Parameter Fitting Error (e) for the Objective Function $U(\phi)$

where $\quad \phi = \begin{bmatrix} L_A(I_0) \\ L_D(I_0) \\ A_1(I_0) \\ \alpha' \\ \theta \end{bmatrix}$

	OBJECTIVE FUNCTION (percent)
N_4	7
N_{24}	5
V	7

An alternative model for the chip, under avalanche conditions of bias, is a parallel combination of bias dependent inductance and capacitance [15]. A separate parameter search method yielded values of the resonant frequency of this circuit, that are plotted against bias current in Figure 4.12.

[16] Throughout the computations the saturated drift velocity was taken as

$$v = 1.0 \times 10^7 \text{ cm sec}^{-1}.$$

A complete search with a coarse mesh in the package parameters space showed shallow local minima outside the feasible region and no improvement on the objective function minimum chosen. For equivalent accuracy and starting points the second order search method of Powell took approximately twice the computation time of the neighboring grid method. However for greater accuracy Powell's method became rapidly more efficient.
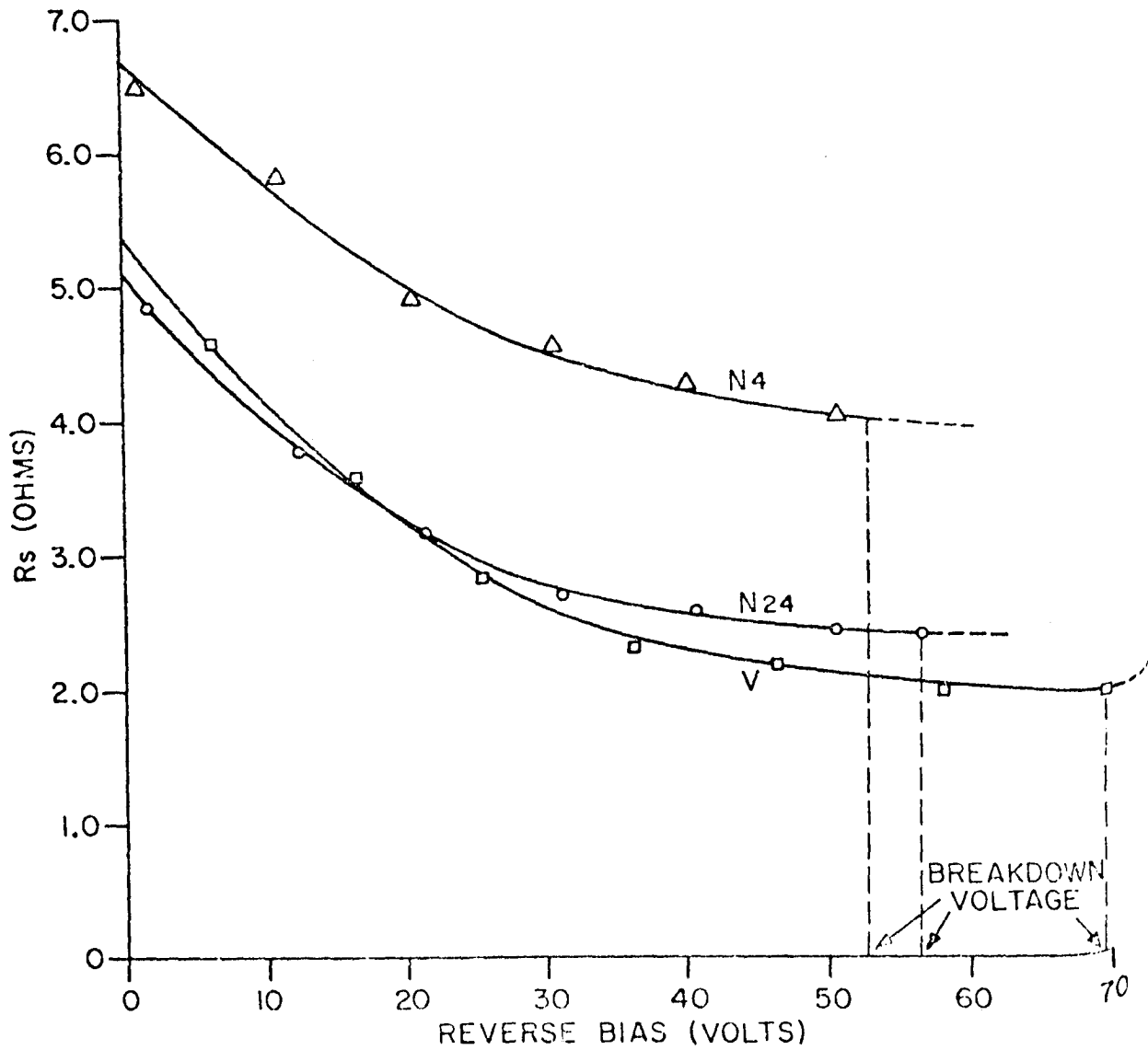
Figure 4.8. Series Resistance (R_s) Versus Reverse Bias Voltage.
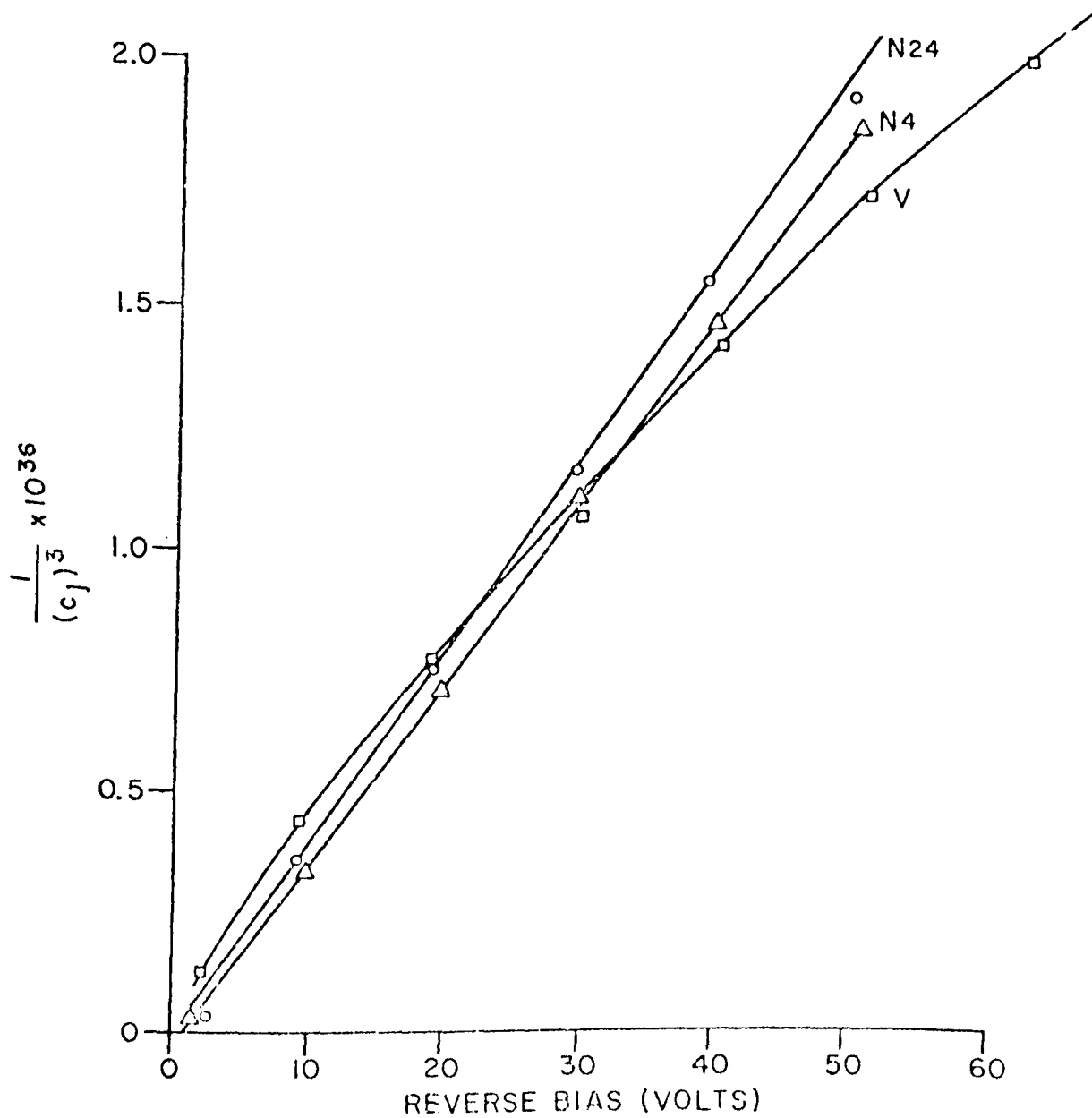
Figure 4.9. Depletion Capacitance (C_j) in (Farads)$^{-3}$ Versus Reverse Bias Voltage.
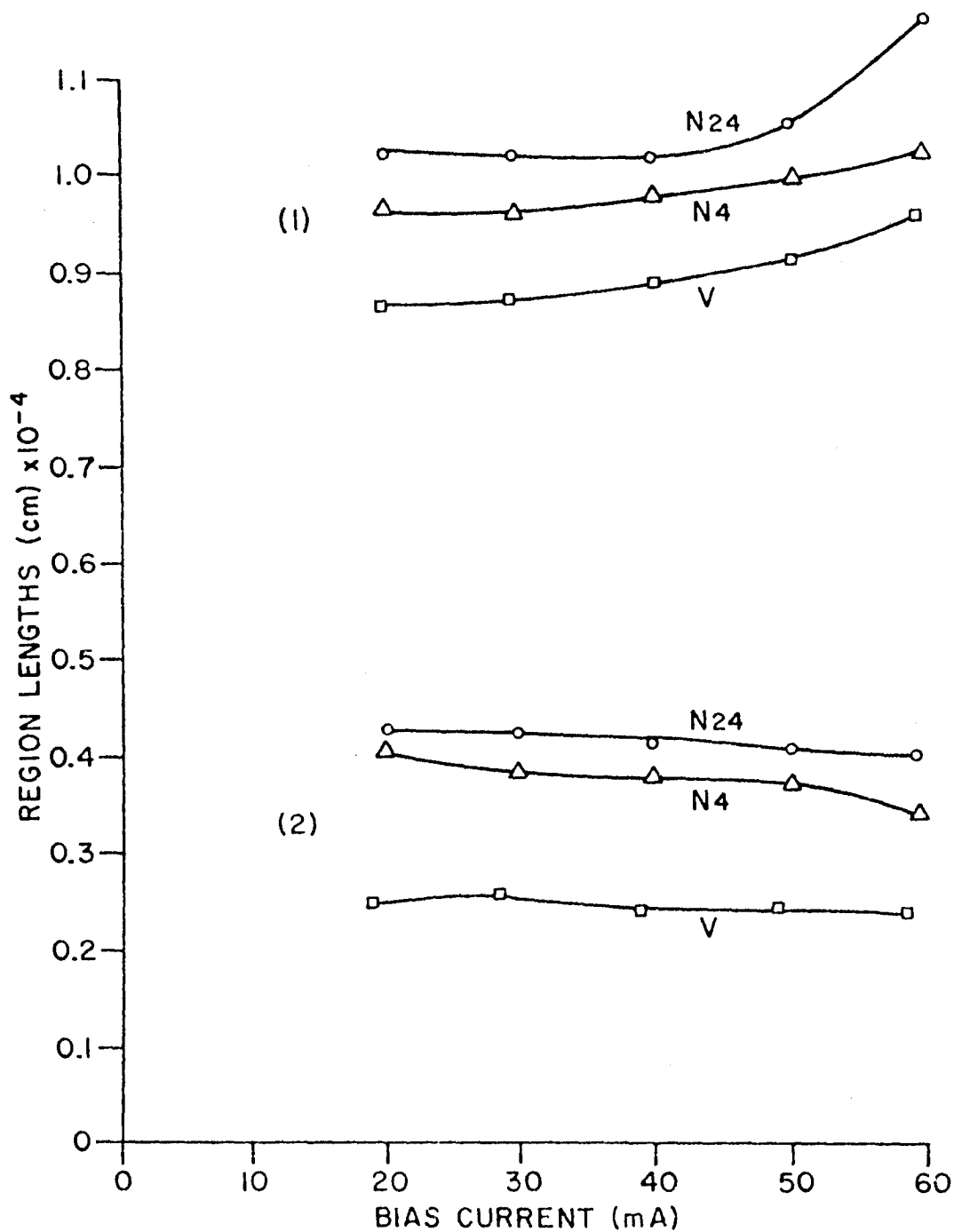
Figure 4.10. *Avalanche and Drift Region Lengths (L_A and L_D) Versus Bias Current (I_o). 1, Drift Region Lengths. 2, Avalanche Region Lengths.*
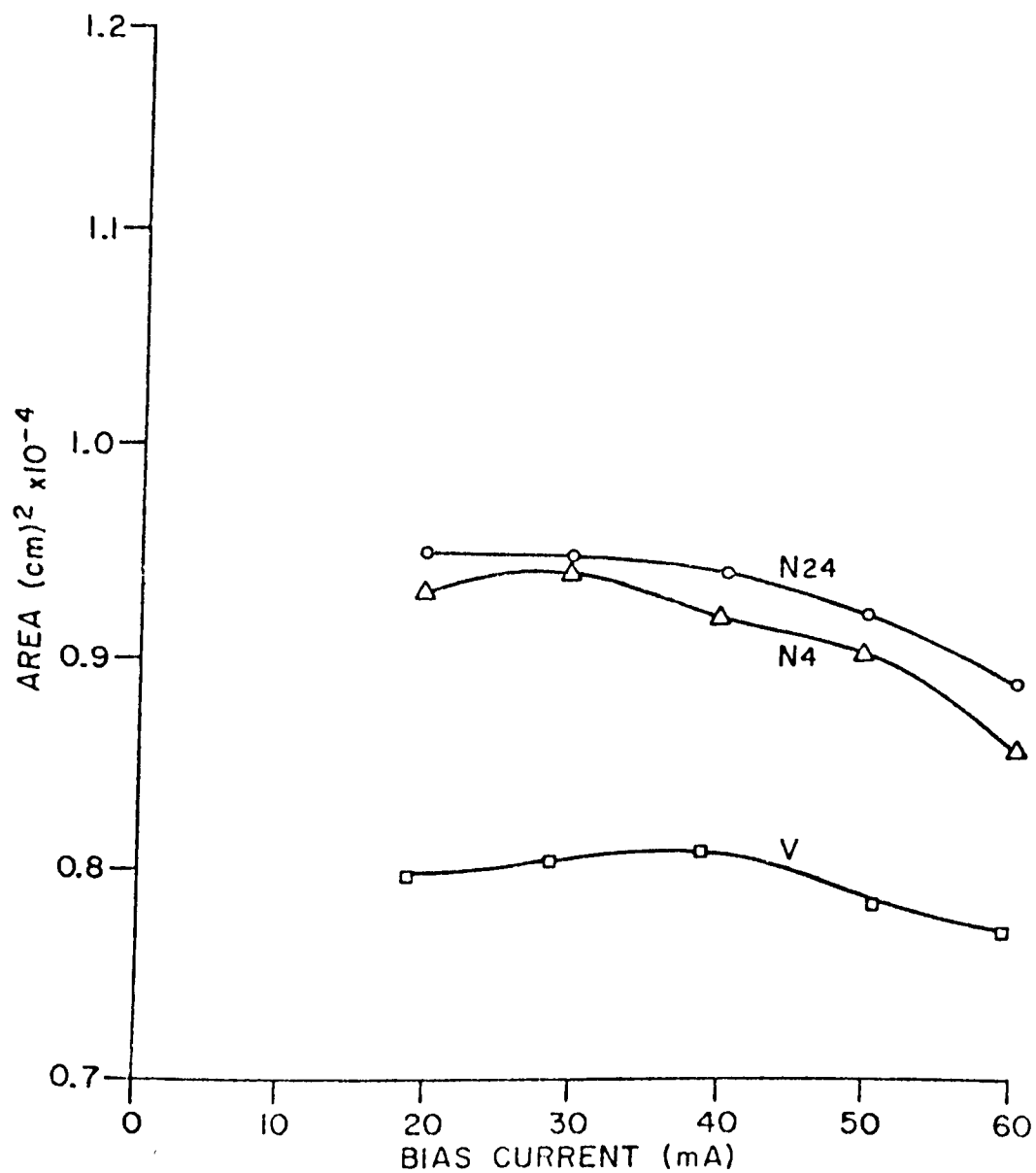
Figure 4.11.   Effective Area (A_I) of the Avalanche
Region Versus Bias Current.

44
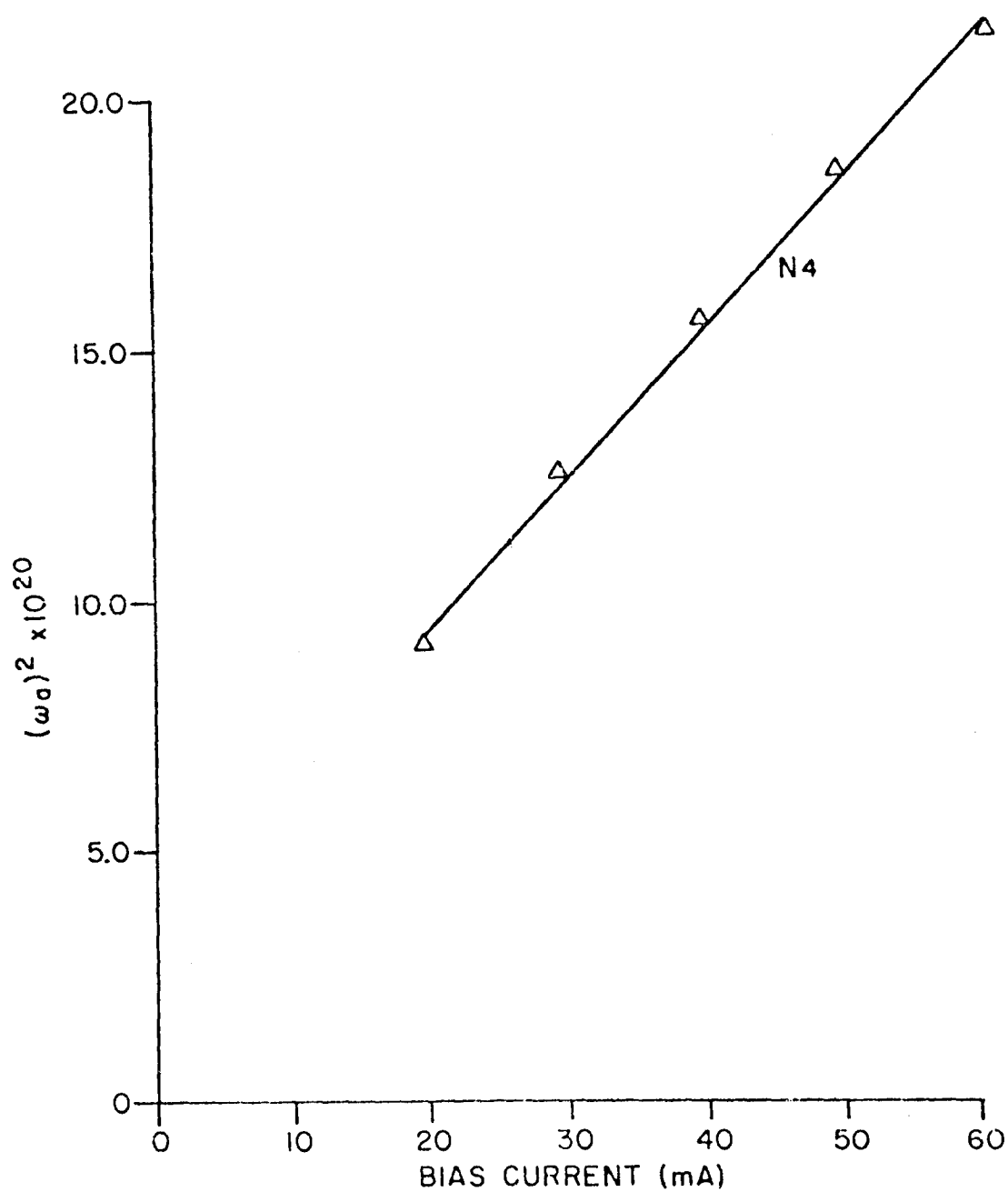
Figure 4.12. Avalanche Frequency (Radian Sec^{-1})^2 Versus Bias Current.

4.7 COMMENTS AND DISCUSSION

If 4% accuracy in the estimation of the model parameters is acceptable, the one-at-a-time parameter search methods are suitable. When greater experimental accuracy is possible, more complex models and more efficient search methods, such as Powell's method, are justified. However, note that the results obtained represented "best fit" solutions not necessarily associated with the global minimum.

The validity of the package parameter values was indicated by the close repeatability (within 2%) for several independent sets of measurements at different bias voltages.

The Northern Electric diodes exhibited different values of package inductance (L_p) because the diode N_4 had one lead wire to the chip, whereas the diode N_{24} had two lead wires.

The variation of the bulk resistance (R_s) with reverse bias agreed qualitatively with published results [17]. The value of R_s at breakdown was assumed to be invariant in avalanche and included the constant losses of the package. Separation of the package and chip losses is difficult due to the high reactance of the chip in series with R_s, masking the small loss.

The depletion capacitance variation with reverse bias voltage is plotted as $1/C^3$ in Figure 4.9. The theoretical relationship for a linearly graded junction was in close agreement with the measurements on the Northern Electric diodes and indicated that the p^+n junctions were linearly graded. The Varian diode exhibited characteristics of an abrupt junction, but this evidence was not conclusive.

The avalanche and drift region length variations with bias current below 50 mA (500 A cm^{-2}) were within 5%, which could have been caused by experimental error. However, for higher currents (>600 A cm^{-2}) the assumption of constant region lengths did not hold. From the results of Schroeder [18], the ratios of avalanche region width to the depletion width for the Northern Electric diodes indicated p^+n junctions with between 10^{15} and 10^{16} cm^{-3} background doping level. The Varian diode results indicated an n^+p junction with between 10^{16} and 10^{17} cm^{-3} background doping.

The effective area of the diode followed the same trend as for the region lengths. The effective area remained within 5% up to 550 A cm^{-2} bias current but deviated sharply above this value of bias.

In Figure 4.12 the square of the avalanche frequency is plotted against bias current. The linear relationship was in good agreement with theoretical predictions [15]. However, at high bias currents the residual error in fitting the measured to theoretical results increased, which could have indicated variation of α' or the effective area at high currents.

The chip taper is shown in Table 4.3 and was found to be a relatively insensitive parameter in the objective function. In this case, the chip taper was a second order effect on the terminal impedance.

The results indicate that the lumped model of the Read structure represents the diode accurately for low currents but above 600 A cm^{-2} the assumptions made in the model gradually become incorrect. For example, the analysis can be affected by ionization in the drift region, a significant transit time in the avalanche region and both types of carriers in the avalanche region. Also, the presence of thermal effects becomes more significant at high currents.

5. DESIGN OF MICROSTRIP IMPATT OSCILLATORS

5.1 INTRODUCTION

The synthesis of active microwave components is complicated and depends on an accurate knowledge of the parameters of the device and the circuit. In practice, however, many circuits are provided with mechanical or active tuning [1] to allow for inaccuracies in design. The complications that arise from the introduction of an external tuning element make it most desirable that an improved design procedure be developed with sufficient accuracy to avoid the need for such elements. In this chapter, the design of IMPATT diode oscillators is considered as an application of both microstrip circuit analysis and state space formulation. The IMPATT diode was characterized in a coaxial cavity and the microstrip circuit provided the impedance necessary for oscillation at the design frequency.

Simple TEM transmission line theory, which predicted the impedance of the microstrip transformer, was corrected for:

    a)   discontinuity impedances;

    b)   the OSM connector from the coaxial to the microstrip lines;

    c)   the microstrip mount for the diode.

This design method predicted the frequency of oscillation to within 3%.

A brief discussion of oscillation conditions and microstrip theory is given.

5.2 OSCILLATOR RELATIONSHIPS

In general, a negative resistance device oscillator can be represented by the circuit shown in Figure 5.1 where the impedance $Z_D(\omega)$ is the device impedance [2]. $Z_L(\omega)$ is the load impedance seen at the device terminals and the voltage source e(t) is the noise in the device and circuit which can initiate oscillation.
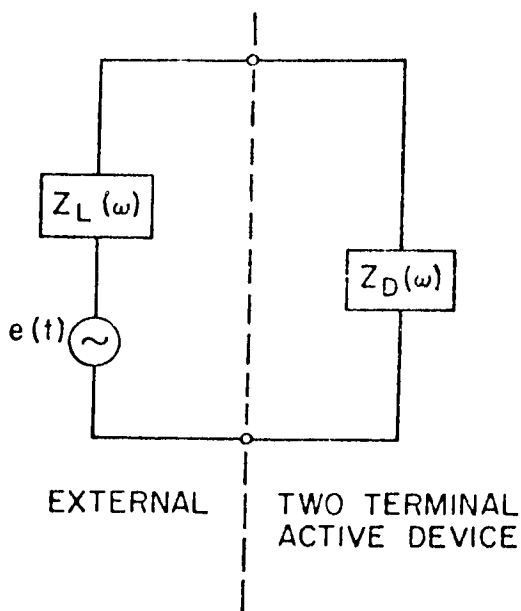
Figure 5.1. Equivalent Circuit of an Oscillator.

For example, assume that the device can be represented as a series, voltage-dependent, resistor and inductor. Thus

$$Z_D(\omega,v) = -R_D(v) + j\omega L_D(v)$$

where

ω is the operating frequency

and v is the alternating voltage.

The impedance matching circuit is given by

$$Z_L(\omega) = R_L + \frac{1}{j\omega C_L}$$

In this case, and assuming no harmonic currents, the form of the voltage (v) can be written as

$$v = Ae^{\alpha t} \cos \omega_n t$$

and

$$\omega_o^2 = \omega_n^2 + \alpha^2 \tag{5.1}$$

where, ω_o, ω_n and α are functions of v,

and ω_o is the natural frequency of the undamped system, given by

$$\omega_o = \frac{1}{(L_D(v) \; C_L)^{\frac{1}{2}}} \tag{5.2}$$

and α is a small positive real number in the case of the total resistance of the circuit being a negative real number.

For small signal oscillation, in the steady state, v is small, where

$$R_D(v) \rightarrow R_L$$

$$\alpha \rightarrow 0$$

and

$$\omega \rightarrow \omega_o. \tag{5.3}$$

5.3 MICROSTRIP TRANSMISSION LINE

Microwave propagation by microstrip transmission line became the subject of considerable investigation in the 1950's [3]. However, the high loss by radiation on the low dielectric constant substrates available at that time discouraged further use of microstrip. In the late 1960's, the demand of the aerospace industry for miniaturization of components and the availability of high-quality, low-loss dielectrics, such as alumina, revitalized theoretical and experimental investigations of microstrip [4], [5].

A single microstrip transmission line is shown in Figure 5.2 and the physical parameters of the structure are indicated. An important advantage of microstrip is the ease with which it can be fabricated, either by photo-etching or metal deposition techniques. However, the advantage of physical simplicity is offset by the disadvantages of radiation loss and interference with nearby circuits (Figure 5.3). These effects can be reduced, but not eliminated, by essentially confining the fields in the dielectric layer with the use of substrates of high dielectric constant.
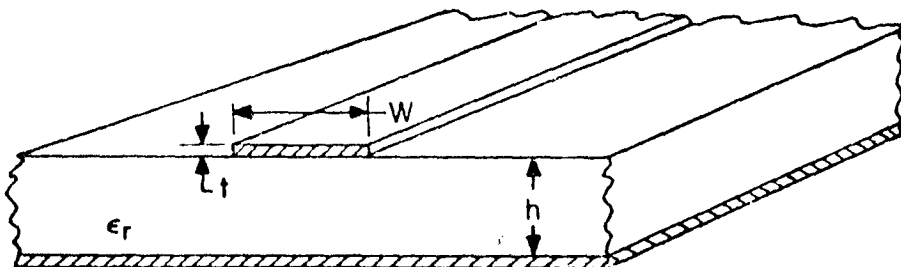
Figure 5.2. Microstrip Transmission Line.

POSSIBLE
INTERFERENCE

LINES OF ELECTRIC FIELD
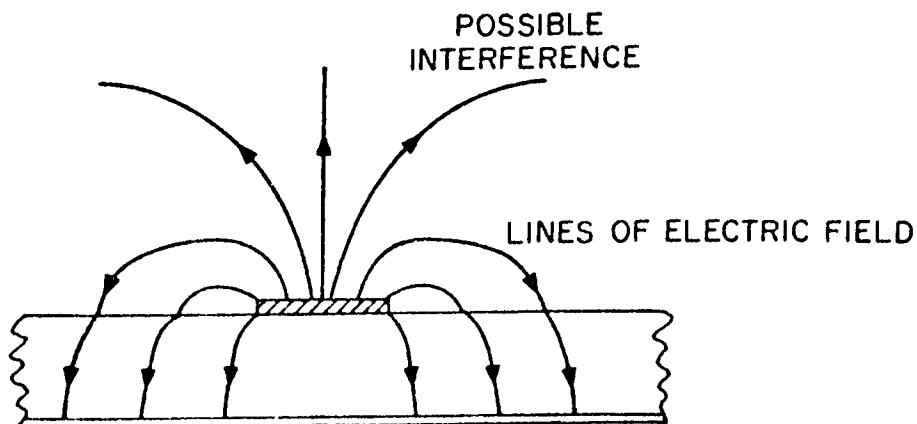
Figure 5.3. Electric Field Distribution of Microstrip

The presence of a dielectric interface does not allow the propagation of a pure TEM mode. In many practical cases, however, the actual hybrid propagating mode, which in fact has all six field components, has many of the characteristics of a TEM mode and is approximated as a "pseudo-TEM" dominant mode with the usual TEM parameters of characteristic impedance (Z_0) and propagation velocity (v). Bryant and Weiss [6] have tabulated microstrip parameters derived from the use of numerical methods and a "dielectric Green's function", which expresses the discontinuity at the dielectric interface. These results have been confirmed by Krage and Haddad [7] for the static (TEM) limit of their frequency-dependent parameters of microstrip, and it has been demonstrated that the pseudo-TEM approach remains a useful approximation at frequencies as high as X-band.

5.4 THE DESIGN APPROACH

The IMPATT diode was characterized by the method described in Chapter 4 and reported previously by the author [8]. The small-signal characterization provided the parameters of the active chip, referred to the Read diode model, and the equivalent circuit of the package. The small-signal model of the chip can give the oscillator frequency and the associated variation with bias current. The chip parameters can also be inserted into a large-signal program [9] and the output power predicted for a given microstrip transformed impedance.

The terminal impedance over X-band of a typical IMPATT diode is shown in Figure 5.4, measured at one value of bias current. In the design of an oscillator, a suitable frequency was chosen and the corresponding impedance of the IMPATT diode at that frequency is indicated as point A. From Section 5.2 the matching impedance for oscillation is shown in Figure 5.4 as point B.

In this work, successive quarter-wavelength microstrip lines were used to obtain the necessary matching impedance for the diode and the bias current was fed through an external bias tee. In a practical circuit this approach

avoids the use of coupled lines and the consequent microstrip bias circuit. Coupled lines can lead to complicated electromagnetic effects, especially at X-band frequencies and higher, due to the differing phase velocity of odd and even modes. Figure 5.5 shows a schematic diagram of the oscillator.
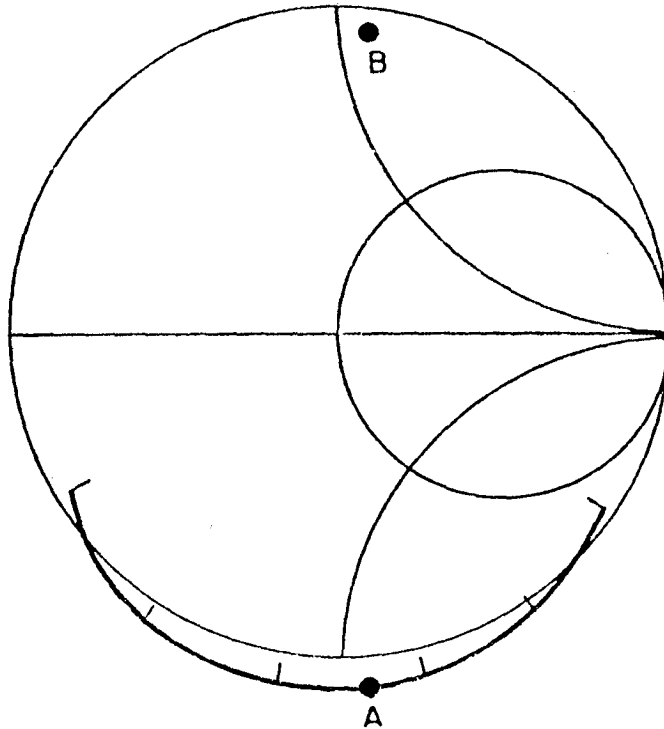
Figure 5.4. Smith Chart Representation of a Typical IMPATT Diode Terminal Impedance. A, Chosen Oscillation Point; B, Necessary Microstrip Matching Impedance (Z'").
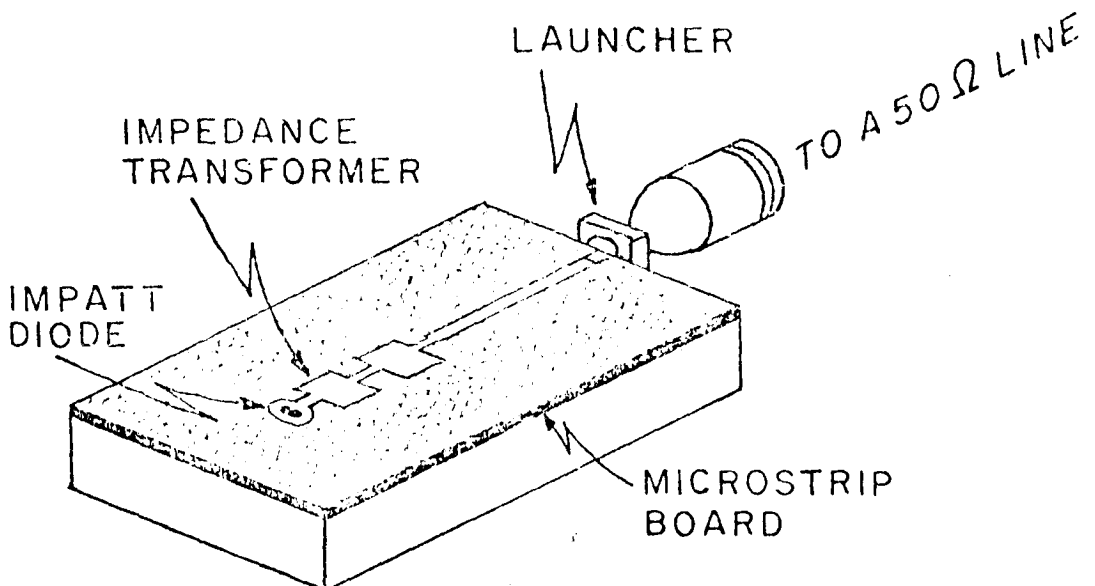
Figure 5.5. Diagram of the Microstrip Oscillator Circuit.

5.5 THE MODEL OF THE MICROSTRIP IMPEDANCE TRANSFORMER

5.5.1 The TEM Model

The equivalent circuit in TEM transmission line form is shown in Figure 5.6. The microstrip was assumed to be lossless. A transformer of five stages ($L_1,...,L_5$) was used to achieve the low value of the resistive part of the transformed impedance necessary for the circuit to oscillate. Several stages were needed as a result of the highly nonlinear relation between the microstrip line width and the characteristic impedance of the line, which limits the practical range of impedance values. The lengths of the microstrip sections were chosen so that the terminating impedance was expected to be the required impedance at point B (Figure 5.4) at the chosen frequency.
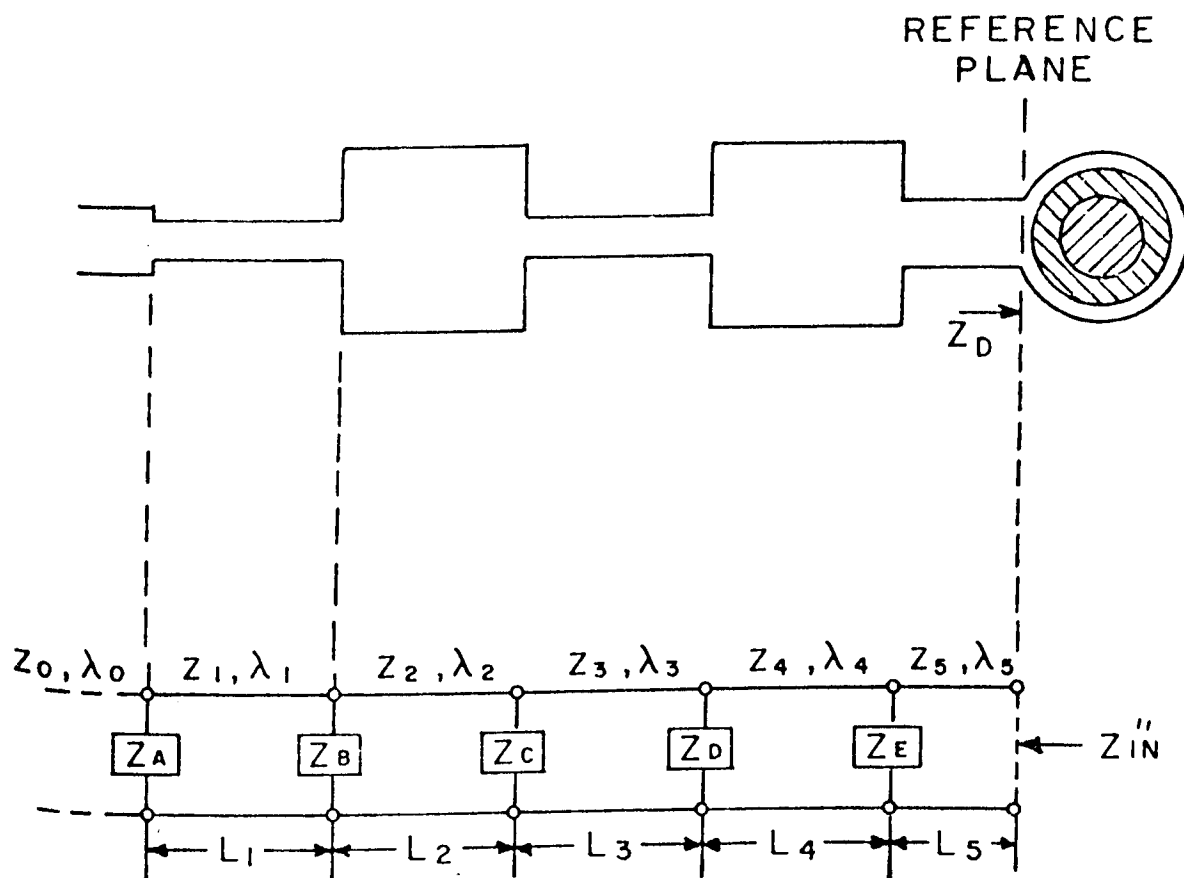
Figure 5.6. The Microstrip Impedance Transformer and Transmission Line Equivalent Circuit (Including Discontinuity Impedance)

Preliminary network analyzer measurements and oscillator tests showed that this first approximation to the microstrip model was significantly in error. The inherent assumptions were examined in detail, and found to involve three important sources of error:

    a)   Discontinuity impedance;

    b)   The coaxial to microstrip transition;

    c)   The diode mount.

5.5.2 Discontinuity Impedances

The excess charge and current distributions in the vicinity of a line discontinuity can be simply modelled as a shunt impedance. Figure 5.6 shows the insertion of discontinuity impedances, $Z_A, \ldots, Z_E$. A true analysis of the discontinuity effects has not yet been reported. However, Benedek and Silvester [10] model the microstrip discontinuities as capacitances for the static field approximation, and these values are used. A typical microstrip discontinuity and the relevant parameters are shown in Figure 5.7. For example, consider a microstrip line discontinuity with the following parameters:

$$\varepsilon_r = 9.6$$

$$h = 0.060''$$

$$W_1 = 0.064'' \text{ (50 ohm microstrip line)}$$

$$W_2 = 0.120'' \text{ (35 ohm microstrip line)}$$

From Benedek and Silvester,

$$\frac{C}{\left(W_1 W_2\right)^{\frac{1}{2}}} = 25 \text{ pF/m}$$

where

    C is the discontinuity capacitance.

Hence $C = 0.043$ pF.

Addition of the discontinuity impedances changed the apparent transformed impedance from Z''' (coincident with B) to Z'', as shown in Figure 5.8a.
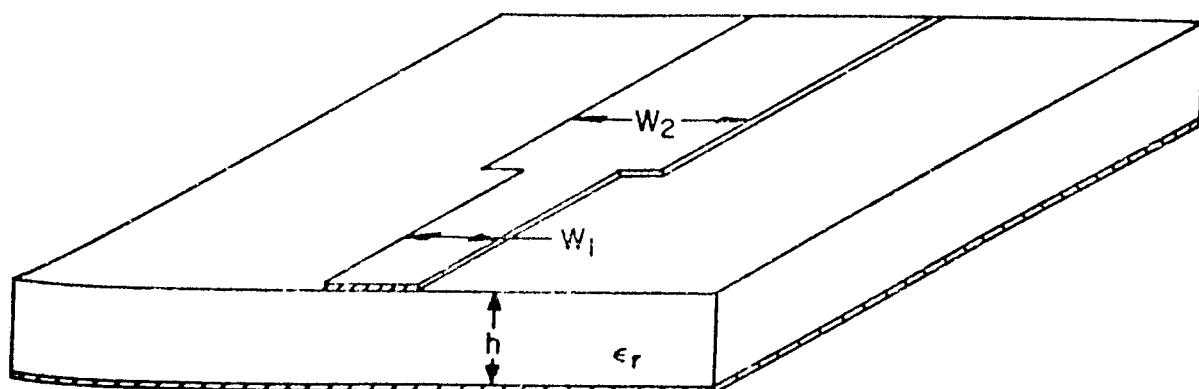
Figure 5.7. A Typical Microstrip Discontinuity.

5.5.3 The Coaxial to Microstrip Transition

Several workers [11,12] have shown that the connector from the coaxial to microstrip line is a significant discontinuity at frequencies of several GHz. The connector does not simply couple two TEM transmission lines but can be regarded as a microstrip "launcher" from which the dominant pseudo-TEM waves and some spurious radiation are initiated.

One approach to the minimization of the discontinuity effects is empirically to redesign the connector until the V.S.W.R. is below an accepted minimum value [13,14]. However, in this work, standard commercially available connectors were used and the major discontinuity was assumed to be at the transition from the coaxial to the microstrip line. The discontinuity was modelled as a shunt impedance (Z_{LR} in Figure 5.9). The value of the impedance was found by examination of the reflection coefficient from an open-circuited length of 50 ohm microstrip line over the frequency range of interest. A parameter variation technique was used to match the actual and predicted reflection coefficients according to a least squares error criterion.

A microstrip having a characteristic impedance of 50 ohms was terminated with an open circuit and the electrical length corrected for the end effect [15,16]. The parameters that were assumed to be known for the microstrip are given:

a) The electrical length from the discontinuity at the plane QQ' to the open-circuit (($\ell_1 + \Delta\ell_1$) in Figure 5.9);

b) The characteristic impedance (Z_o);

c) The propagation velocity (v_1).

The network analyzer measured the reflection coefficient at the plane PP' that resulted from the combined effects of the microstrip line, the microstrip to coaxial connector and the precision OSM to N-type connector.

Figure 5.8a. Effect of the Microstrip Corrections to the Transmission Line Model.

Figure 5.8b. Second Stage of the Iterative Design Process.
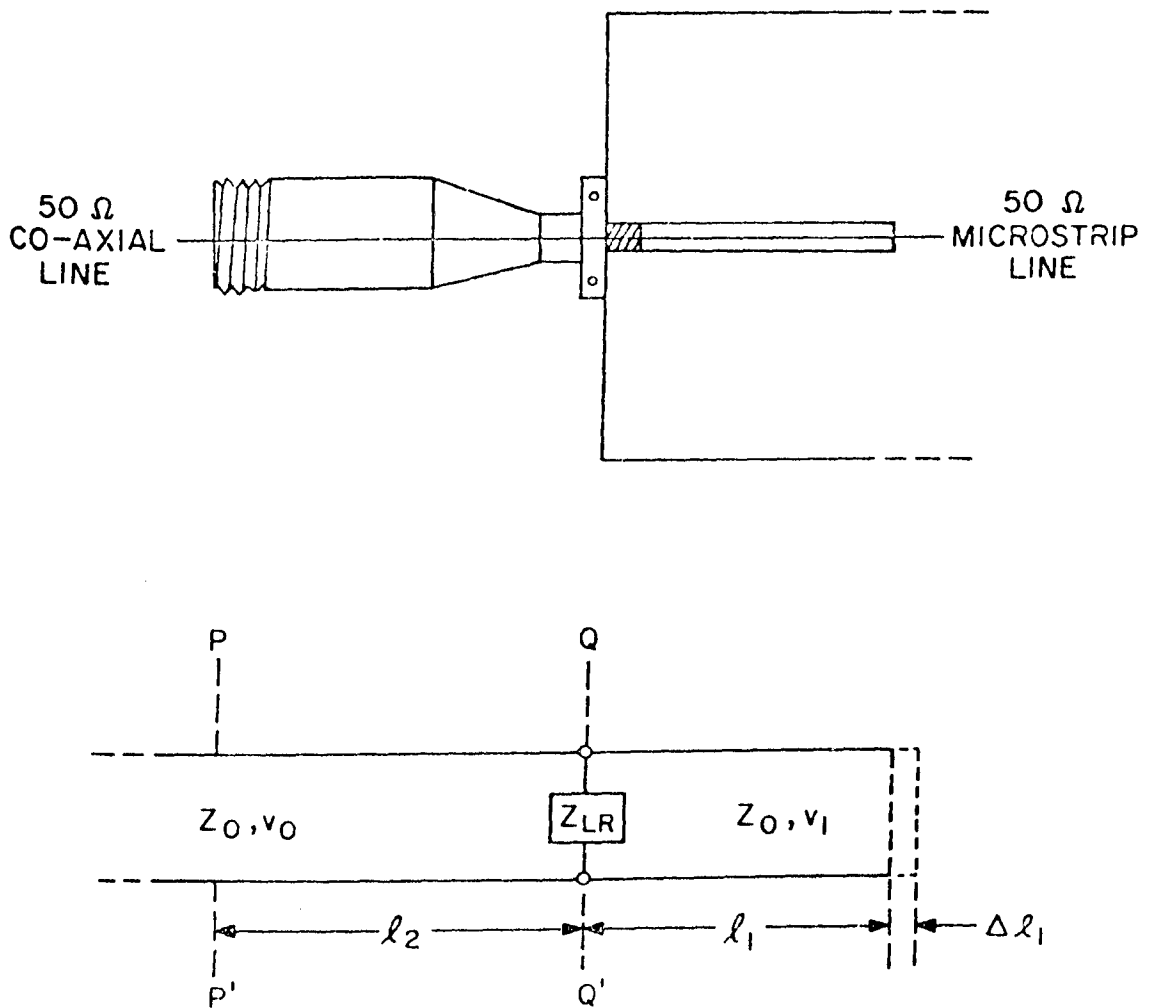
Figure 5.9. The Coaxial Line to Microstrip Transition and the Associated Equivalent Circuit. The Lumped Discontinuity Z_{LR} is at the Plane of the Transition QQ'.

The reflection coefficient can be written as a function of the following unknowns:

  i)   the discontinuity impedance (Z_{LR});

  ii) the electrical length of the OSM to N-type connector (ℓ_2).

A general shunt representation (G, L and C) is assumed for the discontinuity impedance, where

$$Z_{LR} = \frac{1}{G + j\omega C + \frac{1}{j\omega L}} \, ,$$

and ω is the operating frequency.

At the plane PP' the open-circuited length of microstrip line can be represented as an admittance Y_{oc}.

$$\text{Now} \quad Y_{oc} = j \, Y_o \tan \theta_1 \tag{5.4}$$

where

$$Y_o = \frac{1}{Z_o}$$

and

$$\theta_1 = \frac{\omega}{v_1} (\ell_1 + \Delta\ell_1) \tag{5.5}$$

The admittance at the plane QQ' is given by Y_ϕ, where

$$Y_\phi = (j [\omega C - \frac{1}{\omega L} + Y_o \tan \theta_1] + G) \tag{5.6}$$

At the plane PP', the admittance Y_p can be written as

$$Y_p = \left[\frac{Y_\phi + j \, Y_o \tan \theta_2}{Y_o + j \, Y_\phi \tan \theta_2} \right] Y_o \tag{5.7}$$

where

$$\theta_2 = \frac{\omega}{v_o} (\ell_2)$$

and v_o is the velocity of propagation.

The reflection coefficient at PP' is Γ_p, where

$$\Gamma_p = \frac{Y_o - Y_p}{Y_o + Y_p} \tag{5.8}$$

If it is assumed that the impedance Z_{LR} is capacitive, the analysis is simplified, and Y_p becomes:

$$Y_p = \left[\frac{j\left[\omega C + Y_o\left[\tan\left[\frac{\omega}{v_1}(\ell_1 + \Delta\ell_i)\right] + \tan\left[\frac{\omega\ell_2}{v_o}\right]\right]\right]}{Y_o - \left[\omega C + Y_o\tan\left[\frac{\omega}{v_1}(\ell_1 + \Delta\ell_1)\right]\right]\tan\left[\frac{\omega\ell_2}{v_o}\right]}\right] Y_o \tag{5.9}$$

Over a range of frequencies, $\Delta\omega$, the effects of the two unkowns, C and ℓ_2, on the admittance Y_p can be separated if

$$\left[\frac{\Delta\omega.\ell_2}{v_o}\right] > 1 \tag{5.10}$$

The measured reflection coefficient was matched to the predicted reflection coefficient (eqn. (5.9)) over X-band by variation of the parameters C and ℓ_2. Typically the factor $[\Delta\omega\ell_2/v_o]$ had a value of 3 which ensured a separation of the variables over the frequency range $\Delta\omega$ radians. The transformer impedance, including the corrections for the discontinuity and the connector impedances is shown in Figure 5.8a to be Z'.

5.5.4 The Diode Mount

The IMPATT diode was accurately characterized in a coaxial cavity. When the diode was mounted in microstrip the reference plane for the terminal impedance had to be known for this orientation [17]. A substitution method and the use of two reference impedances were employed to establish the reference plane.

   a) The diode was mounted in a microstrip line of characteristic impedance of 50 ohms and the reference plane was assumed initially to be at AA' (Figure 5.10).
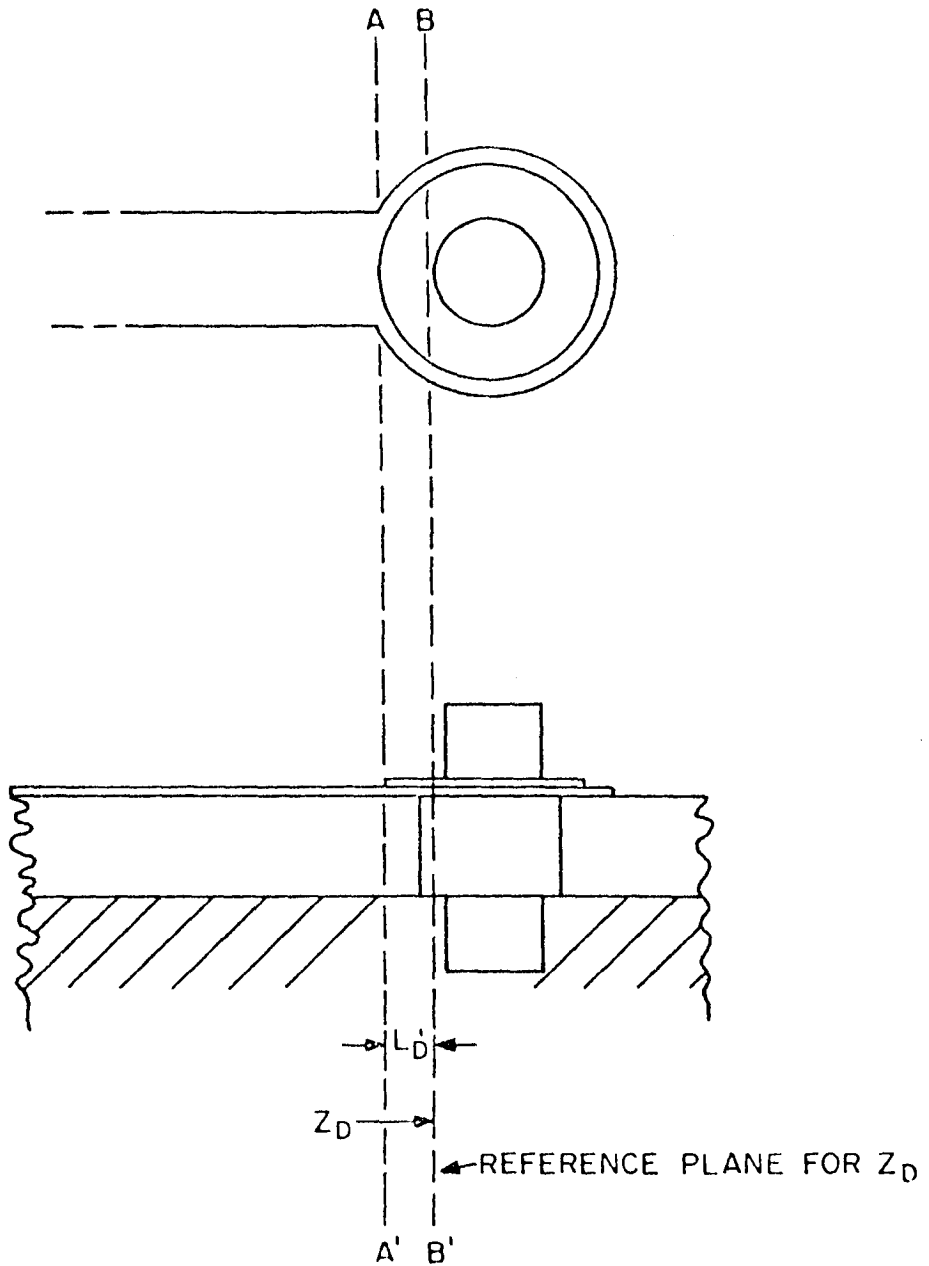
Figure 5.10. Microstrip Equivalent Reference Plane for the IMPATT Diode.
Z_D, *the Measured Impedance of the Diode in the Coaxial Test Jig.*

b) The reference plane of the network analyzer was adjusted until the diode reflection coefficient which was measured in the coaxial jig was displayed on the analyzer's Smith Chart over the X-band range of frequencies.

c) A 50 ohm microstrip line, terminated as an open circuit, was substituted for the diode line and reduced in length until an open-circuit representation, corrected for the end effect, was shown on the analyzer display.

d) The equivalent reference plane BB' for the mounted diode was given by the corrected electrical length of the open-circuited microstrip line (an addition of L_D').

e) The reference impedances in the microstrip lines (i.e., the open-circuit and the IMPATT diode impedance) were then corrected for the effect of the connector discontinuity and the steps b) to e) were repeated. However, in practice, one iteration was found to be sufficient.

The microstrip transformed impedance, including the three corrections, is shown in Figure 5.8a as Z.

5.6 THE DESIGN PROCESS

The improved prediction of the transformed impedance (Z) (Figure 5.8a) was not now that required for oscillation at the chosen frequency. The transformer was redesigned and the corrections applied in order that the final transformed impedance (Z) approached the impedance required (B). A useful guide was to change the transformer section lengths in accordance with the angle Z'".C.Z. in Figure 5.8a which then gave, for example, Z'" as shown in Figure 5.8b. This second iteration in the trial and error process led to a new, corrected, Z value which is close to point B in Figure 5.8b. In practice, two or three iterations were sufficient.

5.7 EXPERIMENTAL MICROSTRIP OSCILLATORS

5.7.1 A Design Example

A microstrip oscillator was built such that the transformer dimensions and characteristic impedances were (after three iterations in the design process) (Figure 5.11).

$$L_o = 2.381 \text{ cm} \qquad Z_o = 50.0 \text{ ohms}$$

$$L_1 = 0.384 \text{ cm} \qquad Z_1 = 83.7 \text{ ohms}$$

$$L_2 = 0.359 \text{ cm} \qquad Z_2 = 36.2 \text{ ohms}$$

$$L_3 = 0.384 \text{ cm} \qquad Z_3 = 83.7 \text{ ohms}$$

$$L_4 = 0.389 \text{ cm} \qquad Z_4 = 36.2 \text{ ohms}$$

$$L_5 = 0.091 \text{ cm} \qquad Z_5 = 50.0 \text{ ohms}$$

The nonlinear relation between the line width and characteristic impedance determines the maximum and minimum practical values of characteristic impedance. To achieve the low value of resistance required for oscillation (eqn. 5.3)) four cascaded microstrip lines were required ($L_1, \ldots, L_4$). The line L_5 inductively tuned the oscillator.

The design example is shown in Figure 5.12 and the input impedance (Z_{in}) of the transformer at the design frequency (7.71 GHz) is also shown on the Smith Chart.

The simple transmission line equations gave the first approximation to the input impedance of the transformer (Z_{in}''').

The discontinuity capacitances were calculated (Section 5.5.2) and the values are given as follows:

$$C_1 = 0.045 \text{ pF}$$

$$C_2 = 0.086 \text{ pF}$$

$$C_3 = 0.086 \text{ pF}$$

$$C_4 = 0.086 \text{ pF}$$

$$C_5 = 0.043 \text{ pF}.$$

With the discontinuity capacitances included, the transformed impedance is shown as Z_{in}''.

As described in Section 5.5.3, the curve fitting technique of parameter variation gave the discontinuity impedance at the microstrip connector as a capacitance of value C_{LR}, where

$$C_{LR} = 0.09 \text{ pF}$$

and

$$\frac{\Delta \omega \ell_2}{v_o} = 2.7 > 1.0$$

The resulting transformer impedance is shown as Z_{in}'.

The third correction, the reference plane for the diode mount, contributed an effective length L_D' to the microstrip line (L_5), such that $L_5' = L_5 + L_D'$. L_D' was measured (Section 5.5.4) to be

$$L_D' = 0.096 \text{ cm}$$

Therefore, $L_5' = 0.187$ cm. The correct input impedance of the transformer is is indicated by Z_{in} (Figure 5.12).
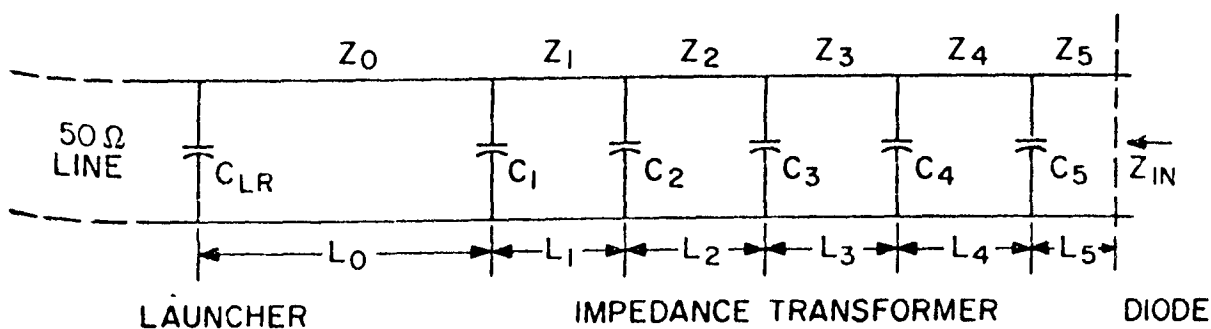
Figure 5.11. *Complete Model of the Microstrip Impedance Transformer.*
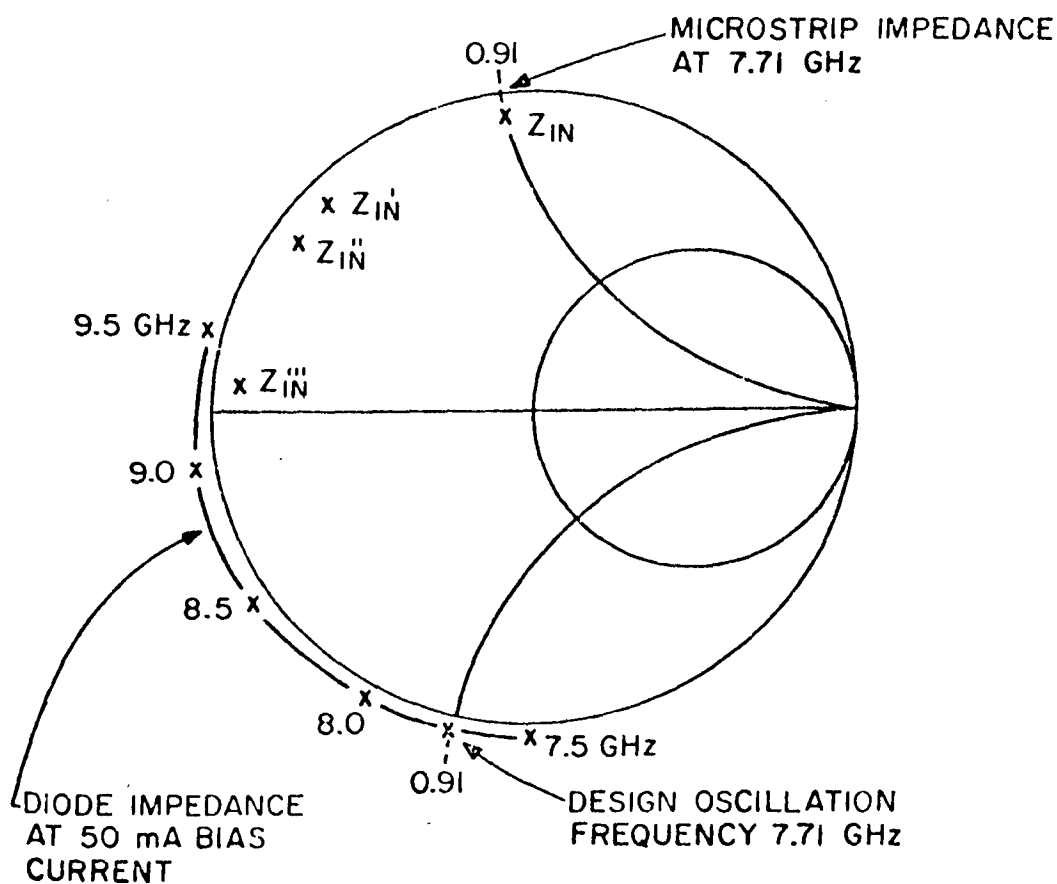
Figure 5.12. *Design Frequency of the Microstrip Oscillator Indicated on the Smith Chart.*

The IMPATT diode impedance at the design frequency and that which was measured over X-band in the coaxial test jig is also shown on the Smith Chart (Figure 5.12). The diode exhibited negative resistance over a broad frequency range and thus the same design of device could be used in many oscillator circuits.

An experimental oscillator is shown in Figure 5.13. The microstrip board was of High-K material with a thickness of 0.060" and a dielectric constant (ε_r) of 9.6. A copper holder, which gripped the base of the IMPATT diode, screwed into the aluminum block, which provided for the removal of the diode, repeatability of the measurements, and acted as a suitable heat sink.
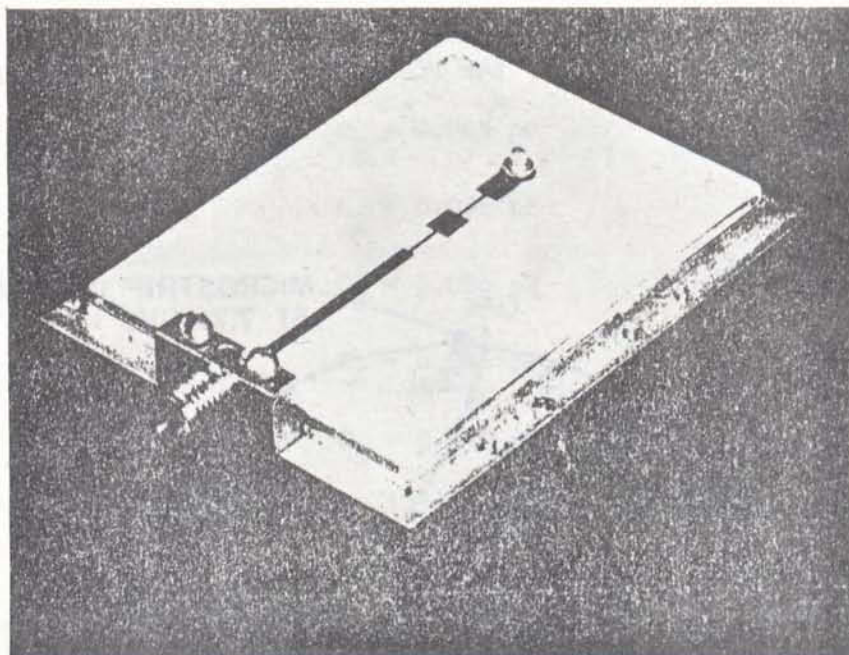
Figure 5.13.   Photograph of the Experimental X-Band Microstrip Oscillator.

5.7.2 State Space Formulation

To illustrate the use of state space techniques in the design of the oscillator, the frequency of oscillation for the example in the previous section was found from the state equation [eqn. (3.18)], with the assumption that the microstrip impedance transformer presented a simple resistive (R_M) and inductive (L_M) impedance to the IMPATT diode.

From the value of the transformer impedance (Z_{in})

$$R_M = 3.2 \text{ ohms}$$

and

$$L_M = 0.94 \text{ nH}.$$

The diode was characterized from the terminal impedance (Figure 5.12) to give the parameters of the chip and package. The state equation

$$\dot{\underline{x}} = [A]\underline{x} + [B]\underline{u}$$

included the effect of the microstrip termination, where the vector $\underline{x}$ is given as (Section 3.4)

$$\underline{x} = \begin{bmatrix} E_1 \\ E_2 \\ E_3 \\ E_4 \\ i_a \\ v_{c1} \\ i_L \\ v_{c2} \\ i_{LM} \end{bmatrix}$$

and i_{LM} is the current in the termination L_M. The eigenvalues of the 9x9 matrix $[A]$ are as follows ($\times 10^9$ rad sec^{-1})

$$2.91 + j48.44$$
$$2.91 - j48.44$$
$$-83.81$$
$$-12.09 + j37.91$$
$$-12.09 - j37.91$$
$$-26.26 + j76.37$$
$$-26.26 - j76.37$$
$$-50.52 + j21.19$$
$$-50.52 - j21.19$$

which gave the oscillation frequency as 7.71 GHz.

Note that the simple representation of the microstrip circuit is not accurate over a range of frequencies and an improved equivalent circuit would be required for further studies. However, if each section of microstrip transmission line is represented as an equivalent circuit of, say, five lumped elements (inductances and capacitances) the matrix [A] of the state equation would become a 38 x 38 element matrix. This size of matrix significantly increases the computation time for solution of the state equation.

5.7.3 Results

The experimental microstrip oscillator described in the previous section oscillated at 7.60 GHz at an output power of 9.1 mW. The output spectrum is shown in Figure 5.14. Note that the oscillator line width was approximately 700 kHz, indicating a low-Q circuit, and that the noise components close to the carrier were only 20 dB below the carrier, which is characteristic of the high noise levels encountered in IMPATT circuits.

Three 10 mW oscillators were built and the following table summarizes their performance.

TABLE 5.1

Experimental Microstrip Oscillator Results

	i	ii	iii
Design oscillation frequency	7.71 GHz	8.50 GHz	8.02 GHz
Measured oscillation frequency	7.60 GHz	8.25 GHz	7.85 GHz
Percentage difference	1.5%	2.9%	1.9%
Output power	9.1 mW	7.2 mW	8.9 mW

5.8 CONCLUSIONS

Microstrip oscillators can be designed to within 3% of the actual operating frequencies in X-band, which would eliminate the need for external tuning elements in many practical applications. Several microstrip effects have been investigated in the oscillator analysis. In order of importance, these are:

a) the effect of the diode reference plane is dependent on the electrical dimensions of the diode and is significant at X-band and higher frequencies, while a similar package at L-band would have negligible effect;
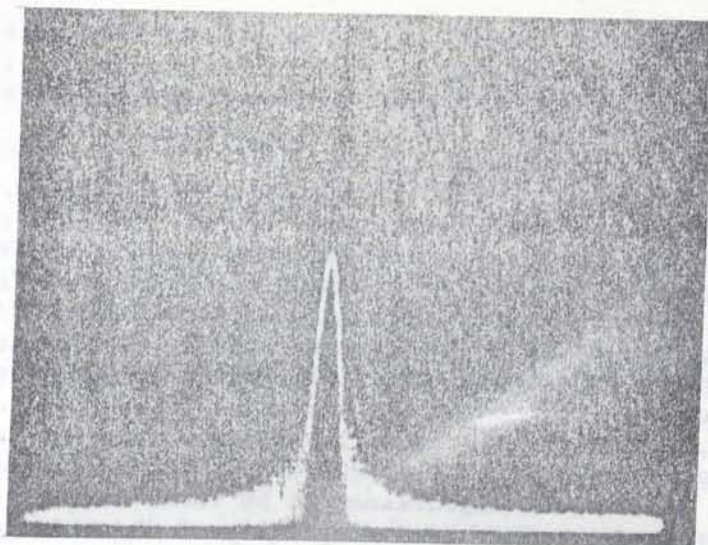
I.F. Bandwidth = 100 kHz

f_o = 7.60 GHz; Horiz. scale is 0.5 MHz/div., Vert. scale is 10 dB/div.
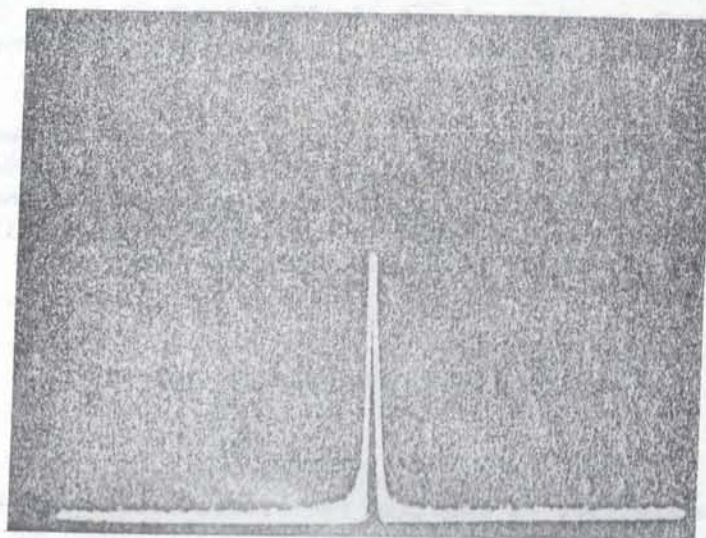
I.F. Bandwidth = 100 kHz

f_o = 7.60 GHz; Horiz. scale is 5.0 MHz/div., Vert. scale is 10 dB/div.

Figure 5.14. *Photograph of the Microstrip Oscillator Output Spectrum.*

b) the discontinuity impedances are calculated from consideration of the excess charge density at the discontinuities in line width, but further research is required to estimate the effects of excess current density in the transformer sections;

c) although the effect of the connector in this case was found to be the least of the three corrections listed, the effect is dependent on the electrical length from the connector to the first section of the transformer and can be minimized at a given frequency.

In practice, the oscillator might require slight frequency tuning to align a communications system experimentally, which can be provided by a change in bias current. To predict the variation of oscillation frequency with bias current, a model of the diode is required that can be matched to the microstrip impedance at various frequencies. State space formulation of the entire system enables the eigenvalues to be found directly which gives the oscillation frequency. The added complexity of the state space representation of transmission lines, however, seriously offsets this advantage.

Theoretically, if the diode is matched at all frequencies for oscillation, the frequency will increase as the square root of the bias current. Alternatively, Evans [18] has shown that there is practically no frequency tuning possible for a high-Q circuit. The oscillators that were built have a tuning range of approximately a hundred MHz, due to the medium-to-low-Q characteristic of the microstrip cavity. This characteristic can be seen from the output spectrum of the oscillator in which the line width is almost one MHz and can be deduced from the inherently lossy nature of microstrip.

The small-signal analysis does not give a prediction of the power output, locking bandwidth or other nonlinear effects. This would require a large-signal model of the diode and an improved estimation of the circuit losses. At high power levels the model of the diode would require improvement due to the nonlinear nature of oscillation [9].

6. A REFLECTION TYPE IMPATT DIODE AMPLIFIER

6.1 INTRODUCTION

Several investigations of negative resistance device amplifiers have been made, both in the 'stable' [1] and 'locked oscillator' [2] modes. Design accuracy of reflection type amplifiers with IMPATT diodes is examined in this chapter. The amplifier operated in a stable, small-signal mode suitable for such applications as communication links [3], or microwave measurements [4]. The coaxial transformer and the transition space between the coaxial line and the diode were analyzed and the small-signal gain and phase shift predicted. In order of importance, the corrections to the transmission line equations were:

1) Radial transmission line at the junction with the diode;

2) Transition equivalent circuit at the coaxial/radial line junction;

3) Discontinuity impedances of the transmission line transformer.

The lumped model for the IMPATT diode, described in Chapter 3, was used to predict the amplifier gain and phase shift with bias current.

The noise figure of the IMPATT amplifier was measured and compared to small-signal noise theories [5],[6] for the parameters of the IMPATT diode found from the characterization method (Chapter 4). The typical noise figure of 30-45 dB limits the applications of the IMPATT amplifier and suggests the use of noise reduction techniques such as injection locking [7].

6.2 IMPEDANCE MATCHING NETWORKS

The experimental testing of devices often employs adjustable microwave cavities so that the same test-jigs can be used to study devices over several frequency ranges. When a device is incorporated into a microwave system, however, the amplifier cavity is fixed and the frequency range therefore is specified.

The cavity design that is considered in this chapter avoids any effects associated with variable tuning-slugs and adjusting-slots, and provides a broadband match at one impedance value, if required.

Low values of characteristic impedance (less than 10 Ω) are achieved with ease in coaxial transmission line and thus stepped impedance transformers are feasible for broadband use in IMPATT diode circuits [8,9].

Consider a length of uniform transmission line, one quarter of a wavelength in length at the chosen centre frequency, with a characteristic impedance Z_1 and terminated in a load Z_L.

From the transmission line equations

$$Z_{in} = \frac{Z_1^2}{Z_L} \tag{6.1}$$

where Z_{in} is the input impedance to the transformer.

If Z_1 is chosen such that

$$Z_1 = (Z_o Z_L)^{\frac{1}{2}} \tag{6.2}$$

where Z_o is the characteristic impedance of the connected system, then a match exists at that frequency. A multi-stage transformer is shown in Figure 6.1. In this case several quarter-wave sections are interposed between the line of characteristic impedance Z_o and the load Z_1.
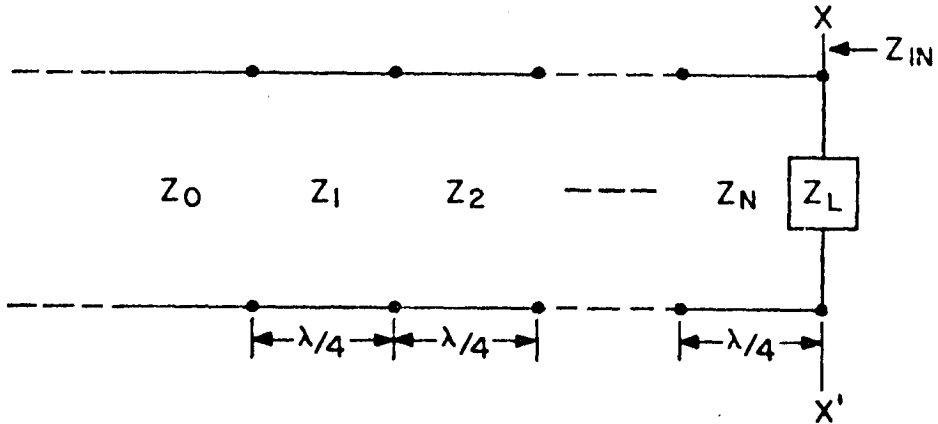
Figure 6.1. Multi-Stage Transformer, Z_i, Characteristic Impedance;
λ, Wavelength in Free Space XX', Transformer Reference Plane;
Z_{in}, Input Impedance.

For the example of a maximally flat pass-band characteristic, and considering only first-order reflections of the TEM wave at each junction, we have a "binominal" transformer [10], where

$$\ell n \; \frac{Z_{n+1}}{Z_n} = 2^{-N} \; C_n^N \; \ell n \; \frac{Z_L}{Z_o} \tag{6.3}$$

$$C_n^N = \frac{N!}{(N-n)! \, n!}$$

and N is the number of quarter-wave sections. The expression (6.3) is derived with the assumption that second-order reflections of the TEM wave are negligible and small reflections only are considered at each junction. Also, higher order coaxial modes with axial field components can be produced at each junction, but in most practical cases the modes are evanescent and are not considered at this point. The assumption of small reflections at a practical number of junctions imposes a constraint on the value of load impedances to be matched. Thus, expression (6.3) is applicable in the range

$$0.5 \; Z_o < Z_L < 2 \; Z_o \tag{6.4}$$

To further increase the bandwidth of the transformer, the magnitude of the reflection coefficient is allowed to vary as a Tchebyscheff polynominal [10], below a chosen maximum value, over the passband of the transformer. A comparison of transformer bandwidths is shown in Figure 6.2 for the quarter-wave, binominal and the Tchebyscheff transformers.
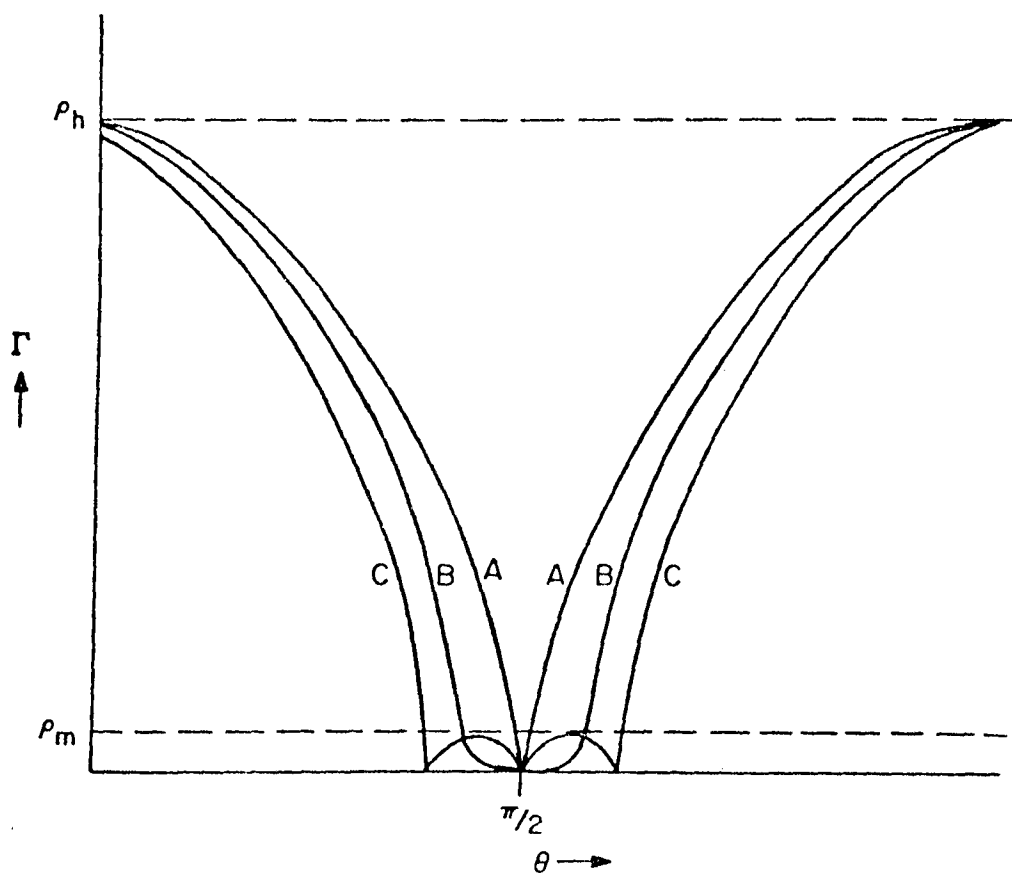
A, quarter-wave;

B, binomial;

C, Tchebyscheff.

Γ, reflection coefficient;

θ, electrical length of each section;

$$P_h = (Z_L - Z_o)/(Z_L + Z_o)$$

P_m, maximum allowable reflection coefficient over the passband.

Figure 6.2. Comparison of Transformer Bandwidths.

For example, if the specifications are given as

$$\rho_m = 0.05,$$

$$Z_L = 2\ Z_o,$$

and   N = 3,

where ρ_m is the maximum allowable reflection coefficient over the passband, the fractional bandwidths can be calculated and are given as follows:

TRANSFORMER	FRACTIONAL BANDWIDTH
Quarter-wave	0.22
Binominal	1.20
Tchebyscheff	1.65

6.3 AMPLIFIER ANALYSIS

A reflection-type amplifier is shown in Figure 6.3. The four-port circulator, matched at the fourth port, effectively separates the input and output signals. The diode cavity and matching network are designed to match the 50 ohm characteristic impedance of the system to the diode and to provide useful power gain.

An equivalent circuit of the transformer and the IMPATT diode is shown in Figure 6.4. The diode is represented by an impedance $Z_D(\omega)$ and the input impedance of the matching network as seen by the diode is represented by an impedance $Z_T(\omega)$,

$$Z_T(\omega) = R_T(\omega) + j\omega L(\omega) + \frac{1}{j\omega C(\omega)} \tag{6.5}$$

The reflection coefficient $\Gamma(\omega)$ at the diode reference plane YY' is given by the expression

$$\Gamma(\omega) = \frac{Z_D(\omega) + j\omega L(\omega) + \frac{1}{j\omega C(\omega)} - R_T(\omega)}{Z_D(\omega) + j\omega L(\omega) + \frac{1}{j\omega C(\omega)} + R_T(\omega)} \tag{6.6}$$

$$= \frac{Z_D(\omega) - Z_T^*(\omega)}{Z_D(\omega) + Z_T(\omega)}$$

OUTPUT

CO-AXIAL IMPEDANCE
TRANSFORMER

50 Ω
TERMINATION

4 PORT
CIRCULATOR

BIAS

IMPATT DIODE CAVITY
AND HEAT SINK

INPUT
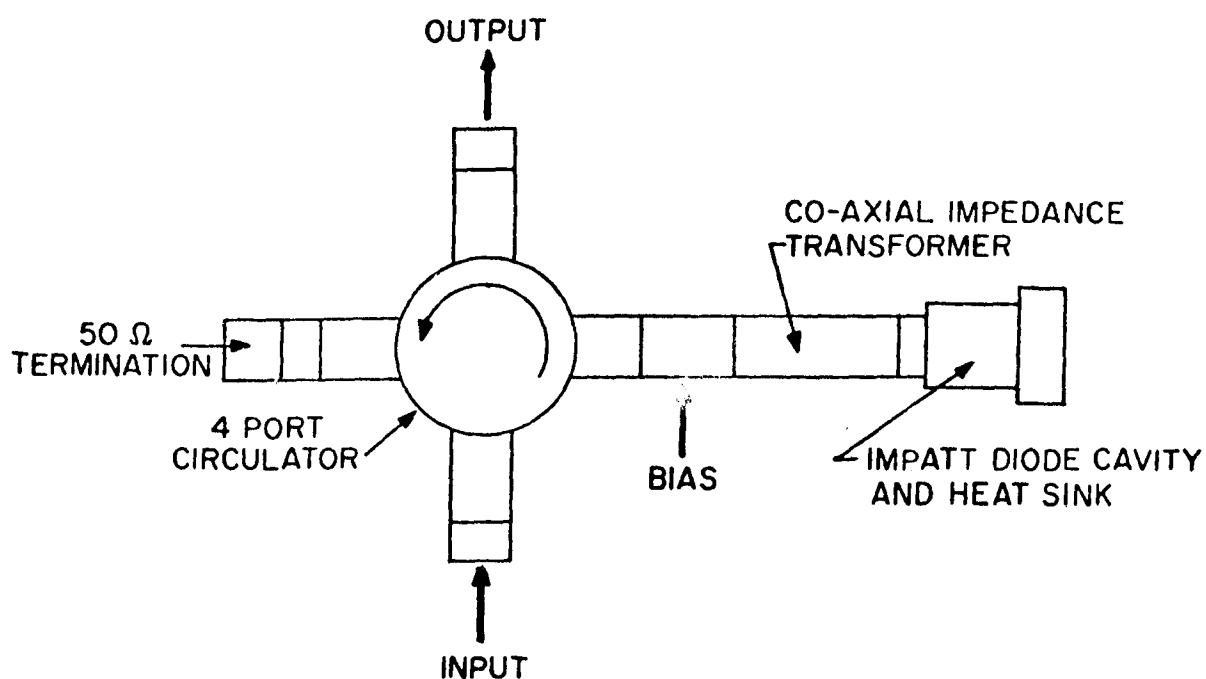
Figure 6.3. Reflection-Type IMPATT Amplifier

OUTPUT

IDEAL
CIRCULATOR

Y

$L(\omega)$

$C(\omega)$

$R_T(\omega)$

$Z_D(\omega)$

Y'

INPUT
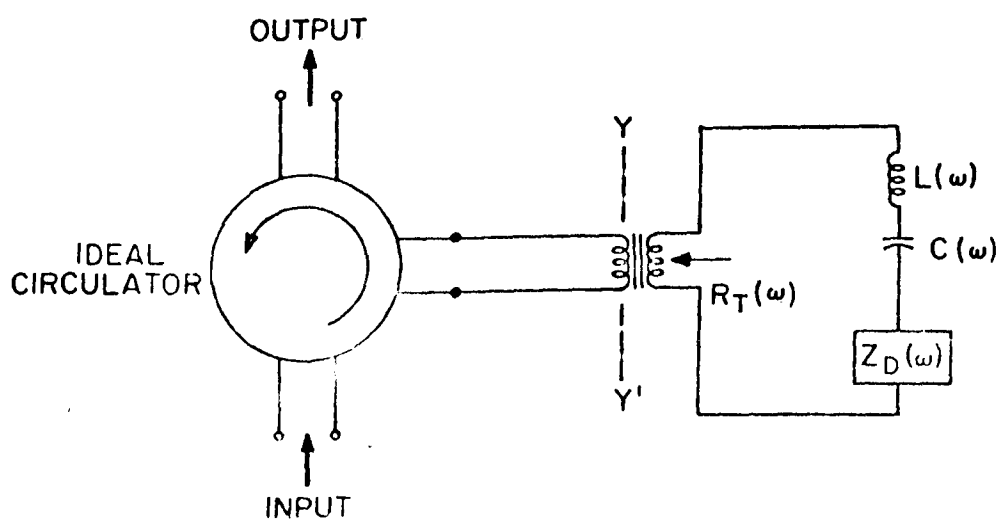
Figure 6.4. Equivalent Circuit of the IMPATT Amplifier

where $Z_T^*(\omega)$ is the conjugate of $Z_T(\omega)$

$\left|\Gamma(\omega)\right|$ is the signal gain,

$\underline{\left|\Gamma(\omega)\right.}$ is the phase of the amplifier response,

$\left|\Gamma(\omega)\right|^2$ is the power gain.

The gain is a maximum at a frequency ω_1, where ω_1 is given by

$$\mathrm{Im}[Z_T(\omega_1)] = -\,\mathrm{Im}[Z_D(\omega_1)] \tag{6.7}$$

Also, the gain is greater than unity for the condition

$$\mathrm{Re}[Z_D(\omega)] < 0 \tag{6.8}$$

Variation of the amplifier gain and phase shift is predicted from a small-signal model of the IMPATT diode. One set of measurements of terminal impedance $Z_D(\omega)$ over the frequency range of interest enables the small signal parameters of the lumped model to be estimated [Chapter 3] and a prediction made of the terminal impedance, amplifier gain and phase shift, with variation of bias current.

6.4 A PRACTICAL EXAMPLE OF AN X-BAND AMPLIFIER

6.4.1 Overall Approach

The bandwidth of an amplifier is an important parameter which distinguishes the design of a matching circuit for the amplifier from that for an oscillator. A single-stage transformer can be used in coaxial line to achieve the impedance match required for an IMPATT diode oscillator, but a similar approach for an amplifier can lead to the limitation of the amplifier bandwidth by the matching circuit and not by the device. This effect may be required in a particular application, but generally a wide bandwidth is desirable.

The terminal impedance of a typical IMPATT diode was measured in a coaxial test jig and is shown in Figure 6.5, as displayed by a network analyzer. Seemingly, the frequency dependence of the terminal impedance is similar to that of a series RLC circuit. The diode exhibits significant negative resistance over the range of 7-11 GHz and useful amplifier gain would be obtained if the diode could be matched (eqn. (6.7)) over the entire range. This match requires negative inductances and capacitances over this range, however, and cannot be realized by coaxial transmission lines connected in series.
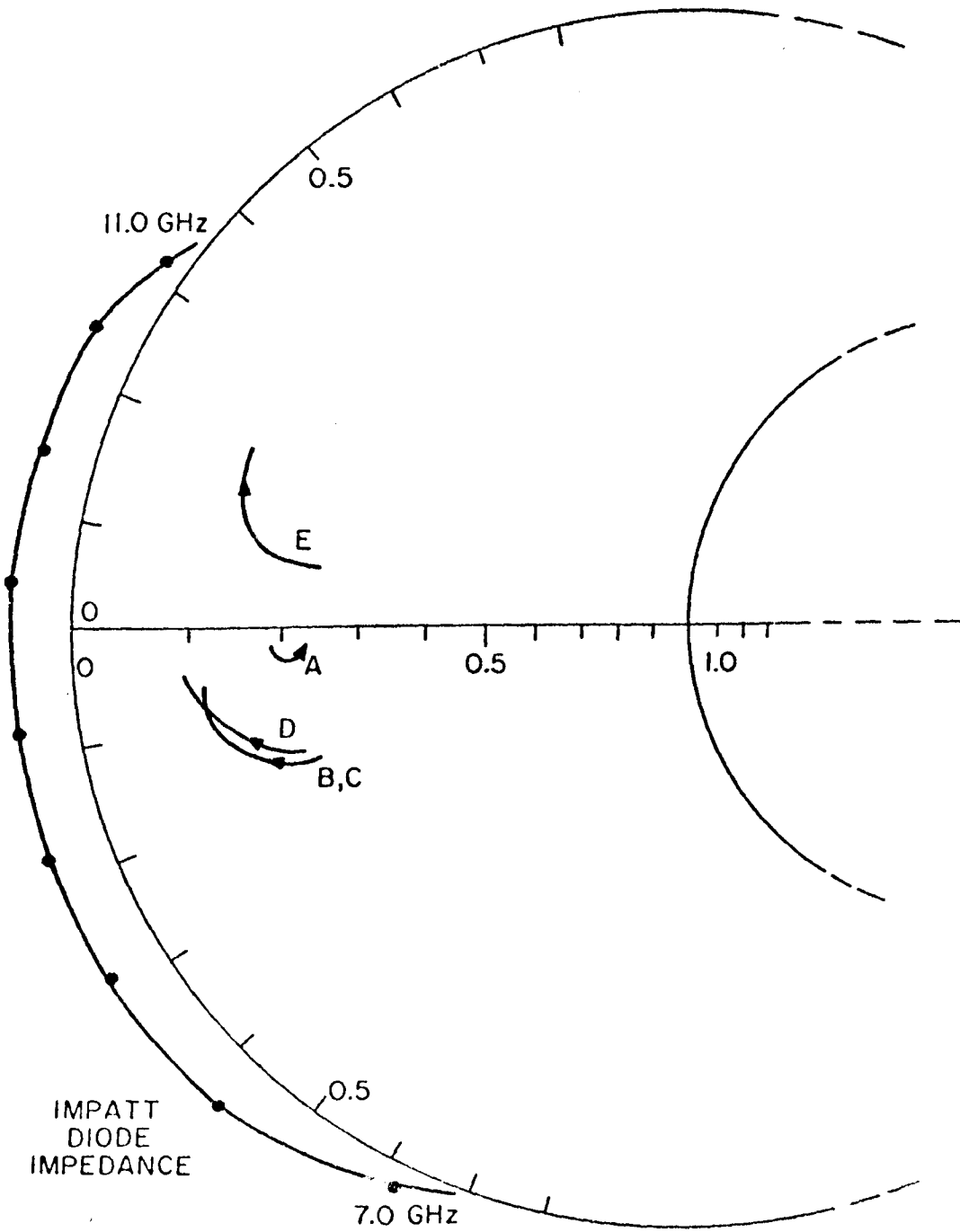
Figure 6.5. IMPATT Diode and Coaxial Transformer Input Impedances. Direction of Arrow Indicates Increasing Frequency, 7-II GHz.

A practical approach to the problem of amplifier design was to present a constant impedance at the plane of the diode over the frequency range of interest, which was achieved by a Tchebyscheff design of the transformer. Several X-band amplifiers were constructed and a typical experiment is described.

The IMPATT diode, whose terminal impedance is shown in Figure 6.5, was incorporated into an X-band amplifier and the criteria for the impedance matching network was taken as follows:

- Centre frequency f_o = 9.5 GHz

- Impedance ratio $(Z_0/Re[Z_T])$ (for a power gain of 10 dB at the centre frequency) = 5

- Fractional bandwidth $\Delta f/f_o$ = (6.5 - 12.0)/9.5 = 0.6

- VSWR (Max) over the passband $\leq$ 1.05

The matching network was designed from tables of Tchebyscheff polynominals [9] and a three-section transmission line model gave characteristic impedance values as follows:

$$Z_1 = 37.9 \text{ ohms};$$

$$Z_2 = 20.5 \text{ ohms};$$

$$Z_3 = 12.5 \text{ ohms}.$$

The calculated impedance over the range 7-11 GHz is shown in Figure 6.5 as Curve A. The design was modified to increase the impedance ratio (for an amplifier gain of 12 dB) and to provide a greater capacitive reactance to the diode (for a centre frequency of 9.9 GHz). The modification was implemented by an increase in the value of Z_2 to 30.5 ohms (Figure 6.6), and the resulting impedance at the plane XX' is shown in Figure 6.5 as curve B. The mechanical dimensions of a cross-section of the transformer in the z-plane are shown in Figure 6.6.

6.4.2 Discontinuity Impedances

In general, each discontinuity of the inner conductor of the coaxial transformer gives rise to an infinite set of discrete evanescent modes. The energy stored in these modes can be represented in an equivalent circuit by capacitances at each junction. The transmission line equations for the terminal impedance of a coaxial line are commonly corrected for the effects of these capacitances. Marcuvitz [11] presents values of the discontinuity capacitances with the parameters of wavelength and dimensions of the junction, and this approach was used in this section.
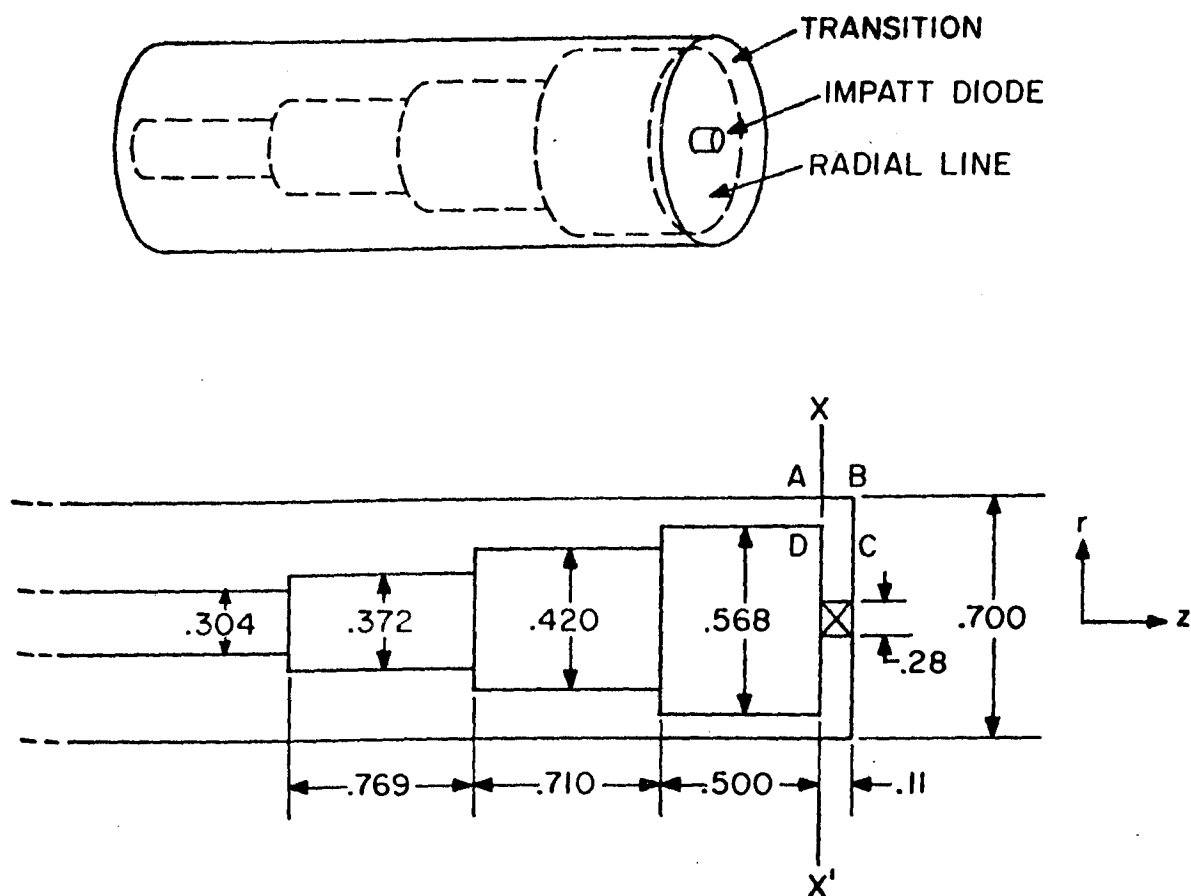
Figure 6.6. The Coaxial Impedance Transformer. (Dimensions in cm).

The values of capacitance for the three junctions of the coaxial transformer shown in Figure 6.6 were calculated to be

$$C_1 = 0.007 \text{ pF},$$

$$C_2 = 0.008 \text{ pF},$$

$$C_3 = 0.043 \text{ pF}.$$

The negligible frequency dependence of the values of capacitance can be seen from the equation for a typical junction (C_1)

$$C_1 = 5.1 \times 10^{-4} \ [11.1 + 2.0 + 0.34/\lambda^2] \text{ pF} \tag{6.9}$$

where λ is the wavelength in the coaxial line. To change the value of C_1 by 5%

$$\lambda < 0.71 \text{ cm}$$

and the frequency of operation must be greater than 42 GHz, at which frequency the validity of the model is questionable.

Insertion of the discontinuity capacitances had negligible effect on the tranformed impedance, which is shown on the Smith Chart (Figure 6.5) as curve C, coincident with curve B. This result is predictable as the design of a multi-stage transformer for wide bandwidths approaches a tapered line which has no discrete junction discontinuities.

6.4.3 Transition Between the Radial and Coaxial Lines

The magnetic fields in the toroidal - shaped transition between the radial and coaxial lines are in the form of concentric circles about the z-axis (Figure 6.6). This form is similar to the magnetic fields in both the coaxial and radial lines and was represented by an equivalent coaxial inductance (L_T), where

$$L_T = \frac{\mu_o}{2\pi} \ln \left| \frac{r_2}{r_1} \right| \text{ H m}^{-1}$$

μ_o is the permeability of free space,

r_2 is the outer radius of the transition cavity,

and r_1 is the inner radius of the transition cavity.

For the dimensions shown in Figure 6.6, the transition inductance was calculated to be

$$L_T = 0.085 \text{ nH}$$

The electric field in the radial line is parallel to the z-axis (Figure 6.6) and in the coaxial line is perpendicular to the z-axis. The transition between these conditions was represented by an equivalent capacitance (C_T) whose value was found as described below.

The area ABCD (Figure 6.7) was divided into a 30 x 20 point matrix and the potential at each point calculated from the solution of Laplace's equation, by a relaxation method [12]. The capacitance per unit length (C_p) in the x-direction was calculated from the relation

$$C_p = \frac{Q_R}{V_R} \tag{6.10}$$

where Q_R is the charge per unit length in the x-direction

and V_R is the potential between the conductors.
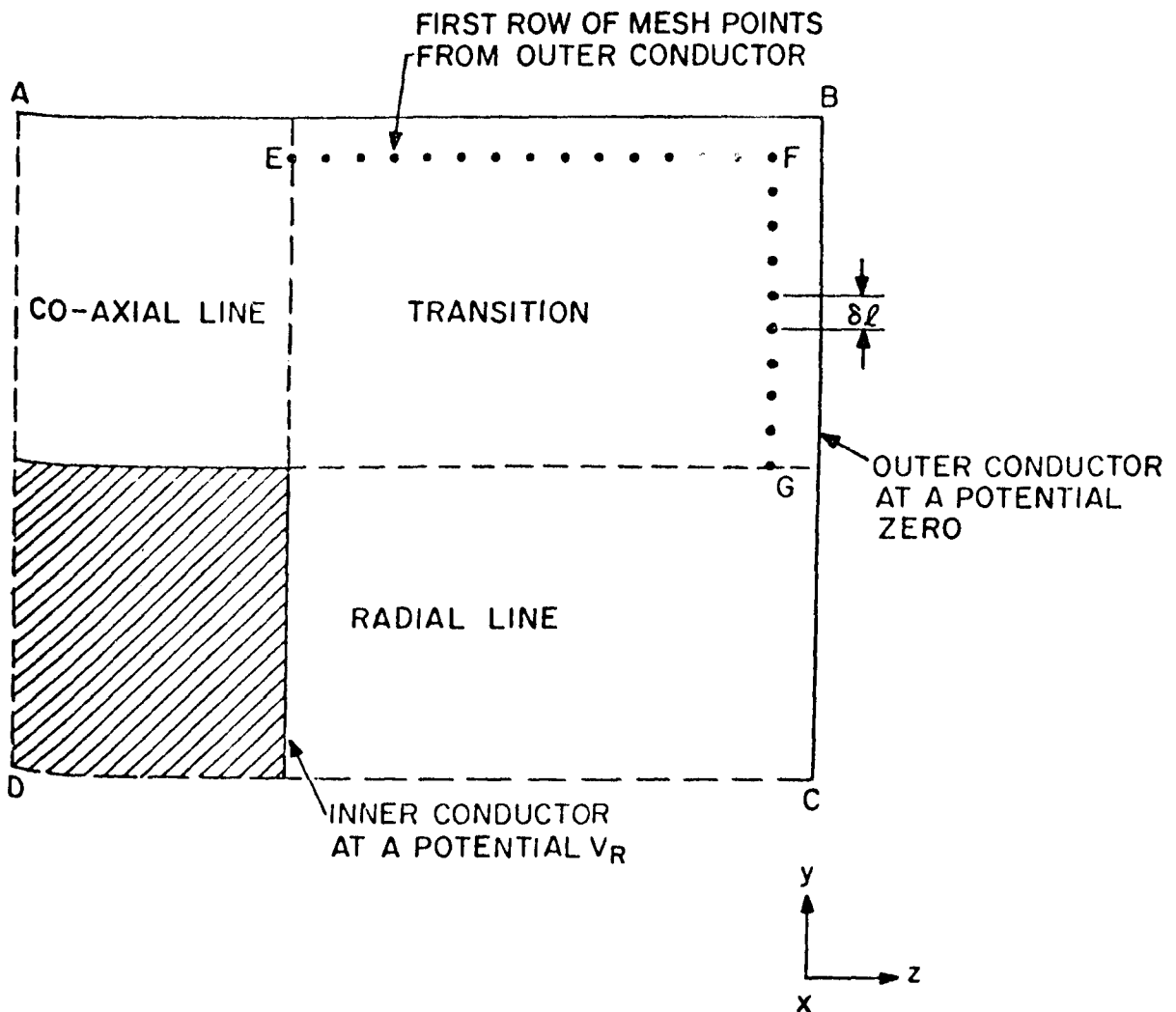
Figure 6.7. Transition Cavity Between the Radial and Coaxial Lines. (See Figure 6.6).

Now,

$$Q_R = \oint_S \underline{D}_R \cdot d\underline{s} \qquad (6.11)$$

$$= \oint_S \varepsilon \, \underline{E}_R \cdot d\underline{s}$$

where

D_R is the electric flux density

ε is the permittivity of free space

E_R is the electric field,

and the surface S is defined as that surface, parallel to the x-axis, whose cross-section is given by EFG (Figure 6.7) and width is unity. Thus,

$$Q_R = \varepsilon \cdot \left[\sum_z \underline{E}_{Rz} \bigg|_{FG} + \sum_y \underline{E}_{Ry} \bigg|_{EF} \right] \cdot \delta\ell \qquad (6.12)$$

where $\delta\ell$ is the distance between adjacent mesh points.

The equivalent transition capacitance (C_T) is given approximately by

$$C_T \doteq \pi d' C_p$$

where d' is the mean diameter of the cavity (planar approximation).

For the dimensions shown in Figure 6.6,

$$C_T = 0.16 \text{ pF.}$$

As the equivalent circuit elements of the transition were distributed, the capacitance C_T was divided into two equal capacitances $(C_T/2)$ to form a pi-network with the inductance L_T. The addition of the transition equivalent circuit to the transformer model gave a transformed impedance of curve D in Figure 6.5.

6.4.4 The Radial Line Transition Cavity

In general, for the radial line (Figures 6.8 and 6.9), the transmission line equations are [11]

$$\frac{dV}{dr} = -jKZI \qquad (6.13)$$
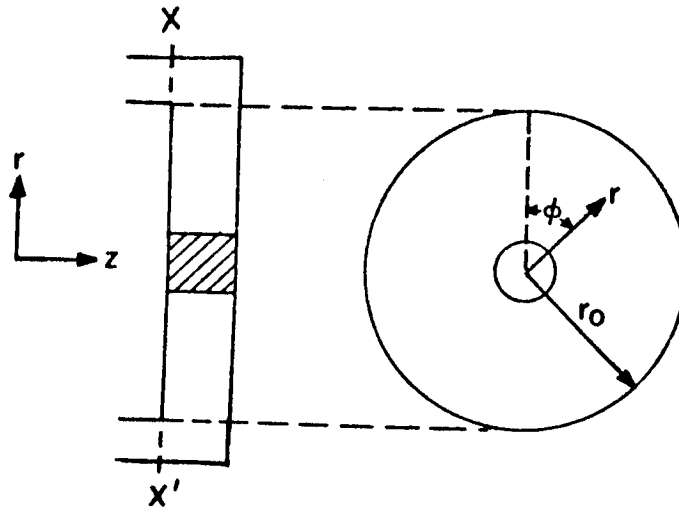
Figure 6.8. Radial Line Coordinate System.
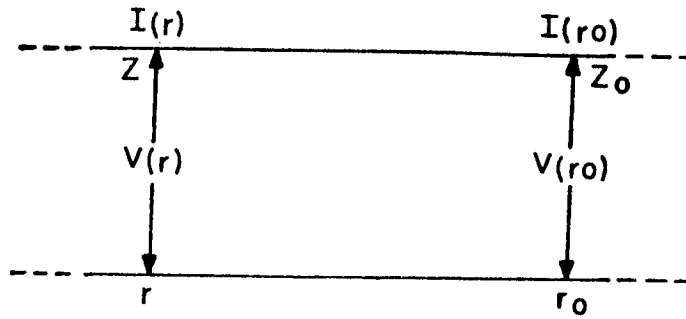
Figure 6.9. Radial Line Equivalent Transmission Line

$$\frac{dI}{dr} = -jKYV \qquad (6.14)$$

for each of the mode amplitudes V and I,

where

$$K = \left[k^2 - \left(\frac{n\pi}{b}\right)^2 - \left(\frac{m}{r}\right)^2 \right]^{\frac{1}{2}}$$

m and n are integers, b is the height of the radial line,

Z = 1/Y, is the characteristic impedance of the radial line

and   k = $2\pi/\lambda$.

For the dimensions of the radial line in the coaxial amplifier, small in comparison to a wavelength, a dominant TEM-type mode was assumed,

where   m = 0

and   n = 0.

For this mode, the electric field (E_t) is parallel to the z-axis and the magnetic field (H_t) is in the form of concentric circles about the z-axis (Figure 6.8).

In this case

$$E_t(r,\phi,z) = -\frac{V(r)}{b} \underline{z} \qquad (6.15)$$

and

$$H_t(r,\phi,z) = \frac{I(r)}{2\pi r} \underline{\phi} \qquad (6.16)$$

Also, the characteristic impedance Z is given by

$$Z = \xi \frac{b}{2\pi r}$$

where ξ is the intrinsic impedance of the medium.

The admittance seen at $Y'(r)$ due to a termination at r_o is given by

$$Y'(r) = \frac{j + Y'(r_o)\xi(x,y)ct(x,y)}{Ct(x,y) + jY'(r_o)\xi(x,y)} \qquad (6.17)$$

where

$$Y'(r) = \frac{Z.I(r)}{V(r)}$$

$$Y'(r_o) = \frac{Z_o I(r_o)}{V(r_o)} \qquad\qquad x = kr$$

$$\text{and } y = kr_o$$

and ct, Ct are radial cotangent functions tabulated by Marcuvitz [11].

For the dimensions shown in Figure 6.6, the pertinent parameters for the radial transmission line equations were taken to be (at 9.9 GHz)

$$r = 0.140 \text{ cm} \qquad\qquad x = 0.290 \text{ cm}$$

$$r_o = 0.284 \text{ cm} \qquad\qquad y = 0.543 \text{ cm}$$

$$ct(x,y) = 6.0$$

$$\xi(x,y) = 0.91$$

$$Ct(x,y) = 3.5$$

and,

$$y = 0.011$$

$$y_o = 0.021$$

The effect of the radial line on the transformed impedance can be seen on the Smith Chart (Figure 6.5) where curve E is the transformed impedance of the complete transformer model (Figure 6.10).

6.5 MEASUREMENTS AND DISCUSSION

6.5.1 Gain and Phase Measurements

The gain and phase shift of the reflection amplifier were measured by a network analyzer over the X-band range of frequencies, and are plotted in Figures 6.11 and 6.12. The coaxial transformer model, shown in Figure 6.10, was used in the calculation of the predicted gain and phase shift curves, which are also shown. For comparison, the simple transmission line model of the transformer gave a predicted gain curve that is shown in Figure 6.11. For the measurements, the circulator shown in Figure 6.3 was removed as the internal precision directional couplers of the network analyzer separated the input and output signals. Also, the signal path lengths were accurately known for this measurement plane. The effect of the circulator was noted to be equivalent to an increase in the signal path lengths and did not cause a significant loss in the power gain. Note that the phase shift of the amplifier was measured relative to the phase at the centre frequency, as an absolute value of phase depends on path lengths, such as that through the circulator. Table 6.1 summarizes the results:

The effects of the corrections to the matching transformer model on the predicted transformed input impedance is seen in Figure 6.5. A basis for comparison is the percentage change in reflection coefficient (vectorially) the correction produces when the predicted impedance terminates a 50 ohms line. (Table 6.2).

TABLE 6.1

Summary of Amplifier Predicted and Measured Results

	PREDICTED	MEASURED	% DIFFERENCE
Centre frequency	8.79 GHz	8.93 GHz	1.6
3 dB bandwidth	690 MHz	650 MHz	5.0
Power gain	12.0 dB	12.5 dB	4.0
Phase shift	138°	151°	8.5

TABLE 6.2

Comparison of Transformer Corrections

	% CHANGE IN REFLECTION COEFFICIENT
Discontinuity capacitances	1.5
Transition network	4.0
Radial transmission line	22

Errors in the values of the corrections could have occured due to radial standing waves produced by reflections at the right-angle transition, or the distortion of simple field patterns at discontinuities. For example, error could have been introduced in the value of transition capacitance due to the integration over the surface EFG (Figure 6.7) of flux that originated outside the transition volume. Also the radial line was assumed to have a terminating impedance that was calculated from transmission line equations up to that point. Slight error could have been included due to the distortion of fields at this transition.
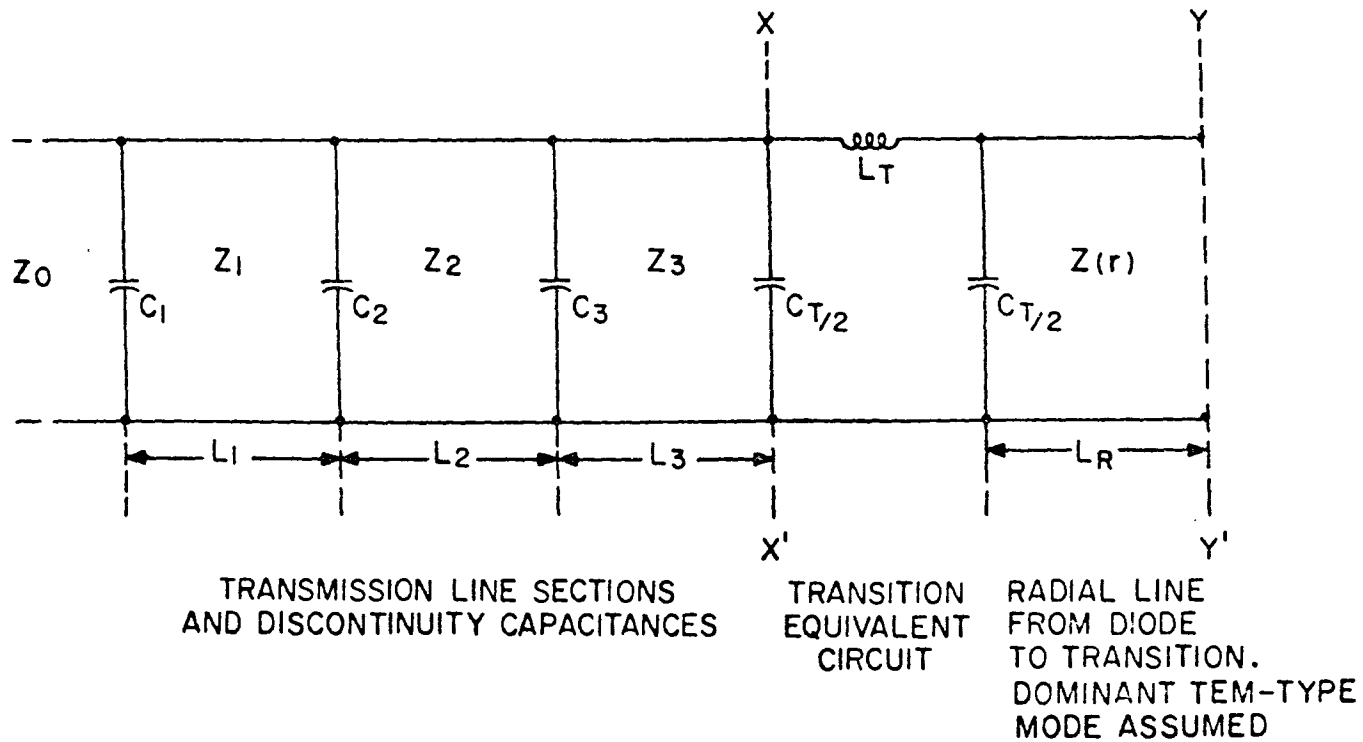
Figure 6.10. Complete Equivalent Circuit of the Coaxial Transformer.
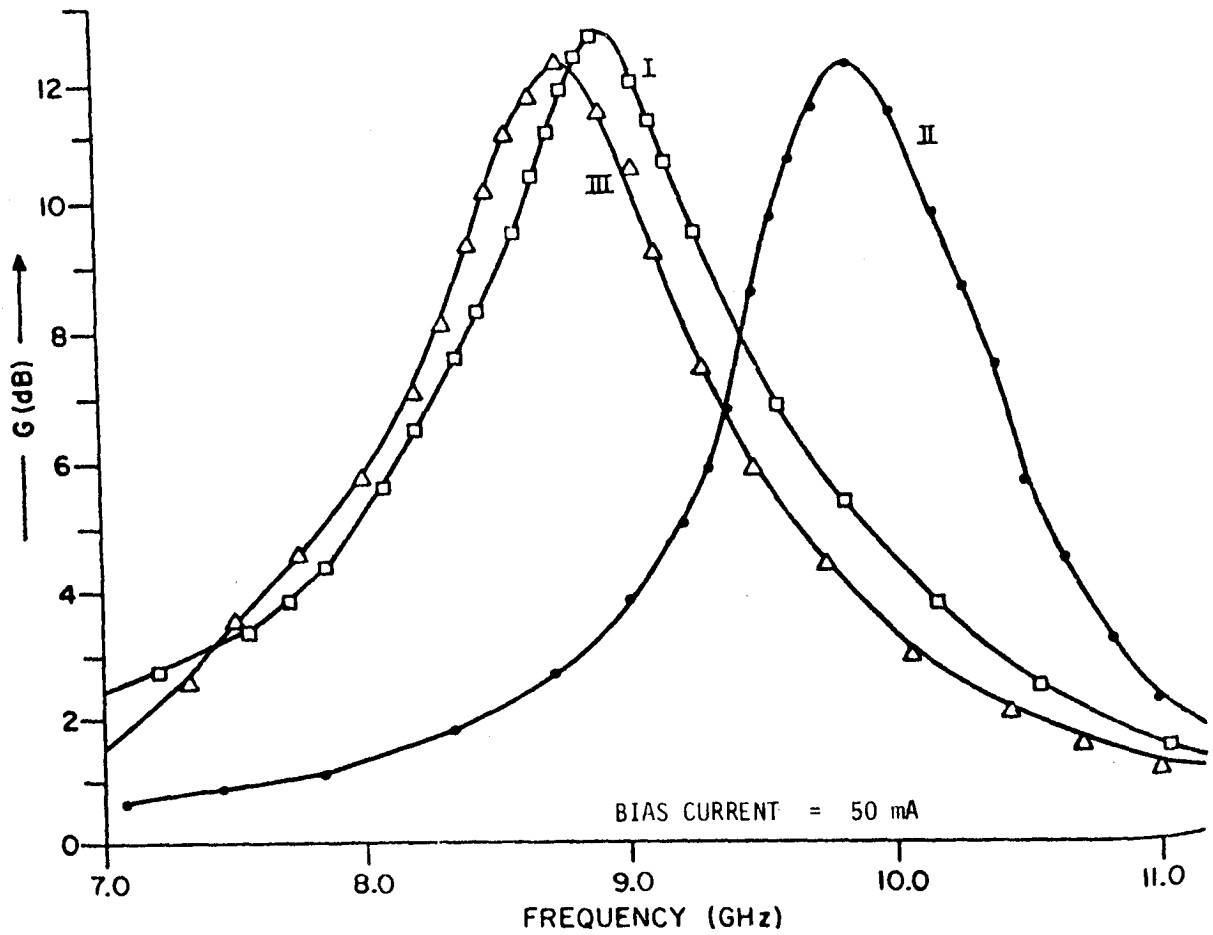
I   - measured gain,

II - predicted gain from Curve B in Figure 6.5,

III - predicted gain from complete model (Curve E in Figure 6.5).

Figure 6.11.   Power Gain (G) Curves for the IMPATT Amplifier.
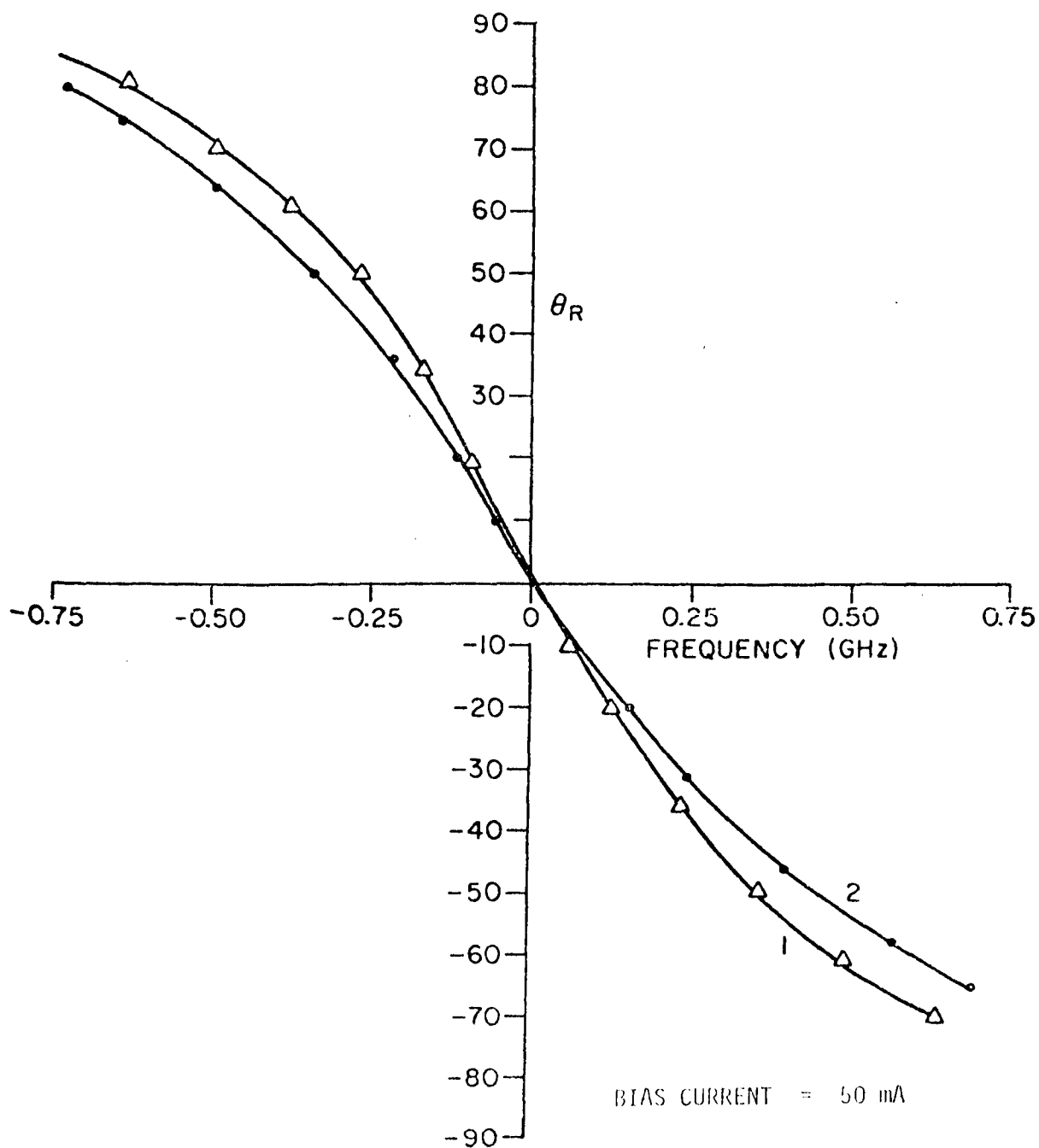
Figure 6.12. *Relative Phase Shift With Frequency for the IMPATT Amplifier.*
1) Measured phase relative to the centre frequency value.
2) Predicted relative phase from the complete transformer model.

6.5.2 Change in Amplifier Characteristics With Bias Current

An IMPATT amplifier was constructed such that the maximum gain occurred at a bias current of 30 mA. The centre frequency of 7.9 GHz was kept constant as the bias current was varied over the range 10-50 mA and the gain and relative phase shift obtained are shown in Figure 6.13 as Curve 1. To predict the performance of the amplifier with bias current the IMPATT diode was characterized (Chapter 4) by the lumped model parameters from the terminal impedance data at 30 mA and over X-band frequencies. The terminal impedance was computed at the new values of bias current and the resulting gain and phase shift of the amplifier predicted. These values are also plotted in Figure 6.13, and are shown as curve 2.

As expected from the results of Chapter 4, the lumped model prediction of amplifier gain and phase shift shows a divergence from the measured results at higher bias current densities (greater than 500 A cm^{-2}) where a more accurate model of the diode (for example, Fisher [13]) might be required. At low bias currents the divergence, which is accentuated on the decibel scale of Figure 6.13, could be due to current dependent losses which were assumed constant in the lumped model.

A practical application for communication systems which is indicated by these curves is a phase-shifter with gain [14]. A change in bias current from 20 mA to 44 mA changes the phase by approximately 90° and leaves the gain unchanged at 4.5 dB. By a suitable choice of IMPATT diode and cavity a phase shift of 180° is possible. This component could have application in Phase Shift Keyed systems operating at high data rates.

6.6 NOISE FIGURE MEASUREMENT OF THE IMPATT AMPLIFIER

6.6.1 Background to the Measurement

The noise figure of IMPATT amplifiers is an important design parameter as the inherently noisy avalanche process can limit applications in communications systems. The first measurements of IMPATT diode noise figures by DeLoach and Johnston [15] indicated values between 45 and 60 dB. Concurrently Hines [5] developed a small-signal noise theory that confirmed this result. He showed that the predominant noise originates in the random avalanche multiplication of a few initial ionizing events to form a pulse of charge for each cycle. The consequent phase jitter in the successive current pulses dominates the avalanche noise. For an IMPATT diode, as described in Section 3.2.1, the expression for noise figure (F) was found by Hines to be

$$F = 1 + \frac{q \dfrac{V_a}{KT}}{4m \, \tau_x \, (\omega^2 - \omega_a^2)} \qquad (6.18)$$

for high gain conditions,

where   q = electronic charge

   V_a = voltage drop across the avalanche zone
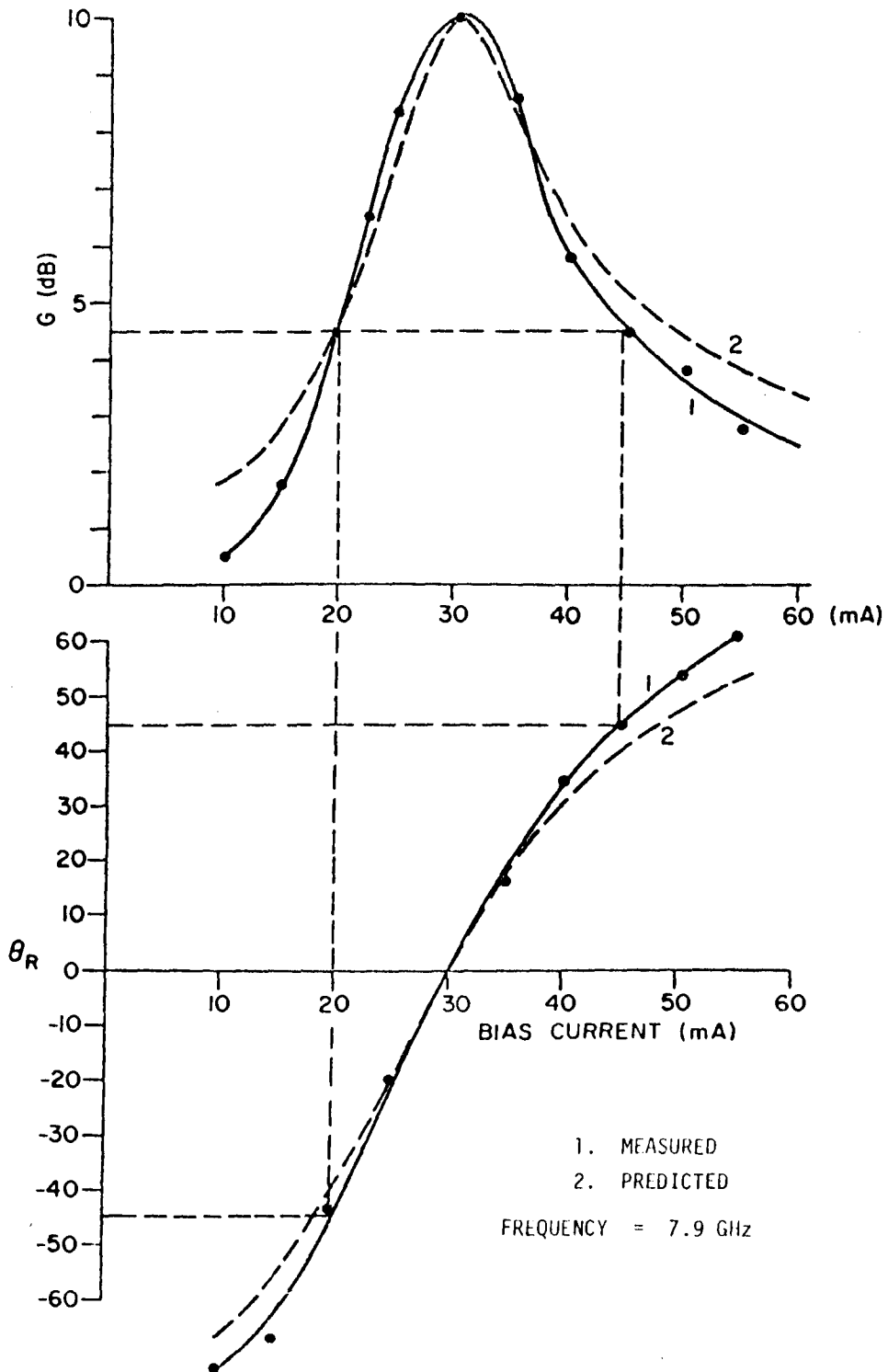
Figure 6.13. Gain and Relative Phase Shift Versus Bias Current.

K = Boltzmann constant

T = absolute temperature in $°K$

m = ionization coefficient

τ_x = delay time

= 1/2 (transit time in the avalanche zone)

ω = operating frequency

ω_a = the avalanche frequency.

This expression does not include the effects of thermal noise, frequency-converted noise, diffusion noise, generation-recombination noise, and flicker noise, all of which are assumed to be relatively small [16].

In 1967 Gummel and Blue [6] included the effects of unequal ionization rates and unequal velocities for holes and electrons, and the effect of parasitic resistance. Their results were presented in graphical form for noise measure (M) versus various parameters of the diode,

where

$$M = \frac{F-1}{1 - \dfrac{1}{G}} \tag{6.19}$$

and G is the gain of the amplifier. Since 1967, many diode and circuit parameters that affect the output noise power have been investigated such as device structure [17] and substrate material [18]. Injection-locking [7] and cavity stabilization [19] have been shown to reduce the output noise power of IMPATT oscillators.

Large-signal effects can also be important due to the dramatic increase in noise power with increase in signal level [20].

6.6.2 Noise Figure Measurement

The noise figure of a system (F) can be expressed as follows:

$$F = \frac{S_s/KT\omega_N N}{S_o/N_o} \tag{6.20}$$

where

S_s is the available source power into the system,

K is the Boltzmann's constant,

T is absolute temperature at $290^{\circ}K$,

ω_N is the equivalent noise bandwidth,

S_o is the available signal power out of the system,

N_o is the available noise power out of the system.

If the condition exists, such that

$$S_o = N_o \qquad (6.21)$$

then

$$F = \frac{S_s}{KT \, \omega_N} \qquad (6.22)$$

The source power, noise bandwidth and absolute temperature can be measured to give the noise figure in eqn. (6.22).

For two cascaded systems such as the amplifier followed by the receiver, the overall noise figure (F_o) can be written

$$F_o = F_A + \frac{F_R - 1}{G_A} \qquad (6.23)$$

where

F_A is the noise figure of the amplifier,

G_A is the gain of the amplifier,

and F_R is the noise figure of the receiver.

Several values of noise figure were measured with variation of frequency over the passband of the amplifier, discussed in Section 6.4. The measurement equipment is shown in Figure 6.14. The equivalent noise bandwidth was calculated from the measured frequency transfer function of the receiver system and found to be 2.21 MHz.

A measurement of noise figure is given:

Amplifier gain (G_A) at 9.0 GHz = 12.3 dB

IMPATT diode bias current = 50 mA.

The receiver "true r.m.s." reading was noted for no input signal to the amplifier, the receiver sensitivity decreased by 3 dB and the input signal
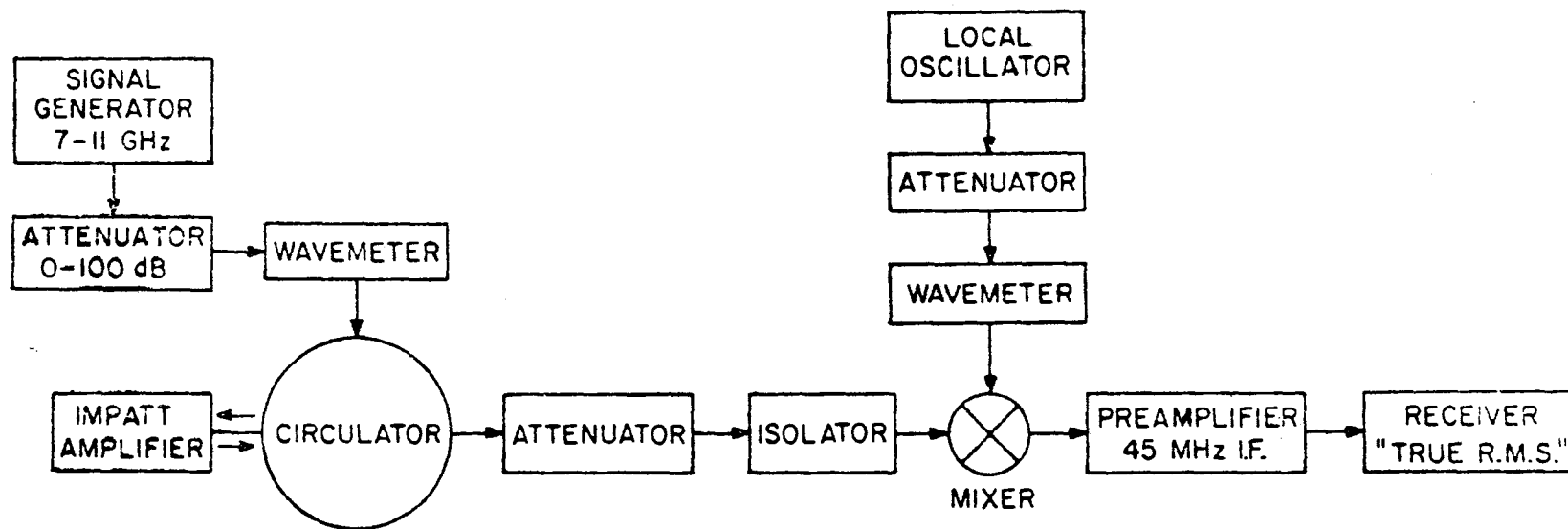
Figure 6.14. *Block Diagram of the Equipment for the Noise Figure Measurement.*

increased until the identical receiver reading was obtained. (Image effects were neglected.)

Thus, $S_O = N_O$ for the overall system. The value of the input power (S_s) at this condition was measured to be

$$S_s \text{ at the signal source} = 2.89 \text{ mW},$$

and through the 80 dB attenuator

$$S_s = 2.89 \times 10^{-11} \text{ W.}$$

Thus

$$F_o = \frac{2.89 \times 10^{-11}}{1.38 \times 10^{-23} \times 2.9 \times 10^2 \times 2.21 \times 10^6}$$

$$= 3290$$

$$= 35.2 \text{ dB.}$$

To measure the receiver noise figure (F_A), the diode cavity was replaced by a short circuit and the procedure repeated.

For this condition,

$$S_s = 5.3 \times 10^{-12} \text{ W}$$

and

$$F_R = 27.8 \text{ dB}$$

The amplifier noise figure (F_A) is given by:

$$F_A = F_o - \frac{F_R - 1}{G_A}$$

$$= 3290 - \frac{620 - 1}{17}$$

$$= 3220$$

$$= 35.1 \text{ dB}$$

The variation in noise figure with frequency for the diode was obtained from a tunable cavity and is shown in Figure 6.15 for constant amplifier gain.
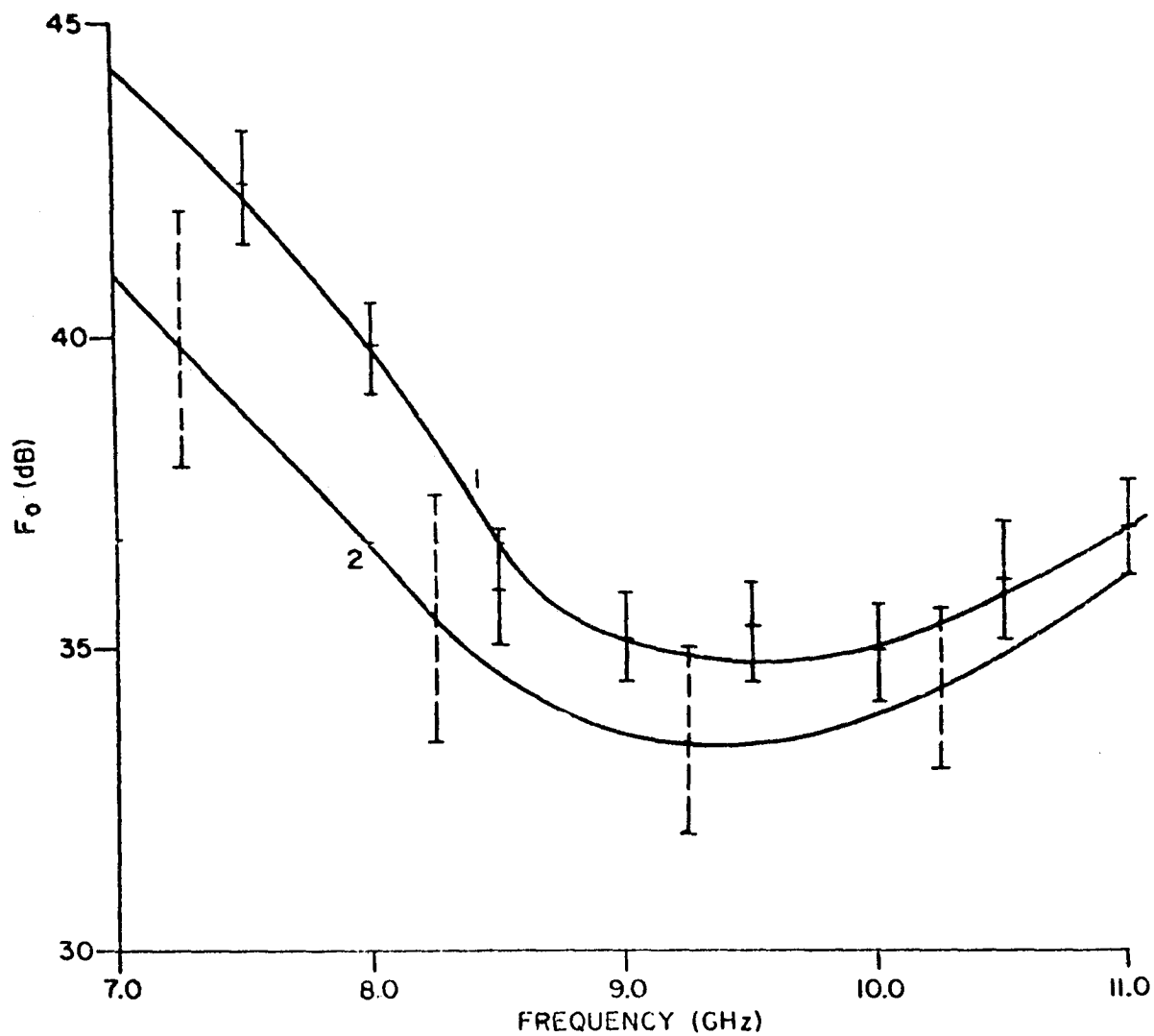
Figure 6.15.   Measured and Predicted Noise Figure Versus Frequency.

6.6.3 Comparison of Experimental and Theoretical Results

A qualitative comparison of the noise measurements and theoretically predicted values was made for the small-signal parameters of the diode found from the characterization method (Section 4.5). An example is given:

Parameters of the IMPATT diode were found to be:

(50 mA bias current)

$$\alpha' = 0.23$$

$$L_A = 0.51 \times 10^{-4} \text{ cm}$$

$$A_1 = 1.38 \times 10^{-4} \text{ cm}^2$$

The avalanche frequency was calculated to be 6.45 GHz.

$$L_D = 1.52 \times 10^{-4} \text{ cm}$$

$$R_s = 2.5 \text{ ohms}$$

From eqn. (6.18), the noise figure predicted by Hines was:

$$F_A = 26.5 \text{ dB}$$

Gummel and Blue [6] extended Hines' analysis and showed the effects of parastic resistance and unequal ionization rates for silicon on the noise figure. From their results, the effect of a parastic resistance of 2.5 ohms degraded the noise figure of the diode by approximately 1 dB at a bias current density of 550 A.cm^{-2} and a frequency of 1.4 times the avalanche frequency. Under similar conditions, the effect of unequal ionization rates further degraded the noise figure by approximately 6 dB.

The revised estimate of amplifier noise figure became

$$F_A = 26.5 + 1 + 6$$

$$= 33.5 \text{ dB}.$$

Similarly, predicted values of noise figure were calculated for the various cavity conditions for the IMPATT diode and are plotted in Figure 6.15.

The predicted values appear to be consistently lower than the measured values with a wide divergence at lower frequencies. This effect can be partially explained by a prediction of avalanche frequency that is low [21]. However, there are also many parameters, both of the model and of the amplifier cavity, that are known to affect the noise figure. For example, a reasonable value of voltage across the avalanche region was assumed, but this

value depends on the actual doping profile of the device. Also bias circuit [21] and cavity [19] design can significantly affect the amplifier noise figure.

6.7 CONCLUSIONS

The analysis of a coaxial transformer and diode cavity has been applied to a series-tuned IMPATT amplifier and has predicted the gain and phase shift curves over the 3 dB passband of the amplifier to within an average deviation of 4.5%.

The dominant correction to the simple transmission line theory for the transformer was the radial line correction which effectively adjusted the diode impedance reference plane to the outer skin of the diode ceramic case. The agreement of the measured and predicted curves also confirmed this choice of reference plane in the characterization method for the diode, described in Chapter 4. The significant correction for the radial line justified the use of exact transmission line equations and not just a simple one-or two-element lumped equivalent circuit. In applications where the effect of the transition is significant, the finite-difference method for the determination of the transition capacitance is useful as it can be applied to irregular shapes where analytic results would be difficult to obtain.

The lumped model of the diode was sufficiently accurate for the prediction within 5% of the amplifier characteristics for medium currents (20-40 mA in a range of 10-55 mA) but at low and high currents the model required improvement. This confirmed the results at high current densities of Chapter 4. The communications capability of the amplifying phase-shifter requires further research but an initial practical difficulty could be in the design of a high speed (<1 nsec) pulse generator that could switch large values of power. (>1 watt).

The high noise figure of the IMPATT amplifier was confirmed by measured values of 35-40 dB. The shape of the noise figure versus frequency curve was supported from theory [6] but a quantitative comparison was difficult due to the individual characteristics of such factors as diode parameters, bias current circuits and cavity design, that can significantly affect the measured value of noise figure.

7. CONCLUSION

7.1 CONCLUSIONS

The objective of this work was the integration of IMPATT diode analysis and microwave circuit analysis in the design of active microwave components.

For the first time, so far as is known:

I.   The lumped model of the IMPATT diode was extended to a diode of nonuniform cross-section and this model was used in a characteriza-

tion method to obtain the parameters of the active chip and the package;

II.   The microwave circuitry of an X-band microstrip oscillator was analyzed with particular attention to the microstrip connector and diode reference plane so that the eigenvalues of the system gave the oscillation frequency;

III.   The small-signal gain, phase-shift and noise figure of an X-band amplifier were predicted from the lumped model of the IMPATT diode.

From these results it may be concluded that:

1.   State space formulation of the lumped model of the IMPATT diode and the external circuit leads to standard matrix methods of solution. However, for frequencies at X-band and higher many microwave circuits are represented as modified transmission lines for which the state space representation is cumbersome and does not necessarily improve the speed of solution.

2.   The lumped model describes the behavior of the IMPATT diode within a few percent for current densities below 550 A cm^{-2} but above this value the assumption of constant region lengths does not hold. Also, the effect of chip taper on the terminal impedance of the IMPATT diode is of second order compared to the effects of the other parameters.

3.   The choice of the diode reference plane is an important factor in the analysis of circuit and diode interaction at X-band. In coaxial line the outer skin of the diode ceramic case is a suitable reference plane from which a radial mode can emanate, but when the diode is placed in a microstrip circuit a new and equivalent reference plane must be defined for the pseudo-TEM mode.

Hence this investigation has shown that, while state space methods can provide a standard approach to the analysis of active microwave circuits, yet the present state of development does not encourage this, and consequently particular care should be taken in the analysis of the circuitry, such as the choice of a suitable diode reference plane which has hitherto received insufficient attention.

The applications of this work are not confined to the IMPATT diode. Other applications would include any packaged microwave device for which the lumped model of the chip is known and a characterization and design procedure is required.

7.2 EXTENSIONS

The limitations of the lumped model and circuit analysis methods presented in this work should be examined at higher output powers and higher frequencies as suitable devices are becoming available. At higher output

powers large-signal results could be significantly different from small-signal due to the impedance variation of the IMPATT diode with signal level. To improve the prediction of avalanche frequency the effect of transit time in the avalanche region should be included in the small-signal model. At frequencies higher than X-band it is doubtful that the simple package equivalent circuit would be valid and a more complex circuit is required. Also at higher frequencies the microstrip losses become more significant, the microstrip-to-coaxial-line connector becomes an increasingly important discontinuity and the microstrip impedance transformer involves additional complications at the junctions, all of which indicate the need for further research on microstrip circuits.

Further work is required on the state space representation of transmission lines to obtain the minimum number of state variables for a multi-section circuit. This research could consider the use of either time-delayed functions or lumped L and C elements.

The high noise figure of the IMPATT diode limits the applications of the device in communications systems. A unified approach to the analysis of IMPATT diode noise is required that can optimize the various parameters of the diode chip, operating conditions and external circuit for a minimum noise figure.

State space methods possibly could be applied to the analysis of digital microwave components such as the active phase shifter which could operate at gigabit data rates in a phase-shift-keyed communications system. A maximum permissible data rate might be indicated as a function of the switching transients involved.

A recently introduced contender of the IMPATT diode is the BARITT diode. Once a suitable model of the chip is chosen, the BARITT diode could be characterized and the performance compared to the IMPATT diode, towards the goal of a unified approach to the design of soild-state microwave circuits.

8. ACKNOWLEDGEMENTS

9. REFERENCES

CHAPTER 1

1. W. Shockley, *Negative Resistance Arising from Transit Time in Semiconductor Diodes*, Bell System Tech. Journal, Vol. 33, pp. 799-826, July 1954.

2. W.T. Read, *A Proposed High Frequency Negative Resistance Diode*, Bell System Tech. Journal, Vol. 37, pp. 401-446, March 1958.

3. C.A. Lee, R.L. Batdorf, W. Wiegmann and G. Kaminsky, *The Read Diode-An Avalanching, Transit Time Negative Resistance Oscillator*, Appl. Physics Letters, Vol. 6, pp. 89-91, 1 March 1965.

4. R.L. Johnston, B.C. DeLoach and B.G. Cohen, *A Silicon Diode Microwave Oscillator*, Bell System Tech. Journal, Vol. 44, pp. 369-372, February 1965.

5. T. Misawa, *Negative Resistance in p-n Junctions under Avalanche Breakdown Conditions*, IEEE Trans. on Electron Devices, Vol. ED-13, pp. 137-151, January 1966.

6. M. Gilden and M.E. Hines, *Electronic Tuning Effects in the Read Microwave Avalanche Diode*, IEEE Trans. on Electron Devices, Vol. ED-13, pp. 169-175, January 1966.

7. S.T. Fisher, *Small Signal Impedance of Avalanching Junctions with Unequal Electron and Hole Ionization Rates*, IEEE Trans. on Electron Devices, Vol. ED-14, pp. 313-322, June 1967.

8. H.K. Gummel and D.L. Scharfetter, *Avalanche Region of IMPATT Diodes*, Bell System Tech. Journal, Vol. 45, pp. 1797-1827, December 1966.

9. W.J. Evans and G.I. Haddad, *A Large Signal Analysis of IMPATT Diodes*, IEEE Trans. on Electron Devices, Vol. ED-15, pp. 708-717, October 1968.

10. R. Kuvas and C.A. Lee, *Nonlinear Analysis of Multifrequency Operation of Read Diodes*, J. Appl. Physics, Vol. 41, pp. 1756-1767, 15 March 1970.

11. W.E. Schroeder, P.T. Greiling and G.I. Haddad, *Multifrequency Operation of IMPATT Diodes*, IEEE Int. Electron Devices meeting, Washington, D.C., October 1969.

12. D.L. Scharfetter and H.K. Gummel, *Large Signal Analysis of a Silicon Read Diode Oscillator*, IEEE Trans. on Electron Devices, Vol. ED-16, pp. 64-77, January 1969.

13. J.L. Blue, *Approximate Large Signal Analysis of IMPATT Oscillators*, Bell System Tech. Journal, Vol. 48, pp. 383-396, February 1969.

14. P.T. Greiling and G.I. Haddad, *Large Signal Equivalent Circuits of Avalanche Transit Time Devices*, IEEE Trans. on Microwave Theory and Techniques, Vol. MTT-18, pp. 842-853, November 1970.

15. H.J. Prager, K.K.N. Chang and S. Weisbrod, *High Power, High Efficiency, Silicon Avalanche Diodes at U.H.F.*, Proc. IEEE (Corr.), Vol. 55, pp. 586-587, April 1967.

16. D.L. Scharfetter, D.J. Bartelink, H.K. Gummel and R.L. Johnston, *Computer Simulation of Low Frequency, High-Efficiency Oscillation in Germanium*, IEEE Solid State Device Research Conf., Boulder, Colo, June 1968.

17. H. Sobol and F. Sterzer, *Solid State: Microwave Power Sources*, IEEE Spectrum, Vol. 9, pp. 20-33, April 1972.

18. J.B. Gunn, *Microwave Oscillations of Current in III-V Semiconductors*, Solid State Comm., Vol. 1, pp. 88-91, September 1963.

19. D.J. Coleman and S.M. Sze, *A Low Noise Metal Semiconductor Metal (MSM) Microwave Oscillator*, Bell System Tech. Journal, Vol. 50, pp. 1695-1699, May-June 1971.

20. D.R. Conn, R.H. Mitchell and J.A.C. Stewart, *State Space Analysis of an IMPATT Diode Lumped Model*, Proc. IEEE (Letters), Vol. 58, No. 5, pp. 809-810, May 1970.

CHAPTER 2

1. R.E. Kalman and J.E. Bertram, *Control System Analysis and Design Via the "Second Method" of Lyapunov: 1. Continuous Time Systems. II-Discrete Time Systems*, Trans. ASME., J. Basic Eng., Vol. 82, pp. 371-393, June 1960.

2. L.A. Zadeh and C.A. Desoer, *Linear System Theory: The State Space Approach*, New York, McGraw-Hill, 1963.

3. T.R. Bashkow, *The A Matrix, New Network Description*, IRE Trans. on Circuit Theory, Vol. CT-4, pp. 117-120, September 1957.

4. E.S. Kuh and R.A. Rohrer, *The State-Variable Approach to Network Analysis*, Proc. IEEE, Vol. 53, pp. 672-686, July 1965.

5. D.L. Snyder, *The State-Variable Approach to Continuous Estimation with Applications to Analogue Communication Theory*, MIT Research Monograph No. 51, Cambridge, Mass., 1969.

6. H.I. Paul and W.E. Larrimore, *Gated Phase Locked Loop in the Presence of Noise*, Inter. Conf. on Communications, IEEE Conf. Record, pp. 6-12, 19-21 June 1972.

7. K.M. Wong, *State Space Approach to the Multiplication Error in a Digital Filter*, Electronics Letters, Vol. 9, No. 10, pp. 224-226, 17 May 1973.

8. M.A. Murray-Lasso, *Automatic General Purpose Microwave Circuit Analysis Program*, IEEE Trans. on Microwave Theory and Techniques, Vol. MTT-17, No. 8, pp. 529, August 1969.

9. D.R. Conn, R.H. Mitchell and J.A.C. Stewart, *State Space Analysis of an IMPATT Diode Lumped Model*, Proc. IEEE (letters), Vol. 58, No. 5, pp. 809-810, May 1970.

10. J.A.C. Stewart, D.R. Conn and R.H. Mitchell, *State Space Analysis of General IMPATT Diode Small Signal Models*, IEEE Trans. Microwave Theory and Techniques, Vol. MTT-18, No. 11, pp. 835-842, November 1970.

11. D.R. Conn, *State Space Analysis of Microwave Active Devices*, Ph.D. Thesis, Queen's University, Kingston, Chapter 9, April 1970.

12. J.W. Moffat and R.H. Mitchell, *Large Signal Lumped Modelling and Characterization of an IMPATT Diode*, IEEE Trans. on Electron Devices (Corresp.), Vol. ED-19, pp. 1297-1299, December 1972.

13. C.O.G. Obah, *State Space Analysis of TRAPATT Diodes*, Ph.D. Thesis, Queen's University, Kingston, 1973.

14. P.M. DeRusso, R.J. Roy and C.M. Close, *State Variables for Engineers*, Wiley, New York, 1965.

15. K. Ogata, *State Space Analysis of Control Systems*, Prentice Hall, 1967, Chapter 6.

16. Private Communication with Mr. M.K. Yeung, Queen's University.

17. A. Chowaniec, *Large Signal Lumped Models of Read IMPATT Diodes*, M.Sc. Thesis, Queen's University, Kingston, December 1972.

18. R. Kuvas, *Large Signal Semiconductor Avalanche*, Ph.D. Thesis, Cornell University RADC-TR-70-142, pp. 87-94, August 1970.

CHAPTER 3

1. W.T. Read, *Proposed High Frequency Negative Resistance,* Bell System Technical Journal, Vol. 37, pp. 401-446, March 1958.

2. M. Gilden and M.E. Hines, *Electronic Tuning Effects in the Read Microwave Avalanche Diodes,* IEEE Trans. Electron Devices, Vol. ED-13, pp.169-175, January 1966.

3. D.R. Conn, *State Space Analysis of Microwave Active Devices,* Ph.D. Thesis, Queen's University, Kingston, 1970.

4. R.S. Engelbrecht, *S.S. Bulk Phenomena and their Application to Integrated Electronics,* IEEE Trans. Solid State Circuits, Vol. SC-3, pp. 210-212, September 1968.

5. A.E. Winter and R.H. Mitchell, *Characterization of IMPATT Diodes",* Int. J. of Electronics, Vol. 31, No. 5, pp. 471-483, 1971.

6. W.J.Getsinger, *The Packaged and Mounted Diode as a Microwave Circuit,* IEEE Trans. on Microwave Theory and Techniques, Vol. MTT-14, pp. 58-69, February 1966.

7. R.P. Owens and D. Cawsey, *Microwave Equivalent Circuit Parameters of Gunn Effect Packages,* Vol. MTT-18, pp. 790-798, November 1970.

8. I.W. Pence and P.J. Khan, *Broad-band Equivalent Circuit Determination of Gunn Diodes,* IEEE Trans. on Microwave Theory and Techniques, Vol. MTT-18, pp. 784-789, November 1970.

CHAPTER 4

1. W.J. Getsinger, *The Packaged and Mounted Diode as a Microwave Circuit,* IEEE Trans. on Microwave Theory and Techniques, Vol. MTT-14, pp. 58-69, February 1966.

2. W.J.L. McCready and J.A.C. Stewart, *Small Signal Characterization of IMPATT Diodes,* Int. J. of Electronics, Vol. 28, pp. 551-564, 1970.

3. J.W. Bandler, *Precision Microwave Measurement of the Internal Parasitics of Tunnel Diodes,* IEEE Trans. on Electron Devices, Vol. ED-15, pp. 275-282, May 1968.

4. R.P. Owens and D. Cawsey, *Microwave Equivalent Circuit Parameters of Gunn Effect Device Packages,* IEEE Trans. on Microwave Theory and Techniques, Vol. MTT-18, pp. 790-798, November 1970.

5. R.P. Owens, *Mount Independent Equivalent Circuit of the S_4 Diode Package*, Electronics Letters, Vol. 7, No. 19, pp. 580-582, September 1971.

6. J.W. Bandler, *Optimization Methods for Computer Aided Design*, IEEE Trans. on Microwave Theory and Techniques, Vol. MTT-17, pp. 533-552, August 1969.

7. R. Fletcher, *Function Minimization without Calculating Derivatives- a Review*, Computer Journal, Vol. 8, pp. 33-41, April 1965.

8. D.J. Wilde and C.S. Beightler, *Foundations of Optimization*, Prentice Hall, p. 16, 1967.

9. S.F. Mahmoud and J.C. Beal, *V.L.F. Propagation Parameters Derived from Observations of Sunrise and Sunset Phenomena*, Proc. IEE, Vol. 118, No. 10, pp. 1272-1279, October 1971.

10. I.W. Pence and P.J. Khan, *Broad Band Equivalent Circuit Determination of Gunn Diodes*, IEEE Trans. on Microwave Theory and Techniques, Vol. MTT-18, pp. 784-790, November 1970.

11. H.H. Rosenbrock, *An Automatic Method for Finding the Greatest or Least Value of a Function*, Computer Journal, Vol. 3, pp. 175-184, October 1960.

12. M.J.D. Powell, *A Survey of Numerical Methods for Unconstrained Optimization*, SIAM Review, Vol. 12, No. 1, pp. 79-97, January 1970.

13. M.J.D. Powell, *An Efficient Method for Finding the Minimum of a Function of Several Variables Without Calculating Derivatives*, Computer Journal, Vol. 7, pp. 155-162, July 1964.

14. A.D. Waren, L.S. Lasdon and D.F. Suchman, *Optimization in Engineering Design*, Proc. IEEE, Vol. 55, pp. 1832-1836, November 1967.

15. M. Gilden and M.E. Hines, *Electronic Tuning Effects in the Read Microwave Avalanche Diode*, IEEE Trans. on Electron Devices, Vol. ED-13, pp. 169-175, January 1966.

16. T.W. Sigmon and J.F. Gibbons, *Diffusivity of Electrons and Holes in Silicon*, Applied Physics Letters, Vol. 15, pp. 320-322, 15 November 1969.

17. C.N. Dunn and J.E. Dalley, *Computer-Aided Small Signal Characterization of IMPATT Diodes*, IEEE Trans. on Microwave Theory and Techniques, Vol. MTT-17, pp. 691-695, September 1969.

18. W.E. Schroeder and G.I. Haddad, *Nonlinear Properties of IMPATT Devices,* Proc. IEEE, Vol. 61, pp. 153-182, February 1973.

CHAPTER 5

1. T.M.S. Heng, *Trimming of Microstrip Circuits Utilizing Micro-cantilever Air Gaps,* IEEE Trans. on Microwave Theory and Techniques, Vol. MTT-19, pp. 652-653, July 1971.

2. K. Kurokawa, *An Introduction to the Theory of Microwave Circuits,* Academic Press, New York, Chapter 9, 1969.

3. F. Assadourian and E. Rimai, *Simplified Theory of Microstrip Transmissions Systems,* Proc. IEEE, pp. 1651-1663, December 1952.

4. P. Silvester, *TEM Wave Properties of Microstrip Transmission Lines,* Proc. IEE, Vol. 115, pp. 43-48, January 1968.

5. M. Caulton, J. Hughes and H. Sobol, *Measurements on the Properties of Microstrip Transmission Lines for Microwave Integrated Circuits,* RCA Review, pp. 377-397, September 1966.

6. T.G. Bryant and J.A. Weiss, *Parameters of Microstrip Transmission Lines and of Coupled Pairs of Microstrip Lines,* Trans. IEEE on Microwave Theory and Techniques, Vol. MTT-16, pp. 1021-1027, December 1968.

7. M.K. Krage and G.I. Haddad, *Frequency Dependent Characteristics of Microstrip Transmission Lines,* IEEE Trans. on Microwave Theory and Techniques, Vol. MTT-20, pp. 678-688, October 1972.

8. A.E. Winter and R.H. Mitchell, *Characterization of IMPATT Diodes,* Int. Journal of Electronics, Vol. 31, No. 5, pp. 471-483, 1971.

9. J.W. Moffat and R.H. Mitchell, *Large Signal Lumped Modelling and Characterization of an IMPATT Diode,* IEEE Trans. on Electron Devices (Corresp.), Vol. ED-19, pp. 1297-1298, December 1972.

10. P. Benedek and P. Silvester, *Equivalent Capacitances for Microstrip Gaps and Steps,* IEEE Trans. on Microwave Theory and Techniques, Vol. MTT-20, pp. 729-733, November 1972.

11. J.L. Schallenberg and J.C. Beal, *Scattering Parameter Measurement Techniques in Microstrip,* presented at the IEEE-GMTT Microwave Symposium, Chicago, May 1972.

12. P. Troughton, *Measurement Techniques in Microstrip*, Electronics
    Letters, Vol. 5, pp. 25-26, January 1969.

13. P.J. Meier, H.C. Okean and E.W. Sard, *Integrated X-band Sweeping
    Super-hetrodyne Receiver*, IEEE Trans. of Microwave Theory and
    Techniques, Vol. MTT-19, pp. 600-608, July 1971.

14. B. Glance and R. Trambarulo, *A Waveguide to Suspended Stripline
    Transition*, IEEE Trans. on Microwave Theory and Techniques,
    Vol. MTT-21, pp. 117-118, February 1973.

15. D.S. James and S.H. Tse, *Microstrip End Effects*, Electronics
    Letters, Vol. 8, pp. 85-86, February 1972.

16. O.P. Jain, V. Makios and W.J. Chudobiak, *Open-end and Edge
    Effects in Microstrip Transmission Lines*, IEEE Trans. Microwave
    Theory and Techniques (Corresp.), Vol. 20, pp. 626-628,
    September 1972.

17. M.A.R. Gunston and J.R. Weale, *The Transmission Characteristics
    of Microstrip*, The Marconi Review, pp. 226-243, 3rd Quarter, 1969.

18. W.J. Evans, *Nonlinear and Frequency Conversion Characteristics of
    IMPATT Diodes*, Technical Report 104, Electron Physics Laboratory,
    Michigan, February 1968.

CHAPTER 6

1. M.E. Hines, *Negative Resistance Diode Power Amplification*, IEEE
   Trans. on Electron Devices, Vol. ED-17,pp. 1-8, January 1970.

2. M.J.E. Golay, *Normalized Equations of the Regenerative
   Oscillator-Noise, Phase Locking and Pulling*, Proc. IEEE,Vol. 52,
   pp. 1311-1330, November 1964.

3. J.E. Morris and J.W. Gewartowski, *A One-way 6 GHz IMPATT Amplifier
   for Short Haul Radio Applications*, International Conf. on
   Communications, Seattle, Washington, pp. 27-8 to 27-13, June 1973.

4. D.S. James and K.N. Patel, *Microwave Measurement of the Per-
   mittivity of Low-Loss Materials*, Journal of Canadian Ceramic
   Soc., Vol. 41, pp. 77-81, 1972.

5. H.E. Hines, *Noise Theory for the Read Type Avalanche Diode*,
   IEEE Trans. on Electron Devices, Vol. ED-13, pp. 158-163,
   January 1966.

6. H.K. Gummel and J.L. Blue, *A Small-Signal Theory of Avalanche Noise in IMPATT Diodes*, IEEE Trans. on Electron Devices, Vol. ED-14, pp. 569-580, September 1967.

7. K. Kurokawa, *Noise in Synchronized Oscillators*, IEEE Trans. on Microwave Theory and Techniques, Vol. MTT-16, pp. 234-240, April 1968.

8. S.B. Cohn, *Optimum Design of Stepped Transmission Line Transformers*, IRE Trans. on Microwave Theory and Techniques, Vol. MTT-3, pp. 16-21, April 1955.

9. G.L. Mattaei, L. Young and E.M.T. Jones, *Microwave Filters, Impedance Matching Networks and Coupling Structures*, McGraw-Hill, New York, 1964.

10. R.E. Collin, *Foundations for Microwave Engineering*, McGraw-Hill, New York, 1966.

11. N. Marcuvitz, *Waveguide Handbook*, McGraw-Hill, New York, 1951.

12. P. Silvester, *Modern Electromagnetic Fields*, Prentice Hall, Chapter 2, 1968.

13. S.T. Fisher, *Small-Signal Impedance of Avalanching Junctions with Unequal Electron and Hole Ionization Rates and Drift Velocities*, IEEE Trans. on Electron Devices, Vol. ED-14, pp. 313-322, June 1967.

14. P. Brook, L.D. Clough and K.G. Hambleton, *Microwave Phase Shifting with Gain Using IMPATT Diodes*, Electronics Letters, Vol. 8, No. 19, pp. 489-491, September 1972.

15. B.C. DeLoach and R.L. Johnston, *Avalanche Transit-Time Microwave Oscillators and Amplifiers*, IEEE Trans. on Electron Devices, Vol. ED-13, pp. 181-186, January 1966.

16. M.S. Gupta, *Noise in Avalanche Transit Time Devices*, Proc. IEEE, Vol. 59, pp. 1674-1687, December 1971.

17. H. Statz and H.A. Haus, *The Dependence of Noise in IMPATT Diodes on Doping Profile*, Proc. IEEE Conf. on High Frequency Generation and Amplification, Cornell University, pp. 155-164, August 1971.

18. P.A. Levine, A.B. Dreeben and A.R. Triano, *Low Noise Operation of CW GaAs Avalanche Diode Oscillators*, Proc. IEEE (Lett.), Vol. 59, pp. 1128-1137, July 1971.

19. K. Schunemann and B. Schick, *Comparison Between Transmission and Reaction Cavity Stabilized Oscillators*, Elect. Letters, Vol. 7, No. 20, pp. 618-621, October 1971.

20. R.L. Kuvas, *Noise in IMPATT Diodes: Intrinsic Properties*, IEEE Trans. on Electron Devices, Vol. ED-19, pp. 220-233, February 1972.

21. R.B. Emmons and G. Lucovsky, *The Frequency Response of Avalanching Photodiodes*, IEEE Trans. on Electron Devices, Vol. ED-13, pp. 297-305, March 1966.

22. E.R. Scherer, *Investigations of the Noise Spectra of Avalanche Oscillators*, IEEE Trans. on Microwave Theory and Techniques, Vol. MTT-16, pp. 781-788, September 1968.

CRC DOCUMENT CONTROL DATA

1. ORIGINATOR: Communications Systems

2. DOCUMENT NO: CRC Report No. 1257

3. DOCUMENT DATE: December, 1974

4. DOCUMENT TITLE: Characterization and Design of IMPATT Devices and Associated Circuits

5. AUTHOR(s):   A.E. Winter

6. KEYWORDS: (1) __IMPATT Devices__

     (2) __Circuits__

     (3) __Design__

7. SUBJECT CATEGORY (FIELD & GROUP: COSATI)

     09   Electronics and Electrical Engineering

     09   03   Electronic and Electrical Engineering

8. ABSTRACT:

  IMPATT diode and microwave circuit interactions at X-band are examined by means of state space techniques. Complexity of circuit formulation is found to limit the usefulness of state space representation as the standard method of device/circuit analysis.

  A small-signal lumped model for the IMPATT diode is extended to a nonuniform cross-section chip. This model is used in a characterization method to obtain the parameters of both the chip model and the package equivalent circuit by computer search. At current densities higher than 550 A cm^{-2} the simple lumped model requires improvement.

  A design procedure is presented for a microstrip IMPATT diode oscillator and the frequency of operation is predicted to within 3 percent. The effects of the diode reference plane and the microstrip-to-coaxial-line connector are significant.

  The gain and phase shift of a coaxial IMPATT diode amplifier is predicted from the lumped model and experimentally verified. The noise figure of the amplifier, measured as 35 dB, indicates a limitation of the IMPATT diode in many communications systems.

9. CITATION: _____

_____